Simulation-based Design of Temperature-responsive Nematic Elastomers

by

Ryan Alexander Epp Neufeld

A thesis
presented to the University of Waterloo
in fulfillment of the
thesis requirement for the degree of
Master of Applied Science
in
Chemical Engineering (Nanotechnology)

Waterloo, Ontario, Canada, 2017

I hereby declare that I am the sole author of this thesis. This is a true copy of the thesis, including any required final revisions, as accepted by my examiners.

I understand that my thesis may be made electronically available to the public.

Abstract

Liquid crystal elastomers (LCEs) are a class of polymer networks which involve the incorporation of liquid crystal (LC) molecules into their polymer backbone or side chain. This results in anisotropy in their mechanical, optical, and electromagnetic properties similar to those exhibited by traditional LC materials. Their mechanical properties are highly coupled to the internal state of LC order, which can result in large mechanical deformations as LC order changes. This can occur in response to a variety of external stimuli such as changes in temperature, exposure to light, and application of external fields.

The interplay between LC order and mechanical properties makes LCEs a highly promising class of functional materials and subsequently, they have been the subject of much research over the past several decades. However, developing an application of LCEs remains difficult in that their mechanical response is both complex and coupled to the state of liquid crystal order prior to cross-linking. Their physics are sufficiently complicated that in most cases, the use of pen-and-paper analysis is precluded. Additionally, the LCE fabrication process is complex and expensive, making trial-and-error experimental design methods unsuitable. This motivates the development and use of simulation-based methods to augment traditional experimental design methods.

The two main contributors to the complexity of the design of LCE applications are the choice and imposition of liquid crystal order, or "texture", prior to cross-linking. In this work, simulation-based methods are developed and partially validated for use in applications-focused design of temperature-responsive nematic LCEs. These methods enable the simulation of LCEs of macroscopic size and of non-trivial geometry through the use of continuum mechanics and suitable numerical methods (the finite element method). LC texture is an input parameter in the presented method, allowing many choices of texture to be explored at low cost given that the textures are physically accessible. In addition to methods development and validation results, proof-of-concept simulation-based design studies were performed for two types of LCE-based actuators that are of current interest in the field: grippers and hinge mechanisms. Finally, preliminary results are presented resulting from the integration of nematic texture dynamics simulation (pre-cross-linking) and LCE mechanical simulations (post-cross-linking) which address the two main sources of complexity in the design process of LCE functional materials.

Acknowledgements

I would first like to thank my advisors Professor Nasser Mohieddin Abukhdeir and Professor Boxin Zhao for jointly supervising me on this new project. I would also like to thank Professor Takeaki Araki for hosting me in his group at Kyoto University and sharing his resources.

I would like to thank Hamed Shahsavan for being my experimental collaborator and sharing his data and expertise, and Fred Fu and Tanyakarn Treeratanaphitak for much discussion and advice regarding Python, numerical methods, and `FEniCS`, as well as for Fred allowing me to use substantial amounts of his code.

Lastly, I would like to thank the sources of funding and resources that supported the work. For financial support, this includes the Ontario Graduate Scholarship (OGS) program, the Natural Sciences and Engineering Research Council (NSERC) of Canada, and the Waterloo Institute for Nanotechnology (WIN) Nanofellowship program. For computing resources, this includes the Shared Hierarchical Academic Research Computing Network (SHARCNET).

Table of Contents

List of Tables **x**

List of Figures **xi**

1 Introduction **1**

1.1 Objectives 2

2 Background **4**

2.1 Introduction to Liquid Crystals 4

2.1.1 Definition and Properties 4

2.1.2 Mathematical Description of the Nematic Phase 8

2.1.3 Anchoring and Alignment 9

2.2 Liquid Crystal Elastomers 12

2.2.1 Sensitivity to External Stimuli 12

2.2.2 Coupling of Liquid Crystalline Order and Macroscopic Shape 13

2.2.3 Soft and Semi-soft Elasticity 15

3 Theory **17**

3.1 Coarse-grained Molecular Models 17

3.1.1 Off-lattice Models 18

3.1.2 Lattice Models 20

3.2 Continuum Models 22
3.3 Hyperelastic LCE Model 26
3.3.1 Neo-classical Model 26
3.3.2 Anisotropic Extension to the Neo-classical Model 27
3.4 Finite Element Description 30

4 LC Mechanical Model Validation **34**
4.1 Material 34
4.2 Measurement of the Idealized Deformation 34
4.3 Hybrid Texture 40
4.4 Deformation of Cantilevers with Hybrid Texture 40
4.4.1 Characterization of deformation 41
4.4.2 Mesh Independence 42
4.4.3 Step Size Independence 44
4.4.4 Test for Hysteresis 47
4.4.5 Comparison With Experiment 48
4.5 Blocking Force of Cantilevers with Hybrid Texture 50
4.5.1 Blocking Force Procedure 51
4.5.2 Mesh Independence 52
4.5.3 Step Size Independence 52
4.5.4 Estimation of the Shear Modulus 54
4.6 Conclusions 59

5 Design Study of Multi-legged LCN Gripper **61**
5.1 Disk-shaped Domain 61
5.2 Flower-shaped Domain 63
5.3 Conclusions 67

6 Design Study of LCN Hinge Actuators **68**
6.1 Introduction . . . 68
6.2 Methods . . . 70
6.2.1 Hinge Angle Metric . . . 70
6.2.2 Nematic Texture Dynamics Model . . . 71
6.3 Results & Discussion . . . 73
6.3.1 Sensitivity of Bending Response to Various Parameters . . . 73
6.3.2 Bending Response of Pure TN Domains of Varying Length . . . 75
6.3.3 Nematic Reorientation Dynamics . . . 78
6.4 Conclusions . . . 85

7 Conclusions & Future Work **86**
7.1 Conclusions . . . 86
7.2 Future Work . . . 87

References **89**

A Derivation of Stress for Model **96**

B Explanation of Image Processing Methods **99**

C Raw Data Collected for Flower Petal Study **102**

D Documentation **103**
D.1 Measurement of the idealized deformation . . . 103
D.2 Characterization of deformation . . . 103
D.2.1 Setup . . . 103
D.2.2 Postprocessing . . . 104
D.3 Mesh Independence . . . 104
D.3.1 Setup . . . 104

D.3.2 Postprocessing 104
D.4 Step Size Independence 104
D.4.1 Setup 104
D.4.2 Postprocessing 105
D.5 Hysteresis of Deformation 105
D.5.1 Setup 105
D.5.2 Postprocessing 105
D.6 Comparison With Experiment 105
D.6.1 Setup 105
D.6.2 Postprocessing 106
D.7 Mesh Independence for Blocking Force 106
D.7.1 Setup 106
D.7.2 Postprocessing 106
D.8 Step Size Independence for Blocking Force 106
D.8.1 Setup 107
D.8.2 Postprocessing 107
D.9 Estimation of the Shear Modulus 107
D.9.1 Setup 107
D.9.2 Postprocessing 108
D.10 Factorial Study of Flower-shaped Domain 108
D.10.1 Setup 108
D.10.2 Postprocessing 108
D.11 Sensitivity of Bending Response to Various Parameters 109
D.11.1 Setup 109
D.11.2 Postprocessing 109
D.12 Bending Response of Pure TN Domains of Varying Length 110
D.12.1 Setup 110

D.12.2 Postprocessing 110
D.13 Nematic Reorientation Dynamics 111
D.13.1 Setup 111
D.13.2 Postprocessing 111

E Change-in-reference Procedure **113**
E.1 Mathematical formulation 114
E.1.1 Immediately after updating the reference state 114
E.1.2 Converting from the new to previous reference state 115
E.1.3 Idealized deformation gradient and stretch values 116
E.2 Validation 118
E.2.1 Forward iteration 119
E.2.2 Hysteresis 120

List of Tables

4.1 Simulation parameters for characterizing curvature metric 42
4.2 Simulation parameters for characterizing mesh independence of model . . . 44
4.3 Simulation parameters for characterizing step size independence of model . 46
4.4 Simulation parameters for characterizing hysteresis of model 47
4.5 Simulation parameters for comparing curvature in simulation and experiment 48
4.6 Simulation parameters for characterizing mesh independence of blocking force 53
4.7 Simulation parameters for characterizing step size independence of blocking force 54
4.8 Simulation parameters for characterizing relation between shear modulus and blocking force 56
4.9 Simulation parameters for estimating shear modulus 58

5.1 Simulation parameters for factorial study of flower-shaped domain 65
5.2 Fitted coefficients for effects of cuts on mechanical properties of radial hybrid domains. 66

6.1 Simulation parameters for factorial study of hinge actuators 74
6.2 Simulation parameters for variable-length TN hinges 77
6.3 Material parameters for 5CB. 81

C.1 Effect of cuts on mechanical properties of radial hybrid domains. 102

List of Figures

2.1 Atoms in a simple tetragonal lattice. 5
2.2 Atoms in a random arrangement viewed from two different angles. 6
2.3 Simulation of a nematic using coarse-grained ellipsoidal "rod-like" molecules. 6
2.4 Contribution of a single mesogen to nematic order parameter S. 8
2.5 Phase diagram showing magnitude of reduced nematic order with respect to reduced temperature of an LC in an applied field. 10
2.6 Order parameter as a function of temperature in a side-chain LCE. 13
2.7 Conformation of an LC polymer chain in the isotropic and nematic phases. 14
2.8 Experimentally-measured stress-strain curves of several LCEs exhibiting soft elasticity. 16

3.1 Schematic illustrating particle interactions in lattice and off-lattice coarse-grained simulations. 19
3.2 Deformation of an LCE with twisted-nematic texture showing saddle-like bending. 24

4.1 Sample image processing output of uniform planar-aligned LCN films with 50% M2 composition at two temperatures. 36
4.2 Image processing output of $\lambda_{\parallel}(T)$ and $\lambda_{\perp}(T)$ from sample with 50% M2 composition. 37
4.3 Fourth-order polynomial fits mapping $\lambda_{\parallel}$ and T for sample with 50% M2 composition. 37
4.4 Plot of relative volume versus temperature, measured from sample with 50% M2 composition, and mapped onto the incompressible regime. 38

4.5 Fourth-order polynomial fits mapping $\lambda_{\|}$ and T for sample with 12% M2 composition. 39
4.6 Plot of relative volume versus temperature, measured from sample with 12% M2 composition, and mapped onto the incompressible regime. 39
4.7 Schematic of the orientational alignment of a hybrid-aligned LCN film. . . 41
4.8 Sampled mesh vertices from various subsets of the full cantilever. 43
4.9 Relative error of curvature estimate as a function of cantilever aspect ratio. 43
4.10 Absolute error of position of cantilever tip for simulations of varying mesh densities. 45
4.11 Absolute error in position of cantilever tip for simulations of differing step size. 46
4.12 Normalized curvature versus temperature for the experimental and simulated LCN cantilever with 50% M2 composition. 49
4.13 Plot of the normalized curvature versus temperature for the experimental and simulated LCN cantilever with 12% M2 composition. 50
4.14 Relative error of blocking force for simulations of varying mesh densities, at $\hat{\lambda_{\|}} = 0.99$. 53
4.15 Relative error in blocking force for simulations of differing step size. 55
4.16 Relation between shear modulus and measured blocking force in simulation where $\hat{\lambda}_{\|} \approx 0.996036$. 56
4.17 Relation between blocking force and temperature for cantilevers with 50% M2 composition and dimensions. 57
4.18 Estimated shear modulus versus temperature for the LCN with 50% M2 composition. 58

5.1 An LCN-based gripper design presented in ref. 1 and the proposed monolithic design. 62
5.2 Schematic of the director field for an idealized radial hybrid texture. 62
5.3 Cutaway views of simulated deformations of an LCN disk and an LCN flower with a radial hybrid texture in response to temperature. 63
5.4 Top view of flower-like domain with eight cuts. 64

5.5 Force versus displacement for radial hybrid domains with cuts of varying number and dimensions. 66

6.1 Anchoring conditions for top and bottom surfaces used to make LCE with TN texture occupying 20% of the domain. 69

6.2 Experimentally-measured bending response of LCEs with different textures. 70

6.3 Visualization of hinge metric as applied to TN domain in un-deformed and deformed states. 71

6.4 Layout of domains in a hinge with 30% active region divided into 1 and 3 blocks. 74

6.5 Bending response to temperature for domains with hybrid texture, and TN texture. 76

6.6 Hinge angle observed at $\hat{\lambda}_{\|} = 0.98$ for TN domains of varying length and width. 77

6.7 Proposed anchoring orientation for hinge domain on top and bottom boundaries. 80

6.8 Both variations of in-plane direction of anchoring in texture modelling simulations. 82

6.9 Equilibrium texture of hinge made with naïve surface anchoring, and equilibrium biaxiality. 84

B.1 Intermediate steps of the image processing method used to measure the dimensions of LCE films. 100

E.1 Maximally-attainable deformation of a hybrid cantilever. 114

E.2 Error introduced by applying the change-in-reference procedure at different steps in a simulation while maintaining step direction. 119

E.3 Error introduced by applying the change-in-reference procedure at different steps in a simulation and reversing step direction. 121

Chapter 1

Introduction

Liquid crystal elastomers (LCEs) are a class of polymer networks which involve the incorporation of liquid crystal (LC) molecules into their polymer backbone or side chain [2]. This results in anisotropy in their mechanical, optical, and electromagnetic properties similar to those exhibited by traditional LC materials. Their mechanical properties are highly coupled with the internal state of LC order, which can result in large mechanical deformations as LC order changes. This can occur in response to a variety of external stimuli such as changes in temperature, exposure to light, and application of external fields.

This combination of properties makes LCEs highly promising candidates for a broad range of technological applications such as artificial muscles [3, 4], light-driven motors [5], jellyfish-like microfluidic pumps [6], and a stage for solar cells that tilts to follow the sun [7]. However, developing a new application using LCEs remains difficult, as the design space has a massive number of degrees of freedom and the physics are sufficiently complicated so as to result in mechanical models which require numerical analysis.

The two main contributors to the complexity of the design of LCE applications are the choice and imposition of liquid crystal order, or "texture", prior to cross-linking. The response of the LCE to external stimuli is largely determined by the LC texture. Traditional trial-and-error design strategies are infeasible due to the large design space of LC texture and complex coupling of the texture to the resulting mechanical response. For nematic LCEs, the LC order is purely orientational, and the texture corresponds to spatial variations in molecular alignment within the material. Imposing a desired nematic texture requires precise control of surface properties, device geometry, and the inherent material properties of the LCE precursor. Modern nematic alignment techniques are available which enable the imposition of highly complex nematic texture fields prior to cross-linking, but relating

these textures to a mechanical response is still an active area of research. Furthermore, the materials used in LCEs are often expensive, resulting in an additional barrier to iterative experimental design.

An example of the current state-of-the-art in LCE design is illustrated in an experimental study by Ware *et al.* They presented an LCE-based actuator which is flat at room temperature, but forms an array of large, sharp cones upon heating [8]. To demonstrate the mechanical performance of the film, the authors balance a load on top of it and show that it can lift objects many times its own weight. While these results are promising, further research is required to formally determine the performance of LCE actuators and how this performance changes with variations of the design and applied loading. Shahsavan *et al.* [1] demonstrate a characterization technique based on measuring the blocking force of an LCE-based actuator; that is, obstructing the deformation of an actuator and measuring the force required to oppose the deformation. This method has a more well-defined measurement, but requires additional equipment and is limited to actuators with relatively simple deformations, geometry, and application of stimulus. For twisting and other complex deformations, the issue of force measurement is substantially more difficult. These factors pose a challenge to the use of LCEs in technological applications, where it is desirable for a device to have well-understood performance characteristics.

Looking to other established applied fields, such as aerospace engineering, the semiconductor industry, and the pharmaceutical industry, a common thread is the use of computer simulations to offset the massive complexity faced in designing new products. Simulations allow for safe, cost-effective, and high-throughput design studies which may be used to inform and augment traditional experimental methods. They also permit far greater levels of automation in the design process, leading to further savings in time and resources.

1.1 Objectives

The overall goal of this research project is to develop applications-focused simulation methods for LCE design, specifically for temperature-responsive LCEs. These methods must enable the simulation of LCEs of macroscopic size and of non-trivial geometry, which motivates the use of continuum mechanics models. Specific objectives include:

1. Identify a suitable continuum model for temperature-responsive nematic LCEs.
2. Develop estimation methods for the model parameters for a specific LCE material.

3. For simple (single deformation mode) nematic textures, predict the thermomechanical response of an LCE domain, including deformation and blocking force.

4. Predict both the nematic texture prior to cross-linking and the resulting thermomechanical response by combining nematic texture and mechanical modelling.

The thesis is organized as follows. First, broad background information on liquid crystals and liquid crystal elastomers is presented to aid the reader in understanding the work (Chapter 2). Next, a mathematical model for LCEs is taken from the literature and described, along with details of the solution method for the model (Chapter 3). A series of tests are then performed on the model to investigate its accuracy and numerical properties. Both deformation and mechanical performance are measured (Chapter 4). A proof-of-concept design study is performed to show how the simulation method can be used to optimize the bending and mechanical response of an LCE for an example soft gripper application (Chapter 5). Finally, LCEs containing an arrangement of multiple textures are investigated. First, an optimal design for a hinge-like actuator is found. Then liquid crystal texture modelling techniques are applied in order to test whether the proposed design could be created using familiar surface anchoring techniques (Chapter 6).

Chapter 2

Background

2.1 Introduction to Liquid Crystals

2.1.1 Definition and Properties

Liquid crystals (LCs) are a phase of matter which flow similarly to liquids but exhibit some degree of elasticity similarly to crystalline solids [9]. The origin of these common properties is the orientational and translational order of the constituent molecules, which can depend on the type of LC phase. Order can be generically defined as the presence of a well-defined structure of the constituent parts of a material. For instance, in most solid crystals, the atoms are arranged in periodically repeating structures called unit cells. If the position of one atom within a unit cell is known along with the unit cell orientation, the positions of other atoms in the crystal can be determined. This *positional* order is, in the case of crystals, *long-range* in that this order is maintained over large length scales far beyond the immediate neighbours of the unit cell.

Since the unit cells all share a well-defined orientation, the material properties of a crystal are anisotropic. That is, its physical properties (refractive index, mechanical strength, *etc.*) vary depending on orientation with respect to the unit cell. This can be loosely understood by considering that many physical properties depend on the arrangement and spatial frequency of the atoms of the material. In Figure 2.1, the atoms of a tetragonal lattice (where the unit cell is a rectangular prism with two equal axes and one unique axis) are shown from two different angles. Although the underlying structure is the same, the arrangement and spatial frequency appear different when viewed from different angles—it

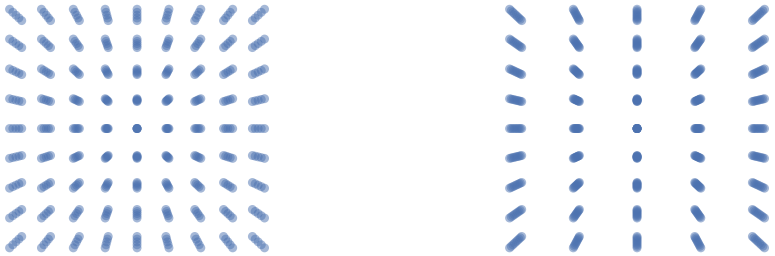

(a) (b)

Figure 2.1: Atoms in a simple tetragonal lattice viewed (a) along and (b) perpendicular to the unique axis.

is for this reason that light passing through such a lattice at different angles is refracted differently.

A disordered material, in contrast, has molecules which are uniformly but randomly dispersed throughout its volume as shown in Figure 2.2. If inspected from any angle, the distribution of molecules appears (statistically) identical and the properties of the material will thus be isotropic. This is the case for amorphous solids and fluids.

There are many different types of LC phases, but the focus of this work is on nematics. Nematics do not have positional order, but they do have long-range *orientational* order [10, 11]. Their constituent molecules have a well-defined internal orientation and are often categorized as "rod-like" or "disk-like" based on their approximate shape. This anisotropy in their shape results in it being favourable for neighbouring molecules to be aligned parallel or anti-parallel with each other and unfavourable for them to be aligned perpendicular to each other [11]. This leads to the emergence of a preferred molecular orientation shared by the constituent molecules over a large region relative to the molecular scale. Unlike in a crystal, the orientational ordering is not perfect and may be described through a spatially-varying orientational distribution function [11]. A visualization of a nematic LC can be seen in Figure 2.3.

Since the discovery of LCs over a century ago, a wide variety of LC phases has been discovered. Accordingly, many different molecules which give rise to one or more of these

(a) (b)

Figure 2.2: Atoms in a random arrangement viewed from two different angles.

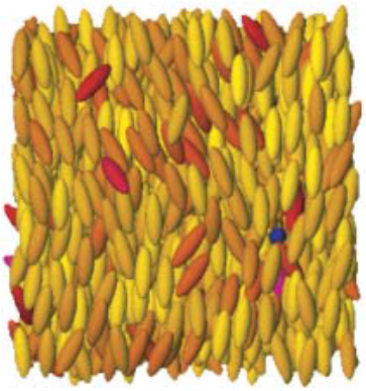

Figure 2.3: Simulation of a nematic using coarse-grained ellipsoidal "rod-like" molecules. The long axis of the ellipsoid indicates orientation and colour indicates agreement between the individual molecular orientation and the average orientation within the entire domain. Figure taken from [12].

phases have also been discovered. These molecules are called mesogens. Mesogens can be integrated into other molecules, such as a side-chain group of a polymer, which may impart the polymer with LC properties [11].

LC order is sensitive to external stimuli and can be easily distorted or modified without disrupting the stability of the phase. Thermotropic LCs are most affected by changes in temperature. As the temperature is lowered below the LC/solid phase transition temperature, the LC freezes into a solid, and as the temperature is raised above the LC/liquid phase transition temperature, the LC "melts" into an isotropic liquid. Between these critical temperatures, the magnitude of LC order varies substantially with respect to changes in temperature [11].

LCs are also susceptible to electric and magnetic fields, which can distort or reorient orientational order in the case of nematics [11]. If an LC is placed between a set of electrodes, this effect can be used to dynamically control the state of orientational order in the LC. Boundary or "anchoring" conditions at a solid/LC or fluid/LC interface can also strongly affect LC order. Based on the interaction between the LC and the opposing surface, a preferred direction of orientational order at the interface is defined. This preferred direction will propagate to part or all of the domain. If the different boundaries of the domain have differing preferred anchoring direction, the resulting LC order will be a compromise between the conflicting boundary conditions, which may involve continuous or discontinuous changes in the preferred direction [11].

The most well-known application of LCs is the liquid crystal display (LCD), which takes full advantage of the aforementioned LC properties [11, 13]. Although many LCD designs exist, notably twisted-nematic (TN) and in-plane switching (IPS) types, they all operate similarly. The area of the display is divided up into a grid of pixels which act as individual tunable light "shutters". Behind the display is a polarized light source, typically referred to as a backlight. The amount of transmission through the LC layer, which depends on the LC alignment, can be varied through the application of a spatially varying electric field. By using the electrodes to control alignment, the brightness of each pixel can be controlled separately, allowing arbitrary images to be displayed. The different LCD designs that have been developed over many decades of research and the blend of LC components and cell geometry must be carefully optimized to achieve low power usage, fast switching between different images, high contrast, and good viewing angle over a wide range of temperatures [11].

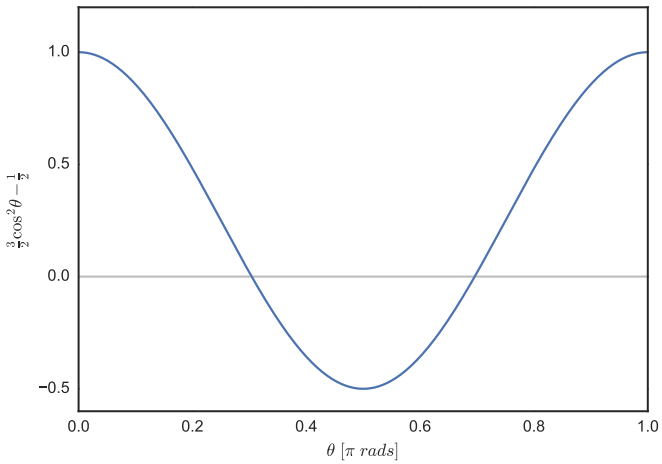

Figure 2.4: Contribution of a single mesogen to nematic order parameter S.

2.1.2 Mathematical Description of the Nematic Phase

Nematic order may be mathematically described through the introduction of a vector order parameter $\boldsymbol{n}$ and a scalar order parameter S. $\boldsymbol{n}$ is also referred to as the *director*. Both may vary in space and quantify the average molecular orientation and the degree to which the mesogens conform to that orientation, respectively. These order parameters are related through a molecular description of the nematic phase:

$$S = \left\langle \frac{3}{2}\cos^2\theta - \frac{1}{2} \right\rangle \tag{2.1}$$

where θ is the angle between an individual mesogen and $\boldsymbol{n}$ and angle brackets denote an ensemble average. A plot of the expression inside the angle brackets is shown in Figure 2.4 to visualize the value of individual contributions to S.

When $S = 0$, mesogens are randomly oriented, and the nematic phase is not present. When $S = 1$, mesogens are perfectly aligned with the director; this phase may bear more resemblance to a crystal than a typical nematic. Mathematically, it is possible for S to take on values as low as $-1/2$, which corresponds to a situation where all mesogens are perpendicular to the director. However, this is highly unphysical under normal conditions [10].

While this scalar/vector order parameter description is intuitive, it is not ideal for describing the nematic phase in that typical nematic mesogens are not polar. Thus it

is more appropriate to represent the nematic orientation in a form where $\boldsymbol{n}$ and $-\boldsymbol{n}$ are mathematically equivalent. One such representation is through the formulation of an alignment or "Q" tensor [11, 10]:

$$\boldsymbol{Q} = S\left(\boldsymbol{N} - \frac{1}{3}\boldsymbol{\delta}\right) \tag{2.2}$$

where $\boldsymbol{N} = \boldsymbol{nn}$ and $\boldsymbol{\delta}$ is the identity tensor. The alignment tensor is necessarily symmetric and typically formulated to be traceless.

In the vicinity of strong distortions of nematic order it is possible for there to be two distinct orientational axes of alignment, which is known as *biaxial* nematic order. To accommodate this, the alignment tensor can be written in a general form [10]:

$$\boldsymbol{Q} = S\left(\boldsymbol{nn} - \frac{1}{3}\boldsymbol{\delta}\right) + P\left(\boldsymbol{mm} - \boldsymbol{ll}\right) \tag{2.3}$$

where P is the biaxial order parameter, $\boldsymbol{m}$ is the director corresponding to the second orientational axis, and $\boldsymbol{l}$ is a vector mutually perpendicular to $\boldsymbol{n}$ and $\boldsymbol{m}$. $\boldsymbol{n}$ is chosen so that it is the eigenvector of $\boldsymbol{Q}$ with the largest corresponding eigenvalue. Thus $\boldsymbol{Q} = \boldsymbol{0}$ corresponds to the isotropic phase, and $S > 0, P = 0$ corresponds to a uniaxial nematic, in which there is only one orientational axis of alignment. Clearly, $\boldsymbol{Q}$ captures the orientation and magnitude of both uniaxial and biaxial order, and if $\boldsymbol{Q}$ is known, these quantities can be isolated and solved for.

Within the nematic phase, order gradually decreases as temperature increases. Since the nematic-isotropic transition is first-order, there is a discontinuous jump in the value of the order parameter between the nematic and isotropic phases [11]. However, when the LC is placed in an applied field (which includes mechanical as well as electromagnetic fields), the discontinuity shrinks until the field strength reaches a critical magnitude upon which the discontinuity vanishes completely [14], which is sometimes termed the "paranematic" phase. This can be qualitatively seen in Figure 2.5, where the nematic order is plotted as a function of temperature in reduced units for the case of no applied field (leftmost series) and increasingly strong applied fields.

2.1.3 Anchoring and Alignment

As previously mentioned, it is possible to impose a desired alignment on LCs through the application of surface anchoring and external fields. Depending on the chemical species,

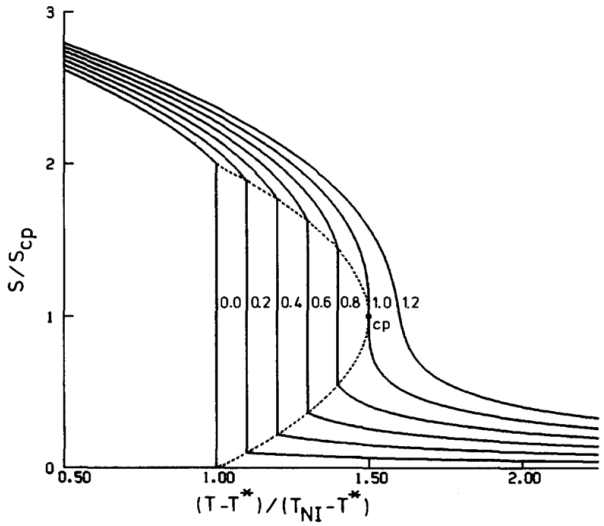

Figure 2.5: Phase diagram showing magnitude of reduced nematic order with respect to reduced temperature. Leftmost series corresponds to thermodynamic equilibrium, while the following series show the phase diagram when the LC is placed under increasingly strong applied fields. The series labelled '1.0' shows the phase shows a sample subject to the critical field strength. Figure taken from [14].

mesogens may prefer to align parallel or perpendicular to electric fields [11], and this effect is of key importance in developing applications of LCs. Surface anchoring can be categorized as homeotropic in the case that mesogens prefer to align perpendicular to the interface and planar in the case that mesogens prefer to align parallel to the interface. Planar anchoring can again be divided into uniaxial planar and degenerate planar, in the case where there is and is not a preferred in-plane direction, respectively.

Different types of surface anchoring may have different degrees to which they affect nematic order. For analytical calculations, this tends to be ignored for simplicity; it is assumed that the mesogens at the surface perfectly obey the surface alignment, which is known as "strong" anchoring [11]. However, in numerical simulations, it is (comparatively) straightforward to account for differences in anchoring strength. In these cases, a surface anchoring potential energy can be specified.

In order to impose homeotropic anchoring, one well-known method is to treat the surface of the cell containing the LC with a layer of amphiphilic molecules [11]. Additionally, homeotropic anchoring is also weakly imposed at gas/LC interfaces [15]. In order to impose uniaxial planar anchoring, one well-known method is to coat a polyimide layer on the cell, and then mechanically rub the surface along the desired axis of alignment (e.g., with a cloth) [11, 16].

While these simple methods cover the whole cell with the same anchoring conditions, other methods of anchoring are amenable to patterning, whereby the surface anchoring can be controlled with high spatial resolution, depending on the method used. For instance, Ichimura *et al.* demonstrate a photo-alignment technique where the anchoring film responds to UV light [17], allowing either homeotropic or planar anchoring to be chosen. By combining this technique with conventional photolithography, micron-scale surface anchoring can be prepared. Schadt *et al.* demonstrate a similar technique where polarization is used to select the preferred in-plane direction [16].

Fukuhara *et al.* use an anchoring agent that self-assembles at the air/LC interface [15], as opposed to being coated on the solid/LC interface. It also imposes planar-axial anchoring in response to polarized light, allowing the planar orientation to be chosen along with the additional advantage that it can be used with non-flat interfaces.

A review of other methods for high-resolution (sub-micron-scale) alignment can be found in ref. 18.

2.2 Liquid Crystal Elastomers

Liquid crystal elastomers (LCEs) are a class of solids that are made from LCs. Some of their properties are inherited from LCs, and some are unique. As previously mentioned, it is possible to incorporate LC mesogens into a polymer backbone or side chain. If the coupling between the mesogens and the polymer is sufficiently strong, it results in a LC polymer (LCP)—a polymer where the chain conformation is not random, but at least partially ordered due to the presence of mesogenic polymer units [2]. Such polymers are referred to as main-chain or side-chain, depending on where the mesogen is incorporated.

LCPs are interesting in their own right, but if the chains of the LCP are then cross-linked into a network, an LCE is formed which has several intriguing properties. After cross-linking has been completed, the orientational order inside an LCE does not drift or distort in absence of the aligning factors that created it due to the presence of the cross-links [2]. Just as with the nematic LC phase, nematic LCEs represent the main area of research in the field and thus the background will be focused on this class of LCEs.

In the literature, a distinction is sometimes made between LCEs and liquid crystal networks (LCNs), which have the same chemical composition but a very high concentration of cross-links. In this work, LCE will be used as a general term, and LCN will be used to specify a densely cross-linked LCE where appropriate.

2.2.1 Sensitivity to External Stimuli

Like nematic LCs, nematic LCEs have some amount of orientational order which is responsive to external stimuli. Temperature greatly affects the magnitude of orientational order present in the LCE, with higher temperatures leading to a decrease in order [2]. At elevated temperatures, the nematic phase undergoes a phase transition to the isotropic phase. The temperature at which this occurs is called the nematic-isotropic transition temperature, above which the LCE has isotropic properties, similar to a standard elastomer. However, this phase transition is typically not abrupt as in traditional LCs, but "smeared" out [2]. An example of this is shown in Figure 2.6 where the phase behaviour of the LCE is similar to that of a traditional LC under the influence of an external field (see Figure 2.5). This observed behaviour is thought to be due to either internal mechanical stress fields resulting from the covalent bonds of the cross-links [2, 19, 20] or other sources of heterogeneity [21]. Additionally, cross-linking while the LC polymer is in the nematic phase leads to an LCE with an increased nematic-isotropic transition temperature, while cross-linking in the isotropic phase causes an opposite effect [2].

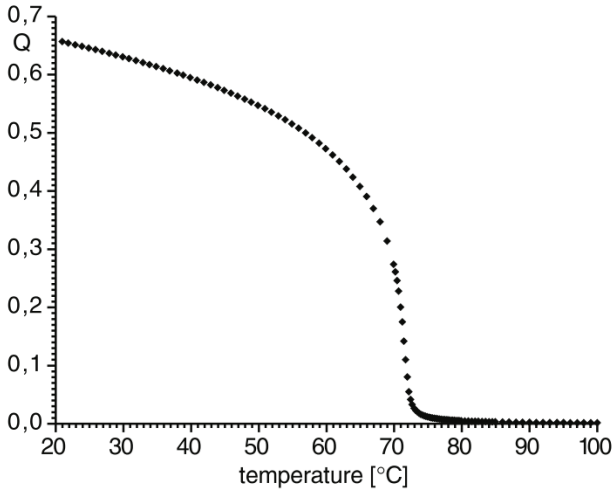

Figure 2.6: Order parameter as a function of temperature in a side-chain LCE. Figure taken from [22].

The orientational order of LCEs is nominally sensitive to electric [23] and magnetic fields. However, this effect is difficult to observe as the mechanical stiffness of the LCE is large in comparison to the susceptibility of the LCE to external fields [24, 25]. To improve the sensitivity of LCEs to external stimuli, they can be integrated with other compounds. For instance, several groups have reported making a UV-sensitive LCE by integrating azobenzene-based compounds into the polymer network [26, 5, 27, 28, 29]. Others have used compounds such as carbon nanotubes in order to convert absorbed light into heat [7, 30]. Similar approaches have been used to enhance the response of LCEs to magnetic fields [31].

2.2.2 Coupling of Liquid Crystalline Order and Macroscopic Shape

If the nematic order within an LCP molecule changes, so does the average conformation of the chain. In the isotropic state, the polymer behaves as a Gaussian chain on a random walk. In the nematic state, the chain has a greater tendency to lie parallel to the director. In this case the radius of gyration is anisotropic, and the LCP extends along the director while contracting along the other axes [2], which is illustrated in Figure 2.7. Since the magnitude of nematic order is a continuous quantity, this change in shape is also continuous, changing smoothly with temperature.

A similar process occurs in LCEs except, unlike in LC polymer melts, an LCE solid will

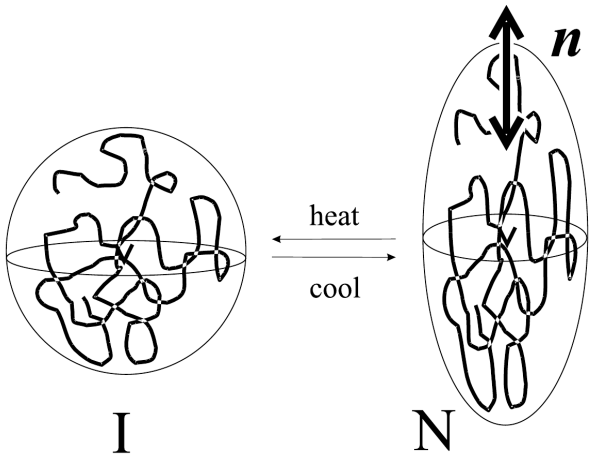

Figure 2.7: Conformation of an LC polymer chain in the isotropic and nematic phases. Figure taken from [2].

macroscopically deform as the magnitude or orientation of nematic order changes [2]. This is again due to the cross-links which tightly couple constituent polymers to their neighbours and to the entire solid. As the conformation of one polymer chain changes shape, so do those of neighbouring polymer chains, due to the coupling effect of the cross-links.

If the nematic director is uniform, the deformation of the solid matches that of the individual molecules; i.e., there is uniaxial expansion and contraction along the principal axes of the material. However, if there are gradients or discontinuities in the director, the axes of expansion and contraction will vary throughout the material. This results in far more complex deformations.

Depending on characteristics of the liquid crystal order imposed at the time of cross-linking, a myriad of different deformation modes can be imprinted into the LCE. These range from simple deformations, such as extension, bending [32], and twisting [28], to complex deformation modes, such as self-folding origami [8] and bas-relief images [33]. This coupling also functions in the opposite direction; that is, mechanically stretching and compressing the LCE results in reorientation and change in magnitude of the underlying LC order [2]. This property is utilized in the Finkelmann method, an early technique for producing well-aligned LCE domains [24]. To start, a LC polymer is cooled to the nematic phase and lightly cross-linked. This produces a polydomain LCE, where there are many small nematic domains pointed in different directions. Next, the LCE is lightly (as it is mechanically weak without further cross-linking) stretched in a chosen direction, causing the individual domains to reorient toward the direction of stretching. Then a much more

extensive cross-linking process is performed with the LCE in this stretched state. This produces a uniaxial nematic LCE, though the initial cross-links remain in a permanently strained state.

Incidentally, without the Finkelmann method, it is challenging to produce well-aligned LCEs, as LC polymers are much slower to respond to the alignment methods used with typical LCs [24, 25]. An alternative method, demonstrated by Broer *et al.*, is to instead align the LC monomer and subsequently photopolymerize [25]. If the monomer has suitable chemical functionality, this will create a densely cross-linked elastomeric network.

The coupling of order and shape in LCEs is quite strong. Subsequently, the mechanical response of the LCE can be very large and they have been observed to exhibit strains of up to several hundred percent when transitioning from the isotropic to the nematic phase [34, 35].

2.2.3 Soft and Semi-soft Elasticity

Soft elasticity is perhaps the most unusual property of LCEs. It refers to the phenomenon where the LCE, when subjected to certain mechanical stresses, deforms without resistance. That is, there is a continuous set of states of deformation along which the change in the overall potential energy of the system is negligible. In a standard stress-strain curve, this appears as a plateau, after which the curve resumes a more typical trajectory. A distinction is sometimes made in terminology, where for soft elasticity the plateau begins at the origin, and for semi-soft elasticity the plateau begins after some initial threshold stress. The onset of the plateau appears to be correlated with the shear modulus of the LCE and the anisotropy of the polymer backbone [36], meaning that stiffer LCEs and main-chain LCEs, which naturally have higher backbone anisotropy, exhibit soft elasticity at higher threshold stresses. Several examples of soft elasticity are shown in the stress-strain curves in Figure 2.8.

The origin of the phenomenon lies in the reorientation of the director [20, 38, 37]. The energetic cost of mechanically deforming the cross-links and changing the polymer conformation is offset by the improved alignment of the mesogens. This class of deformations is known as a Goldstone mode [20], and theoretical models for LCEs aim to reproduce it. An explicit form for the Goldstone modes of an early model can be found in ref. 39.

Soft or semi-soft elasticity is not observed in every sample or loading configuration [40]. Even if the sample is deformed by the loading, the accompanying director reorientation may not be sufficient to cause a plateau in the stress-strain curve, or may not occur at

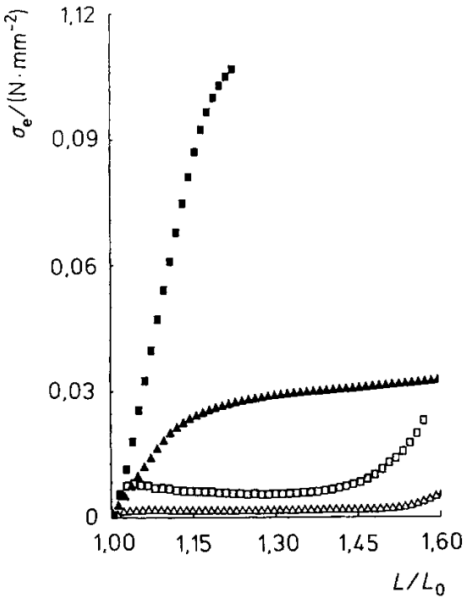

Figure 2.8: Experimentally-measured stress-strain curves of several LCEs of the same composition exhibiting soft elasticity at different points. Figure taken from [37].

all. The variety of LCE materials and synthesis conditions results in many differences in observations [20].

Despite theoretical predictions of soft elasticity [41], in experiments it is generally semi-soft elasticity that is observed (if any soft response is observed at all) due to various non-idealities [2]. One method of observing a soft response is to simply make a polydomain LCE (i.e., cross-linking at high temperature and cooling) and apply a uniaxial stress in any direction [42]. The domains will simultaneously reorient to the direction of applied stress. Alternately, one can start with a uniaxial LCE, and apply a uniaxial stress perpendicular to the director [20]. In this case, the theory predicts [2, 43] (and experiment demonstrates [44]) that the reorientation occurs in alternating stripes in the LCE where the director rotates in opposite directions.

Chapter 3

Theory

In this chapter the different classes of mechanical models for LCEs are briefly reviewed, focusing on those models which are able to capture experimentally relevant length and time scales. The hyperelastic continuum model [32, 45] used in this work is then presented within the context of the current state-of-the-art. Finally, the variational or "weak" form of the continuum model is derived for numerical solution via the finite element method.

3.1 Coarse-grained Molecular Models

Coarse-grained molecular models approximate molecules as particles such that, to some degree, the internal degrees of freedom of the molecules are neglected. For LCE models, similar to most course-grained models for polymers, bead-spring models have been used where polymer molecules are approximated as the combination of particles (beads) and bond potentials (springs). These types of models for traditional polymers and elastomers have been an area of intense study over the past several decades. Much of the research on LCEs using these types of models involves the use of molecular interaction potentials (force fields) which account for the molecular anisometry which is inherent to molecules which exhibit liquid crystalline phases.

For many molecular systems, coarse-grained models are considered relatively simple to construct. Even if the initial conditions are slightly unphysical, a system can be expected to relax to a physically realistic state in the normal course of running a simulation. For polymeric or glassy systems, there are some added difficulties since relaxation times may become impractically long. LCEs share that problem, but the presence of cross-links poses

an even greater challenge. Since they are distributed in the LCE in a random fashion, the exact structure of the LCE is unknown. Still, many complicated scenarios are conceivable, such as a polymer strand knotting around several other strands before being cross-linked to itself. Since they are permanent parts of the structure, relaxation will not help in making the initial conditions more physically realistic. These random and poorly-defined features of the LCE may have a large impact on the measured results, especially if the simulated system is small.

Finally, the parameters used in coarse-grained potentials typically do not directly correspond to macroscopically measurable quantities. Through extensive experimentation and simulation, it may be possible to tune all of the model parameters to reproduce the physical properties of a particular material, but this would likely be time-consuming and has no guarantee of success.

As an aside on terminology, coarse-grained models are generally categorized as lattice or off-lattice. In lattice models, individual particles (which may represent a group of many polymer molecules) are only permitted to occupy positions defined by points on a regular grid. Particle-particle interactions are also defined by the lattice; typically, a particle will only interact with its nearest and perhaps second-nearest neighbours.

In contrast, particles can move continuously through space in off-lattice models, and they typically interact with all other particles that drift within a specified radius.

This is briefly depicted in Figure 3.1.

3.1.1 Off-lattice Models

The majority of LCE research involving off-lattice models utilize Gay-Berne type potentials [46, 47] for mesogenic particle-particle interactions and the FENE potential [48] for particle bonds.

Skačej and Zannoni have performed several molecular Monte Carlo simulations of LCEs. In ref. 49, a system of LCEs is subject to changes in temperature and applied stress, and a variety of measurements familiar to experimental researchers, such as X-ray diffraction, are performed. To create the system, polymer strands are made from soft-core Gay-Berne beads bonded with FENE springs, simulating a main-chain LC polymer. After the polymer strands are initialized, they are aligned in an electric field and an additional 2 FENE bonds are added randomly between each strand and its neighbouring strands to lightly cross-link the system. Lastly, additional Gay-Berne particles are introduced to act as a swelling agent. Some features of LCEs are qualitatively reproduced by these simulations.

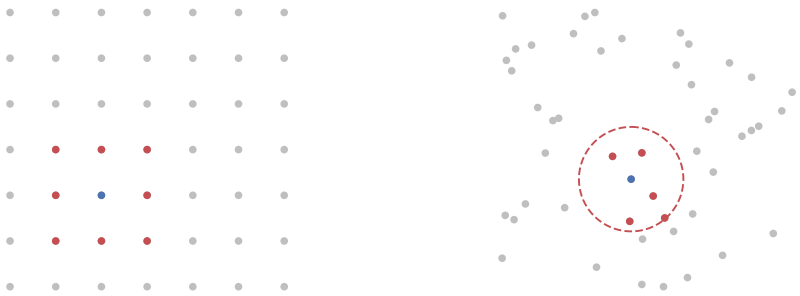

(a) (b)

Figure 3.1: Schematic illustrating particle interactions in (a) lattice and (b) off-lattice coarse-grained simulations. A particle of interest is shown in blue, and the particles it interacts with are shown in red.

A nematic-isotropic transition, as well as a smectic-nematic transition, another well-known LC transition, are observed along with corresponding uniaxial changes in the shape of the domain. Furthermore, the temperature of the nematic-isotropic transition is shifted higher than that of the equivalent monomeric system. Additionally, soft elasticity is observed when stress is applied to the domain starting in an isotropic state. However, the nematic-isotropic transition is sharp rather than smooth, and the elastic modulus observed is more than 10 times that of a comparable experimentally-characterized LCE. The authors ascribe these problems to the artificially high order of the system due to their method for generating initial conditions. In ref. 48, a similar system is investigated which is also subject to an electric field. Following an earlier experimental work [50], they are able to use an electric field to drive the system from isotropic to nematic, and also to rotate the director in an already nematic system.

Ilnytskyi *et al.* [51] perform molecular dynamics simulations of LCEs as well as equivalent LC polymer systems, notably studying a smectic instead of a nematic phase. They prepare a smectic LCE, as well as an equivalent smectic LC polymer, and investigate the presence of a memory effect in the shape of the domain when the system is heated to an isotropic state, then cooled again to a smectic phase. It is found that while both systems recovered orientational order after subsequent cooling, the LCE recovered its original shape, while the LC polymer did not. Additional simulations were run with applied stress at constant temperature, again showing that the LCE was capable of partially recovering its original shape when the stress was removed, while the LC polymer behaved more like a

viscous fluid and could not sustain the same levels of applied stress. Due to their sample preparation method, a more random and heterogeneous network was formed, with multiple independent sub-networks of LCE in the domain. However, discussion on the impact of this was limited in the paper.

Whitmer *et al.* [36] run large-scale molecular dynamics simulations to illuminate the microscopic details of a polydomain LCE re-orienting into a monodomain LCE under external stress. They use 77,824 particles in total so that a polydomain structure can be represented without significant finite size effects, though they prepare the system so that there are no entanglements of chains, which may not be realistic. When the domain is strained at a finite rate, semi-soft elasticity is reproduced in the stress-strain curve, but is highly dependent on the strain rate, qualitatively matching experimental results [52] referenced in the paper. However, when the strain rate is zero (i.e., the system is at equilibrium), the plateau associated with soft elasticity disappears, and a linear trend is observed. To characterize the polydomain-monodomain transition, the authors define individual domains by spherical clusters of particles with a local order parameter exceeding a particular threshold. During the transition, they observe domains rotating to a common director, and eventually merging together, illustrating the microscopic mechanism of the transition.

Skačej and Zannoni [53] similarly study a polydomain LCE but with Monte Carlo, using up to 216,000 particles. However, they deliberately introduce many non-idealities into the network when choosing initial conditions. Their polymer strands have random lengths and are initially oriented in random directions. Cross-links are introduced by linking the end of one polymer strand to the middle of another, resulting in a highly entangled and spatially heterogeneous network. In an equilibrium stress-strain experiment, they reproduce the plateau associated with soft elasticity as expected; this is in contrast with Whitmer *et al.*'s result, but due to the entanglements it is difficult to say with complete certainty whether they are truly at equilibrium or not. They reach a similar conclusion that the molecular origin of semi-soft elasticity is simultaneous domain growth and reorientation.

3.1.2 Lattice Models

Some work, particularly in earlier years, has successfully applied lattice models to improve the theoretical understanding of LCEs.

One prototypical example is Pasini *et al.*'s work [54]. Physical deformation of the lattice is assumed to be completely homogeneous, so only simple and uniform deformations are permitted. However, the director at each lattice point is allowed to re-orient. By using

a spatially invariant coefficient for the nematic interaction term of the Hamiltonian, a monodomain lattice is created that is well-aligned at low temperatures and isotropic at high temperatures. Lattices with varying degrees of polycrystallinity are also made by choosing a random value for the coefficient for each pair of neighbours in the lattice; different distributions of random values are used for different amounts of polycrystallinity. In pairs of neighbours where the sign of this coefficient is negative, perpendicular alignment is promoted, leading to a polydomain structure being favoured at low temperatures. Stress-strain curves are measured with stress oriented along the z-axis, which is defined as the director for the homogeneous samples. In the homogeneous samples, increasing applied stress drove isotropic samples into a nematic state and elongated them, and the already-nematic samples elongated slightly without the order changing. With the exception of the sample held at the transition temperature itself, the transition in the initially isotropic samples was relatively sharp, however, resembling the first order transition characteristic of nematic LCs, not LCEs. For samples of increasing polycrystallinity, the transition temperature fell and became more smeared out, as is more typically observed in LCEs.

A lattice model is also used in Selinger and Ratna's work [21], which studied the theoretical origin of the smeared out phase transition of LCEs. They introduce two forms of quenched disorder to their lattice model in order to deliberately try to smear out the phase transition, and then measure the temperature phase diagram while subjecting their lattice to varying levels of mechanical stress. The first form of disorder is "random-bond disorder", which is the spatial variance of the strength of nematic interactions between neighbours. This is similar to Pasini *et al.*'s approach [54], though negative coefficients are not considered here. The authors use this to represent chemical heterogeneity in the material. The second form is "random-field disorder", which is a spatially-varying field promoting alignment in different directions throughout the material. The authors use this to represent a heterogeneous internal mechanical stress distribution which could be caused by the presence of randomly-oriented cross-links which locally influence the director. Both forms of disorder are applied in the domains, where inside a domain there is no local disorder. When no disorder is present, the authors observe a typical nematic phase diagram with a first-order nematic-isotropic phase transition, which is slightly smeared out when external mechanical stress is applied; this is accompanied by a change of the lattice dimensions typical for LCEs. When both forms of disorder are tested independently, both are found to contribute to the smearing of the phase transition, so long as the domain size is sufficiently large. The fact that a broadening of the transition is seen for "random-bond disorder" is particularly significant, as it shows that even LCEs prepared with little-to-no "random-field disorder" can still exhibit this phenomenon.

In these previous papers, a substantial limitation is that the lattice can only sustain

very simple deformations, since a rectangular lattice is used and the lattice dimensions of each cell must be commensurate. In Skačej *et al.*'s work, their Monte Carlo moves include plane dislocations of rows of the lattice, allowing for some shear deformation to occur [55]. While this allows the phenomena of semi-soft elasticity to be explored, it still limits the model to relatively simple deformations. This by itself precludes lattice methods for use in most applications, since many of the capabilities of LCEs make use of more complex deformations; furthermore, the design of actuators that have purely uniaxial deformations is simple enough that the benefits of simulation are much more modest.

Finally, like off-lattice coarse-grained models, the parameters used in lattice models may not directly correspond to macroscopically measurable quantities, which adds difficulty in using the model for working with particular materials.

3.2 Continuum Models

Continuum models for LCEs are based on continuum mechanics [56], where the length and time scales being modelled are assumed to be much larger than those characteristic to the molecular description of the material. Existing continuum mechanical models for solids involve phenomenological approximations for the relationships between stress and strain at every point of the continuum. The most simple of these relationships is linear elasticity (Hooke's Law) which is only valid for relatively small strains [56], unlike those experimentally observed for LCEs. It is termed linear since it states that when a material is subject to stress, it deforms by an amount that is linearly proportional to the amount of stress. More general nonlinear elastic models are needed for LCEs which also take into account anisotropy of the stress-strain relationship resulting from nematic order. Additionally, many existing models assume that LCEs are incompressible [2] which, as will be seen, is not always the case.

Continuum methods for LCEs are generally based on extensions to rubber elasticity; in particular, a common element is so-called "neo-classical elasticity" [2, 57, 58]. This is an anisotropic form of neo-Hookean rubber elasticity, which assumes that the conformation of individual polymer strands can be described by a three-dimensional random walk, and it completely neglects collisions or interactions between strands [2]. Continuum models are generally solved using numerical methods, predominantly the finite element method.

Continuum methods can be applied to simulate much larger length and time scales, and as such, much of the literature surrounding them involves simulating devices to solve particular design problems. Design problems are typically posed as sets of requirements

that must be met. To solve the problem, a design that satisfies all requirements must be found. In most cases, it is possible to take a design as input and use a model to predict whether or not the design satisfies the requirements. But what is actually desired is a way to supply the requirements as input and have the model produce a design as output. This is known as an inverse problem, and for most models it is difficult or impossible to solve in the general case.

Aharoni *et al.* [59], however, claim to have solved the inverse problem for the case of approximately two-dimensional LCE films, so long as the desired deformation has axial symmetry. That is, given a desired three-dimensional shell or surface that can be expressed as a surface of revolution, they can find a texture that will reproduce it when the texture is imprinted on a flat LCE film which is subsequently heated. In their approach, they assume that the LCE expands and contracts ideally and uniaxially according to the local director and use methods from differential geometry to compute the metric tensor and thus the local curvature along each axis. Then, they find a general form for the metric tensor for any surface of revolution, and work backwards to find the required director field. While the utility in this design is clear and the thin-film geometry has broad potential applications, the inability to simulate thicker domains limits its general usefulness.

Lin *et al.* [60] take the neo-classical model and couple it with light-based actuation. They focus on azobenzene-based actuation, where the molecular conformation of part of the chemical structure switches between *cis* and *trans* upon exposure to UV light and subsequently drives a change in the LC order. They account for saturation of this change of conformation, as well as the nonlinear absorption of light through the depth of the material. They simulate deformation of an LCE in a shear-stress loading configuration, allowing them to confirm their results by comparison with an analytical solution. However, they only demonstrate their model on a two-dimensional domain, using a linearized mechanical model to get their results. These simplifications limit their model to infinitesimal strains and sufficiently symmetric domains, significantly restricting the types of design that can be done. Furthermore, dynamic illumination is not considered—that is, ideally, as the domain deforms, the illumination of light should cover a different spot on the domain and cause further deformation, which is a key point of interest in light-driven LCEs. For example, in Serak *et al.*'s experimental work [61], an LCE cantilever is driven by a laser to oscillate as fast as 270Hz; although the light source is stationary, it strikes different parts of the LCE as the LCE deforms, causing an oscillatory feedback loop.

Fuchi *et al.* [62] demonstrate an interesting proof-of-concept for approximately solving the inverse problem, applied to find an optimal texture for creating films exhibiting hinge-like bending deformation in response to temperature. Using a simplistic and empirical model, the deformation of an LCE film with a given input texture is found. In order to

Figure 3.2: Deformation of an LCE with twisted-nematic texture showing saddle-like bending. Figure taken from [63].

find the optimal texture for a hinge, a cost function is defined that computes the difference in the shape of a deformation from the desired hinge-like shape. A simple rectangular block of 90° twisted-nematic texture has been previously used in the literature for constructing hinges; however the deformation has some saddle-like character (shown in Figure 3.2), which the authors claim is problematic when many hinges are combined in the same film, as neighbouring hinges can interfere with each other and cause improper folding.

A topological optimization problem is then posed, to find the texture that results in a hinge with a less saddle-like fold. A fixed proportion of the domain is assumed to have no nematic order, and is "inactive" in the model, while the remainder of the domain has nematic ordering. Due to the alignment method used, the director is limited to having in-plane orientations on the top and bottom boundaries. Thus, only planar and twist textures are permitted. The spatial arrangement of ordered and disordered parts, and the texture of the ordered parts, are the main variables in the design problem. Due to the computationally expensive nature of the optimization process, the mechanical model is linearized during this part. The authors recognize that while a nonlinear model is needed to accurately model the deformation for large strains, the basic features that they are trying to optimize emerge even at small strains, so a linear model is justifiable.

After finding an optimal texture for a hinge-like deformation, they use the full nonlinear model to simulate its deformation at large strains, along with the incumbent twisted nematic block. Analogous experiments are also performed, confirming the simulation predictions, with the exception of a few non-idealities like hysteresis. Finally, a self-folding box is experimentally created using the optimized hinge textures, and while it still does not fold completely reliably, the authors claim that the problem is lessened as a result of the optimized texture. The approach described in this paper is very promising, but the model used is entirely material-agnostic in that it contains nothing specific to LCEs or even elastomers. It is unclear whether it would still be accurate in the case of external

applied forces, or geometries other than thin-film.

Mbanga *et al.* [40] simulate the dynamics of an LCE under strain using a nonlinear finite element model. They formulate a Hamiltonian with terms for the mechanical properties of an isotropic elastic solid, coupling between strain and nematic order, coupling between nematic order and the nematic order originally imprinted during cross-linking, and a term for nematic elasticity. This Hamiltonian is then adapted to a tetrahedral mesh in a finite element formulation. They simulate how the nematic order of an initially uniaxial nematic evolves when stress is applied perpendicular to the initial director. They observe a semi-soft elastic stress-strain curve, with an initially linear trend that plateaus over some span of strains before becoming linear again; within the plateau region, the director reorients to point along the direction of applied stress. In this configuration, there is a degeneracy in which way the director rotates, and it has been theoretically predicted (and experimentally confirmed) that the domain will be divided into alternating stripes where in half of the stripes, the director will rotate clockwise, and in the other half, the director will rotate counter-clockwise. The authors were able to successfully reproduce this phenomenon in their simulations and investigate the onset and shape in detail. Since their model also accounts for dynamics, they also measured the impact of strain rate on stress-strain curves, finding that faster strain rates increased the stress required to deform the sample. Although the work is impressive, the authors did not relate any of the model coefficients and parameters to those of real materials. Some of the model terms are familiar solid mechanics quantities, such as the bulk modulus, but others are more vaguely-defined coupling strengths and energy penalties; this raises some doubt about how this model might be applied to real LCE materials, which is not directly addressed in the paper.

In the work by Sawa *et al.* [32], a nonlinear continuum model is applied to bending LCE actuators with hybrid nematic texture. The deformation of a simple rectangular domain is simulated in response to changes in temperature. The key metric used to characterize deformation is curvature, since the expected deformation of a hybrid-aligned LCE is a uniform circular shape. Very good agreement is achieved between the simulations and a set of parallel experiments. Crucially, material parameters (which are few in number) are determined in an empirical and stimulus-independent manner, which allows the model to be adapted to new materials with a minimal amount of characterization. The model also accounts for the effects of deswelling, which may occur if unreacted material leftover during the synthesis of the LCE is expelled. Although the simplest model of rubber elasticity is used, co-authors DeSimone and Teresi derive how the model might be expanded in an earlier paper [45], showing the flexibility of the approach. Other applications of the model to twisting actuators [64] and crawlers [65] support the use of this model for relatively complex deformation modes. However, the model does not account for dynamics, which

would have clear utility for some applications. Additionally, the nematic texture is assumed to be uniaxial which excludes the modelling of textures with defects unless further simplifications are made. Finally, the authors do not consider the dynamic reorientation of the mesogens, assuming that the LC texture is "frozen-in" at the time of cross-linking; as a result, although the underlying neo-classical model can reproduce soft elasticity, the authors use a method of solution that ignores it.

With that being said, the core of the project requirements are satisfied by the model demonstrated in Sawa *et al.* [32], and it shows potential for extension if more advanced features are required. Thus, this model was selected for this research project.

3.3 Hyperelastic LCE Model

The LCE model developed by Sawa *et al.* [32] will be used in this work. The model is an adaptation of Bladon, Warner and Terentjev's so-called "trace formula" model, which will first be briefly described before moving on to the adaptation appearing in ref. 32.

3.3.1 Neo-classical Model

The neo-classical model for LCEs is a simple theoretical model developed by Bladon, Warner and Terentjev, based on the neo-Hookean model of rubber. It involves the assumption that polymer chains act as non-interacting random walks, and that their free energy is entirely entropic. Its full derivation is presented in ref. 2, Chapters 3 and 6, where the free energy density of a nematic rubber in Equation 6.5 of ref. 2 (also known as the "trace formula") is as follows (Dyadic/Gibbs tensor notation [66]):

$$W_{trace} = \frac{1}{2}\mu \,\mathrm{Tr}\left(\boldsymbol{L}_0 \cdot \boldsymbol{F}^T \cdot \boldsymbol{L}^{-1} \cdot \boldsymbol{F}\right) \tag{3.1}$$

where μ is the shear modulus, $\boldsymbol{F} = \boldsymbol{\delta} + \boldsymbol{\nabla u}$ is the deformation gradient, $\boldsymbol{u}$ is the displacement, and $\boldsymbol{L}$ is a tensor characterizing the shape anisotropy of the underlying polymer network, which is related to the direction and magnitude of nematic order. The subscript 0 indicates the quantity as it was at the time of cross-linking from a polymer melt into an elastomer. Qualitatively, the equation characterizes the energy density of an LCE that initially has polymer anisotropy $\boldsymbol{L}_0$, and is deformed by $\boldsymbol{F}$ so that the new polymer anisotropy is $\boldsymbol{L}$.

Although this model can reproduce soft elasticity [2], in which certain deformations have no energetic cost (see Section 2.2.3), real experimental samples invariably show some kind of threshold before the onset of soft elasticity, no matter how small [2, 36].

3.3.2 Anisotropic Extension to the Neo-classical Model

DeSimone and Teresi reconcile the immediate onset of soft elasticity in the trace formula with the threshold observed in experimental samples by showing that the trace formula actually describes an originally isotropic material which has been deformed uniaxially; the anisotropy at the time of cross-linking is shown to be irrelevant to the formula after a change-in-reference [45]:

$$W_{trace} = \frac{1}{2}\mu \,\mathrm{Tr}\left(\boldsymbol{B}\cdot\boldsymbol{L}^{-1}\right) \tag{3.2}$$

$\boldsymbol{B} = \boldsymbol{F}\cdot\boldsymbol{F}^T$ is the left Cauchy-Green strain tensor. Note that Equations 3.1 and 3.2 exist in different frames of reference. See ref. 45 for more details.

Since the left Cauchy-Green strain tensor is invariant under rotations of the material frame, it is physically appropriate for isotropic materials such as conventional rubbers. DeSimone and Teresi propose a correction term with a similar form in Equation 26 of ref. 45 but using the right Cauchy-Green strain tensor $\boldsymbol{C} = \boldsymbol{F}^T\cdot\boldsymbol{F}$:

$$W_{an} = \frac{1}{2}\mu_\beta \,\mathrm{Tr}\left(\boldsymbol{C}\cdot\boldsymbol{L}_0^{-1}\right) \tag{3.3}$$

They use a distinct shear modulus μ_β.

The right Cauchy-Green strain tensor is sensitive to rotations of the material frame, hence permanently encoding the anisotropy at the time of cross-linking. In turn, it is insensitive to rotations of the spatial frame, which is associated with the symmetry of space and physical laws.

Finally, in Sawa *et al.* [32], the model is reduced to only contain the anisotropic correction of Equation 3.3 and not the original trace formula. In this case, μ_β and $\boldsymbol{L}_0$ carry all the physical properties of the model, and they lose some of their original physical meaning as they absorb μ and compensate for the loss of the isotropic component.

The hyperelastic energy density in Sawa *et al.* [32] is:

$$W(\boldsymbol{C};\boldsymbol{C}_*) = \frac{1}{2}\mu(\boldsymbol{C}:\boldsymbol{C}_*^{-1} - 3) \tag{3.4}$$

where μ is the shear modulus, $\boldsymbol{C}$ is the right Cauchy-Green strain tensor characterizing the true deformation and $\boldsymbol{C}_*$ is the right Cauchy-Green strain tensor of an idealized deformation of the LCN in response to a given stimulus. This formulation is from Equation 9 of ref. 32.

Given the deformation gradient $\boldsymbol{F}$, the right Cauchy-Green strain tensor is defined as $\boldsymbol{C} = \boldsymbol{F}^T \cdot \boldsymbol{F}$. For the case of $\boldsymbol{C}_*$, the corresponding deformation gradient $\boldsymbol{F}_*$ is defined as follows:

$$\boldsymbol{F}_* = \lambda_\parallel \boldsymbol{n}\boldsymbol{n} + \lambda_\perp \left[\boldsymbol{\delta} - \boldsymbol{n}\boldsymbol{n}\right] \tag{3.5}$$

where λ represents a local stretch equal to ℓ/ℓ_0, the ratio of current and initial length. Equivalently, if ϵ is defined as strain, $\lambda = 1 + \epsilon$. The local stretch factors $\lambda_\parallel$ and $\lambda_\perp$ lie parallel and perpendicular, respectively, to the nematic director, $\boldsymbol{n}$, which is a function of position. Note that $\boldsymbol{F}_*$ takes the place of $\boldsymbol{L}$ and $\boldsymbol{L}_0$ in ref. 45, as director reorientation is assumed to be negligible. These are empirical quantities that are used in lieu of direct information about the amount of LC order, its coupling to mechanical deformation, and its response to stimuli.

It can be seen that Equation 3.4 has a minimum for the case $\boldsymbol{C} = \boldsymbol{C}_*$. This corresponds to a deformation gradient $\boldsymbol{F} = \boldsymbol{F}_*$. As an example, consider the case where $\boldsymbol{n} = \boldsymbol{e}_3$:

$$\boldsymbol{F}_*(\boldsymbol{n} = \boldsymbol{e}_3) = \begin{bmatrix} \lambda_\perp & 0 & 0 \\ 0 & \lambda_\perp & 0 \\ 0 & 0 & \lambda_\parallel \end{bmatrix} \tag{3.6}$$

This deformation gradient corresponds to a stretch of $\lambda_\parallel$ and $\lambda_\perp$ along the appropriate axes. One solution for the corresponding displacement field would be:

$$\boldsymbol{u}_*(\boldsymbol{n} = \boldsymbol{e}_3) = \begin{bmatrix} (\lambda_\perp - 1)X_1 \\ (\lambda_\perp - 1)X_2 \\ (\lambda_\parallel - 1)X_3 \end{bmatrix} = \begin{bmatrix} \epsilon_\perp X_1 \\ \epsilon_\perp X_2 \\ \epsilon_\parallel X_3 \end{bmatrix} \tag{3.7}$$

The neglect of director reorientation when solving the model means that semi-soft elasticity will never be exhibited by the model as solved by the methods in this thesis. Although semi-soft elasticity is an intriguing property of LCEs, adding director reorientation would complicate the solution of the model and thus it is not considered at this time. This raises a question of the accuracy and applicability of the model. It is known that for LCEs cross-linked in the nematic state, soft elasticity is not observed until some threshold stress or deformation (i.e., semi-soft elasticity) [2, 36]. In ref. 45, where the model originates, the authors derive the theoretical bounds for the values of $\lambda_\parallel$ where a "hard" or typical elastic response may be observed. They come up with the following expression:

$$\lambda_\parallel \in [a^{-1/6}, a^{1/12}) \tag{3.8}$$

where a is a ratio representing the backbone anisotropy of the polymer chain [2, 45]; it is equal to $\lambda_{\parallel}^{1/3}$ when the reference state is fully isotropic and the current state is fully nematic (i.e., the maximum range of deformation of the LCE). Using an example value $a = 2$, suggested by the authors as large but realistic, results in a set of bounds $\lambda_{\parallel} \in [0.891, 1.059)$. This corresponds to strains on the order of a few percent, which are considered large outside of the field of LCEs. Clearly, it would be desirable to add director reorientation to the model. In the meantime, however, the impact on the accuracy of the results should be minimal for values of $\lambda_{\parallel}$ within the defined bounds, as well as cases where there are no forces applied at a near-perpendicular angle to $\boldsymbol{n}$.

As LCEs are typically assumed to be incompressible [2], an incompressibility constraint was added to the model. First, the expression for potential energy density was modified to be invariant with respect to isotropic expansion or contraction [67] (signified with a $\hat{}$ symbol):

$$\hat{W}(\boldsymbol{C}) = W(\hat{\boldsymbol{C}}) \tag{3.9}$$

$$= W((\det \boldsymbol{F})^{-2/3}\boldsymbol{C}) \tag{3.10}$$

Then, an isotropic stress term was added along with a corresponding equation to enforce incompressibility:

$$W = \hat{W} + p(\det \boldsymbol{F} - 1) \tag{3.11}$$

$$\det \boldsymbol{F} = V/V_0 = 1 \tag{3.12}$$

This is the nonlinear incompressibility criterion (see, e.g., Chapter 3 in ref. 56). Note the more typical $\boldsymbol{\nabla} \cdot \boldsymbol{u} = 0$ is only valid for small deformations (linear regime), and cannot be used here. p is a scalar field that acts as a Lagrange multiplier.

An interesting consequence of the model is that if there are no external forces, and if the shear modulus is spatially homogeneous, its value has no influence on the solution, since it is just a scalar multiple of the energy density. Thus, the deformation mode can be predicted without knowledge of this parameter.

The potential energy density was used to derive an expression for the Cauchy stress tensor $\boldsymbol{\sigma}$ [67]:

$$\boldsymbol{\sigma} = \frac{1}{\det \boldsymbol{F}} \frac{\partial W}{\partial \boldsymbol{F}} \cdot \boldsymbol{F}^T \tag{3.13}$$

Following the decomposition of W, the Cauchy stress tensor is also decomposed into devi-

atoric and isotropic parts in the incompressible formulation:

$$\boldsymbol{\sigma}_{dev} = \frac{1}{\det \boldsymbol{F}} \frac{\partial \hat{W}}{\partial \boldsymbol{F}} \cdot \boldsymbol{F} = \mu \left(\det \boldsymbol{F}\right)^{-5/3} \left[\boldsymbol{F} \cdot \boldsymbol{C}_*^{-1} \cdot \boldsymbol{F}^T - \frac{1}{3} \boldsymbol{C} : \boldsymbol{C}_*^{-1} \, \boldsymbol{\delta} \right] \tag{3.14}$$

$$\boldsymbol{\sigma}_{iso} = \frac{1}{\det \boldsymbol{F}} \frac{\partial}{\partial \boldsymbol{F}} \left[p(\det \boldsymbol{F} - 1) \right] \cdot \boldsymbol{F} = p\boldsymbol{\delta} \tag{3.15}$$

$$\boldsymbol{\sigma} = \boldsymbol{\sigma}_{dev} + \boldsymbol{\sigma}_{iso} \tag{3.16}$$

A full derivation is shown in Appendix A.

The presence of the determinant makes the resulting expression for $\boldsymbol{\sigma}$ nonlinear in the deformation of the material. Since the constitutive equation (Equation (3.4)) is both nonlinear and path-independent in terms of the state of deformation, the model is *hyperelastic* by definition [67].

This expression for $\boldsymbol{\sigma}$ is then substituted into Equation 3.17 to solve the model:

$$\rho \boldsymbol{a} = \boldsymbol{\nabla} \cdot \boldsymbol{\sigma} + \boldsymbol{B} \tag{3.17}$$

Here ρ is the mass of one infinitesimal volume of the continuum, $\boldsymbol{a} = \frac{\partial^2 \boldsymbol{u}}{\partial t^2}$ is its acceleration, $\boldsymbol{\sigma}$ is the Cauchy stress tensor that it is subject to, and $\boldsymbol{B}$ is the external force acting on that volume.

This equation defines the conservation of momentum for a continuum, and by substituting Equation 3.16 into it, it is ensured that solutions have no discontinuities (i.e., voids or overlapping of different parts of the domain).

The solution method is described in the following section.

3.4 Finite Element Description

The Galerkin finite element method is a numerical method for solving boundary value problems for systems of partial differential equations (PDEs). The domain of the PDE is discretized into a mesh of interconnected points, which need not fall on a regularly-spaced lattice. The Galerkin method of weighted residuals is used to map the original (continuous) model equations onto the discretized mesh, and to subsequently formulate an expression for the residual of a proposed solution (or "trial function") [68]. Solutions found using the finite element method minimize this residual over the domain.

In order to use the method of weighted residuals, the model equations must be put into "weak" or variational form given some arbitrary test function. In the finite element method, a set of test functions is used to weight the residual locally in each mesh element; in the converged solution, the residual will be minimized for all test functions in the set. The following procedure follows the steps and techniques shown in Chapter 2 of ref. 68.

We start with Cauchy's momentum equation, as written in Equation 3.17. To put it into weak form, the first step is to move all the terms to one side, then take the inner product with a test function over the domain. The test function has the same dimensionality as the unknown that we are solving for; in our case, the unknown is a displacement vector $\boldsymbol{u}$, which is implicitly included in Equation 3.17 via $\boldsymbol{a}$ and $\boldsymbol{\sigma}$ (as defined in Equation 3.16). So our test function will be a vector, called $\boldsymbol{v}$.

The weak form can now be written:

$$\int_\Omega \rho \boldsymbol{a} \cdot \boldsymbol{v} \, \mathrm{d}V - \int_\Omega (\boldsymbol{\nabla} \cdot \boldsymbol{\sigma}) \cdot \boldsymbol{v} \, \mathrm{d}V - \int_\Omega \boldsymbol{B} \cdot \boldsymbol{v} \, \mathrm{d}V = 0 \tag{3.18}$$

where Ω specifies the volume of the domain.

This identity holds for any rank 2 tensor $\boldsymbol{\sigma}$ and vector $\boldsymbol{v}$ [68]:

$$\boldsymbol{\nabla} \cdot (\boldsymbol{\sigma} \cdot \boldsymbol{v}) = \left(\boldsymbol{\nabla} \cdot \boldsymbol{\sigma}^T\right) \cdot \boldsymbol{v} + \boldsymbol{\sigma} : (\boldsymbol{\nabla} \boldsymbol{v})^T \tag{3.19}$$

The Cauchy stress tensor is symmetric, so we can safely eliminate the transposes:

$$\boldsymbol{\nabla} \cdot (\boldsymbol{\sigma} \cdot \boldsymbol{v}) = (\boldsymbol{\nabla} \cdot \boldsymbol{\sigma}) \cdot \boldsymbol{v} + \boldsymbol{\sigma} : (\boldsymbol{\nabla} \boldsymbol{v}) \tag{3.20}$$

Consider the divergence theorem [68]:

$$\int_\Omega \boldsymbol{\nabla} \cdot \boldsymbol{X} \, \mathrm{d}V = \int_{\partial\Omega} \boldsymbol{X} \cdot \hat{\boldsymbol{k}} \, \mathrm{d}S \tag{3.21}$$

where $\partial\Omega$ specifies the boundary of the domain, and $\hat{\boldsymbol{k}}$ is the surface normal vector.

If we integrate Equation 3.20, we can use the divergence theorem to simplify the left-hand side:

$$\int_\Omega \boldsymbol{\nabla} \cdot (\boldsymbol{\sigma} \cdot \boldsymbol{v}) \, \mathrm{d}V = \int_{\partial\Omega} (\boldsymbol{\sigma} \cdot \boldsymbol{v}) \cdot \hat{\boldsymbol{k}} \, \mathrm{d}S \tag{3.22}$$

$$= \int_\Omega (\boldsymbol{\nabla} \cdot \boldsymbol{\sigma}) \cdot \boldsymbol{v} \, \mathrm{d}V + \int_\Omega \boldsymbol{\sigma} : (\boldsymbol{\nabla} \boldsymbol{v}) \, \mathrm{d}V \tag{3.23}$$

Now we can rearrange and substitute that into Equation 3.18:

$$-\int_\Omega (\boldsymbol{\nabla}\cdot\boldsymbol{\sigma})\cdot\boldsymbol{v}\,\mathrm{d}V = \int_\Omega \boldsymbol{\sigma} : (\boldsymbol{\nabla}\boldsymbol{v})\,\mathrm{d}V - \int_{\partial\Omega} (\boldsymbol{\sigma}\cdot\boldsymbol{v})\cdot\hat{\boldsymbol{k}}\,\mathrm{d}S \tag{3.24}$$

$$\int_\Omega \rho\boldsymbol{a}\cdot\boldsymbol{v}\,\mathrm{d}V + \int_\Omega \boldsymbol{\sigma} : (\boldsymbol{\nabla}\boldsymbol{v})\,\mathrm{d}V - \int_{\partial\Omega} (\boldsymbol{\sigma}\cdot\boldsymbol{v})\cdot\hat{\boldsymbol{k}}\,\mathrm{d}S - \int_\Omega \boldsymbol{B}\cdot\boldsymbol{v}\,\mathrm{d}V = 0 \tag{3.25}$$

Now, in the case of static equilibrium, we can set $\boldsymbol{a} = \boldsymbol{0}$. Due to symmetry, we can rearrange $(\boldsymbol{\sigma}\cdot\boldsymbol{v})\cdot\hat{\boldsymbol{k}} = \left(\boldsymbol{\sigma}\cdot\hat{\boldsymbol{k}}\right)\cdot\boldsymbol{v}$. The surface traction $\boldsymbol{\sigma}\cdot\hat{\boldsymbol{k}}$ should equal zero in static equilibrium, but we may want to specify a Neumann boundary condition to subject the domain to some external traction.

In that case, we can specify some surface traction $\boldsymbol{h}$ which is applied to some subset of the boundary Γ_N. For further simplification, we can neglect gravity and other external forces, setting $\boldsymbol{B} = \boldsymbol{0}$. This is a reasonable assumption for stiff LCNs with small dimensions; later experiments performed with millimeter-scale LCNs do not reveal substantial bending under gravity. The simplifications result in the final weak form of Cauchy's momentum equation:

$$\int_\Omega \boldsymbol{\sigma} : (\boldsymbol{\nabla}\boldsymbol{v})\,\mathrm{d}V - \int_{\Gamma_N} \boldsymbol{h}\cdot\boldsymbol{v}\,\mathrm{d}S = 0 \tag{3.26}$$

Based on the form of $\boldsymbol{\sigma}$ used, this equation has no dependence on bare $\boldsymbol{u}$ terms, only on gradients of it. Therefore there are an infinite number of solutions trivially related by a constant shift in $\boldsymbol{u}$ across the domain (corresponding to a rigid body translation of the domain). To ensure convergence to a single well-defined solution, it is necessary to specify a Dirichlet boundary condition fixing the value of $\boldsymbol{u}$ in some part of the domain. Besides $\boldsymbol{u}$, there is one more unknown quantity: the scalar field p (which appears implicitly in $\boldsymbol{\sigma}$), which enforces incompressibility. This necessitates one more equation in the finite element formulation with its corresponding set of (scalar) test functions q, which also needs its own weak form.

The strong form comes from Equation 3.12. p is well-specified by the constraint in Equation 3.12, so the weak form can be written in a straightforward manner:

$$q\,(\det\boldsymbol{F} - 1) = 0 \tag{3.27}$$

where q is the corresponding test function for the unknown p. Equations 3.26 and 3.27 together comprise the finite element formulation of nonlinear, static and incompressible elasticity problems.

By substituting the model's formulation for $\boldsymbol{\sigma}$ from Equation 3.16, the model can be solved. Since the model is nonlinear, Newton's method is used to solve the system of

equations resulting from the finite element description of the problem. The model is implemented and solved using version `2016.1.0` of `FEniCS`, an open-source software package which implements the finite element method along with related numerical methods. The basis functions used in the finite element formulation are Lagrange interpolating polynomials, with continuity enforced at element boundaries. Displacement uses second-order interpolants, and pressure uses first-order interpolants, a formulation that is known as Taylor-Hood, which is known to improve the numerical stability of incompressible elasticity problems. Tetrahedral elements are used, since they allow for the meshing of complex geometries and remain the only well-supported three-dimensional element in `FEniCS` at the time of writing.

To run a deformation simulation, the magnitude of mesogen order is changed (corresponding to a change in temperature or an applied field, as empirically measured), and the corresponding deformation response of the domain is measured. The mesogen order is specified by the pair of scalars $(\lambda_{\parallel}, \lambda_{\perp})$, as defined in Section 3.3.2. Since the LCE domain is assumed to be incompressible, only one needs to be specified (see Equation 4.1). If temperature is used as the stimulus, an increased temperature leads to a decreased value of $\lambda_{\parallel}$. It is assumed that $\lambda_{\parallel}$ is uniform throughout the domain.

In the initial state, $\lambda_{\parallel} = 1$ and $\boldsymbol{u} = \mathbf{0}$, corresponding to an undeformed domain. Using a continuation method $\lambda_{\parallel}$ is gradually moved closer to some target value in a series of steps. The step size is automatically adjusted so that steps are as large as possible while retaining numerical convergence. For the total residual of the domain, an absolute tolerance of 1.0×10^{-11}, and a relative tolerance of 1.0×10^{-9} were used. When the simulation is completed, a series of datapoints containing the state of deformation for different stimuli has been collected. In this simple scheme where the magnitude of the stimulus is increased at each step, this results in a discrete set of data for the deformation as a function of the magnitude of the stimulus.

Chapter 4

LC Mechanical Model Validation

4.1 Material

Although other forms of validation are included in this chapter, the most important checks were made by comparing simulations to experimental data from several formulations of the LCE given in ref. 1. All experimental data was provided by Hamed Shahsavan.

Each formulation is composed of a mixture of 4-(6-Acryloxy-hex-1-yl-oxy)phenyl 4-(hexyloxy)benzoate and 1,4-Bis[4-(6-acryloyloxyhexyloxy)benzoyloxy]-2-methylbenzene, hereafter referred to as M1 and M2, respectively. Each compound is a monomer, but M1 is bi-functional, while M2 is tri-functional, meaning that the amount of M2 is primarily responsible for the amount of cross-linking in the network. Compositions are referred to by the weight percentage of M2 in relation to the total weight of M1 and M2. Experimental data for the basic temperature response (see Section 4.2) is available for the formulations with 12%, 25%, 50% and 75% M2 composition. However, data used for subsequent verification (see Section 4.4 and 4.5) was only available for samples with 12% and 50% M2. These materials are hereafter referred to simply by their M2 composition and anchoring conditions.

4.2 Measurement of the Idealized Deformation

In the model, the term $\boldsymbol{C}_* = \boldsymbol{F}_*^T \cdot \boldsymbol{F}_*$ represents the idealized response of the LCE to the given stimulus. It is defined in terms of an idealized deformation gradient $\boldsymbol{F}_*$, which is in turn defined in terms of the director $\boldsymbol{n}$ and local stretch factors $\lambda_\parallel$ and $\lambda_\perp$ in Equation 3.5.

The local stretch factors are measured using experimental data, in which a sample with a uniform director is made and its shape change in response to the stimulus is measured. More precisely, thin film samples were created with either planar-uniaxial (in-plane) or homeotropic (out-of-plane) anchoring. Then, each sample was placed on a temperature-controlled microscope stage, and images were successively captured as the temperature was raised. Using custom-made image processing software described in Appendix B with manual measurement as necessary, the in-plane dimensions of each sample were measured in each image. $\lambda(T)$ is then calculated along axes parallel and perpendicular to the director. $\lambda = \ell/\ell_0$, where the ℓ_0 is the reference length, which is simply taken to be the length along the appropriate axis at the starting temperature. Data was collected experimentally using the above procedure for all formulations of LCE.

In the case of the homeotropically-aligned samples, the two visible axes of the film (i.e., the in-plane axes) are perpendicular to the director, which is pointed in the out-of-plane direction. Thus, only $\lambda_\perp(T)$ can be measured from these images. In the data collected, neither axis appeared to change much with temperature; although this runs counter to expectations, the homeotropic samples are not directly used in the rest of the analysis.

In the case of the planar-aligned samples, both $\lambda_\parallel(T)$ and $\lambda_\perp(T)$ can be measured simultaneously, with the assumption that there is no difference between $\lambda_\perp(T)$ in the in-plane and out-of-plane direction. This is a substantial assumption, as the in-plane and out-of-plane directions are different in *space* due to gravity and the normal force of the stage, even if they should be equivalent in the material. Sample output of the image processing methods are shown in Figures 4.1a–4.1b.

Figure 4.2 shows the stretch factors versus temperature measured directly from experimental data for the planar samples with 50% M2 composition. Additionally, the temperature dependence of $\lambda_\perp(T)$ was also computed indirectly from the experimentally determined values of $\lambda_\parallel(T)$ given an assumption of incompressibility (Equation 4.1),

$$\hat{\lambda}_\parallel \hat{\lambda}_\perp^2 = 1 \tag{4.1}$$

where the $\hat{}$ symbol is used to denote quantities which obey the incompressibility constraint. While LCEs are theoretically incompressible [2], experimental results clearly show (Figure 4.2) that the samples exhibited non-negligible change in volume. Thus the use of the model without corrections for isotropic thermal expansion/contraction will introduce inaccuracy into simulation results. Using an *a priori* assumption, the experimentally-observed temperature response of the film was decomposed into an isotropic component, representing thermally-induced volume change, and an incompressible anisotropic component, representing the theoretical response of the LCN to temperature:

$$\lambda_\parallel \lambda_\perp^2 = (\hat{\lambda}_\parallel \lambda_{th})(\hat{\lambda}_\perp \lambda_{th})^2 = \lambda_{th}^3 = V/V_0 \tag{4.2}$$

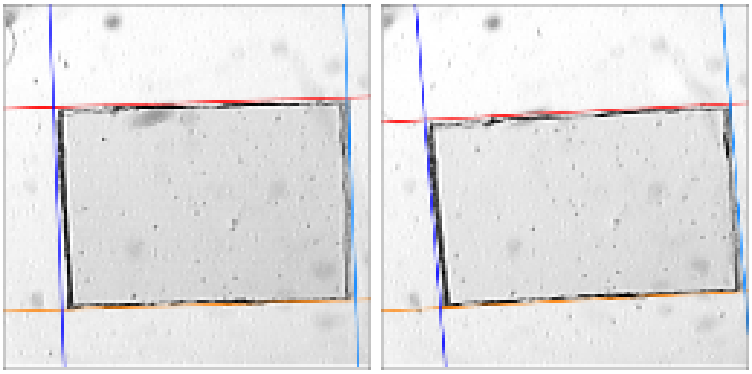

(a) (b)

Figure 4.1: Sample image processing output of uniform planar-aligned LCN films with 50% M2 composition for (a) $T = 32.1°C$ and (b) $T = 179.6°C$. The film shape identified by the image processing method, indicated by coloured lines, was used to compute $\lambda_{\parallel}$ (in the vertical axis) and $\lambda_{\perp}$ (in the horizontal axis) for each sample over a range of temperatures in order to construct an empirical relation between temperature T and deformation of the LCN, i.e., $\lambda_{\perp}(T)$ and $\lambda_{\parallel}(T)$.

where λ_{th} is the isotropic stretch factor.

Isotropic expansion/contraction will cause an isomorphic volume change, preserving shape while the volume increases/decreases. Thus, if the decomposition is valid, the simulated deformation of the LCN will match the incompressible component of the experimentally-observed deformation. Since the thermally-induced volume change preserves shape, shape-based metrics such as curvature will remain unchanged between simulation and experiment. Furthermore, the value of λ_{th} is also experimentally measured, and thus states of deformation can be mapped between incompressible and experimental regimes.

This mapping between an experimental temperature and a set of incompressible stretches $\hat{\lambda}$ is achieved using two polynomial fits. If mapping from temperature to $\hat{\lambda}$, the first step is to fit $\lambda_{\parallel}(T)$. The inverse function $T(\lambda_{\parallel})$ is also fit for the case of the inverse mapping. An example of this process is shown in Figure 4.3.

In some samples, the datapoints around the lowest and highest temperatures show the response levelling off, giving the curve a nonlinear shape; this means the quality of fit is poor around the lowest and highest temperatures, and necessitates the use of a high order polynomial to get a satisfactory fit. As a result, the fit is only applied to values that fall within an interior span of the data; specified in temperature, this span goes between 5% and 95% of the full span of the data.

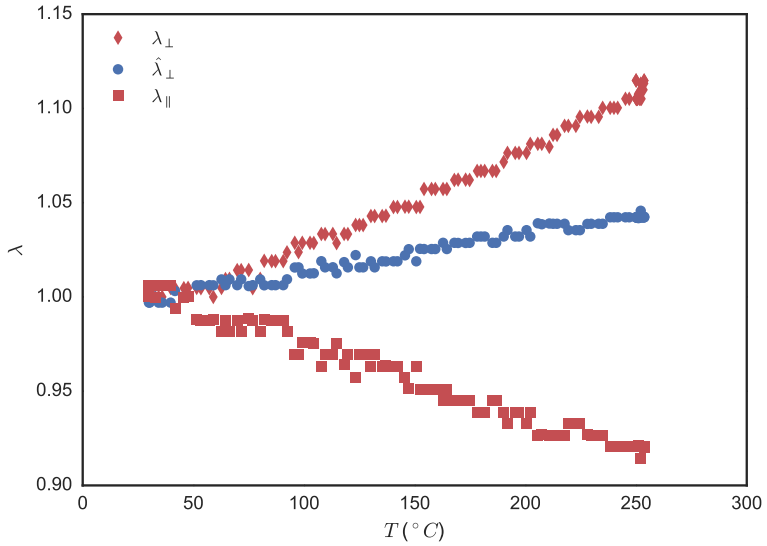

Figure 4.2: Image processing output of $\lambda_{\parallel}(T)$ (squares) and $\lambda_{\perp}(T)$ (diamonds) measured directly from experimental sample with 50% M2 composition and $\hat{\lambda}_{\perp}(T)$ (circles) measured indirectly using the incompressibility constraint.

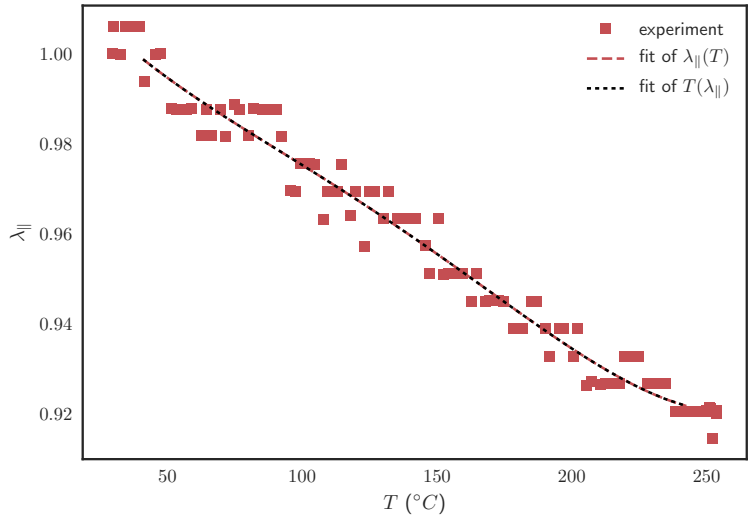

Figure 4.3: Fourth-order polynomial fits mapping $\lambda_{\parallel}$ and T for sample with 50% M2 composition.

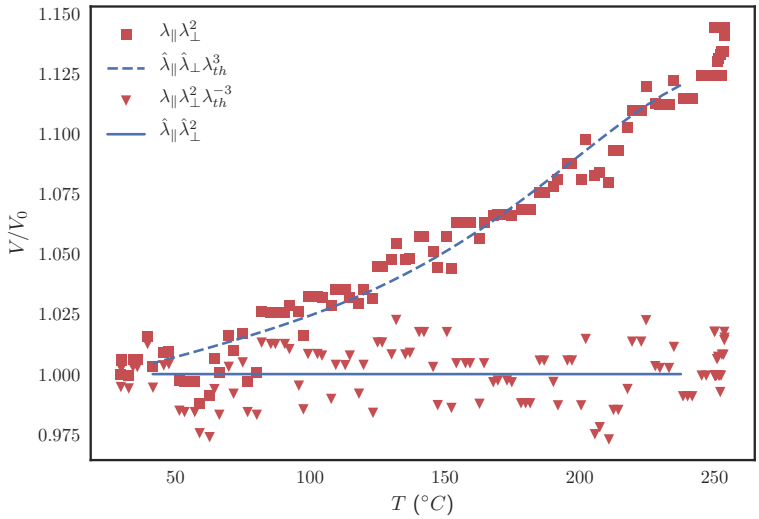

Figure 4.4: Plot of relative volume versus temperature, measured directly from experimental sample (squares) with 50% M2 composition, and mapped onto the incompressible regime (triangles) using the experimentally determined value of $\lambda_{th}(T)$. The inverse process, taking a range of incompressible pairs of λ (solid line) and mapping it onto the compressible regime (dashed line), is also plotted.

The next step is to fit $\lambda_{th}(\lambda_\parallel)$, and apply Equation 4.2 to find $\hat{\lambda}_\parallel$ and $\hat{\lambda}_\perp$. The function $\lambda_{th}(\hat{\lambda}_\parallel)$ is also fit for the case of the inverse mapping. The two fits can be combined in sequence to yield a mapping between experimental temperature and incompressible values for $\hat{\lambda}$ used in the simulation, demonstrated in Figure 4.4.

Plots demonstrating the temperature model and thermal expansion model determined from samples with 12% M2 composition are shown in Figures 4.5 and 4.6. Visual contrast in images of this sample was very low, so the image processing methods could not be used, necessitating manual measurement of the sample dimensions.

Consequently, all simulations are performed with the assumption of incompressibility and results are compared with experiment by mapping their stretch values based on the volume change observed. This approach comes with the significant advantage that the simulations are in some sense independent of the material used; they can be performed before the LCE material is known, or even be used to guide the selection of the material.

In the future, several steps could be taken to improve this mapping process. First, a

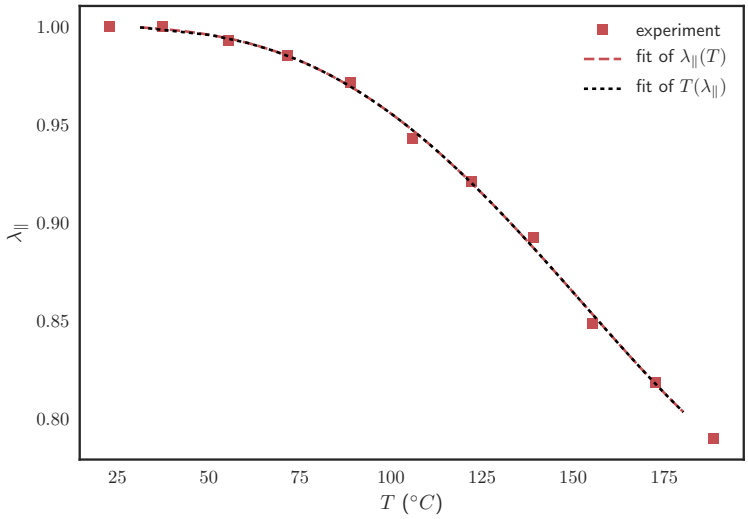

Figure 4.5: Fourth-order polynomial fits mapping $\lambda_{\parallel}$ and T for sample with 12% M2 composition.

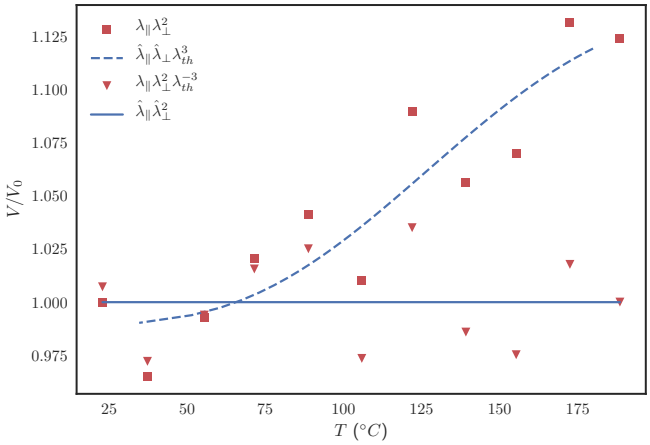

Figure 4.6: Plot of relative volume versus temperature, measured directly from experimental sample (squares) with 12% M2 composition, and mapped onto the incompressible regime (triangles) using the experimentally determined value of $\lambda_{th}(T)$. The inverse process, taking a range of incompressible pairs of λ (solid line) and mapping it onto the compressible regime (dashed line), is also plotted.

wider span of temperatures could be collected to get a fuller description of the material. The behaviour seen in the fits should only persist for a finite range, between the freezing or glass transition temperature and the nematic-isotropic transition temperature of the LCE, as plateaus are expected on either side of the data. More and higher-quality data would also be valuable; to this end, larger samples and higher resolution images with better colour contrast would make for less noisy data.

Next, instead of a two-step mapping process, it could be made one-step by simply making fits between temperature and λ_{th}, as the intermediary $\lambda_{\parallel}$ is unnecessary. This would reduce error introduced through the use of fitting. The current process is two-step simply because it was organically developed as the need arose, and it works adequately with the current data. Finally, rather than using high-order polynomials in linear regression, fits could be performed using locally-weighted linear regression. This would allow low-order polynomials to be used, yet easily capture bends and plateaus as they may occur, and unlike interpolation, it would be tolerant to noise and error in the data.

4.3 Hybrid Texture

A key texture used for validation is the hybrid texture, which employs planar anchoring of the director (tangent to the surface) on one bounding surface, and homeotropic anchoring (normal to the surface) on the other. Throughout the depth, there is a uniform change of the orientation between these two boundary conditions [69]. An analytical form for the director in a hybrid texture can be written as follows,

$$\boldsymbol{n}(\boldsymbol{x}) = \cos\left(\frac{\pi}{2t}x_3\right)\boldsymbol{e}_1 + \sin\left(\frac{\pi}{2t}x_3\right)\boldsymbol{e}_3 \tag{4.3}$$

where t is the thickness of the sample in x_3 and $\{\boldsymbol{e}_i\}$ are basis vectors for a Cartesian coordinate system with $\boldsymbol{e}_3$ orthogonal to the film. A schematic of this texture is shown in Figure 4.7. LCEs with this texture exhibit a pure bending deformation in response to temperature [32], which is an interesting but simple and easily characterizable change in shape.

4.4 Deformation of Cantilevers with Hybrid Texture

Several simulations were performed to check the stability and reproducibility of the results. Then, simulations measuring the curvature response of LCN cantilevers were performed and results were compared with analogous experiments from ref. 1.

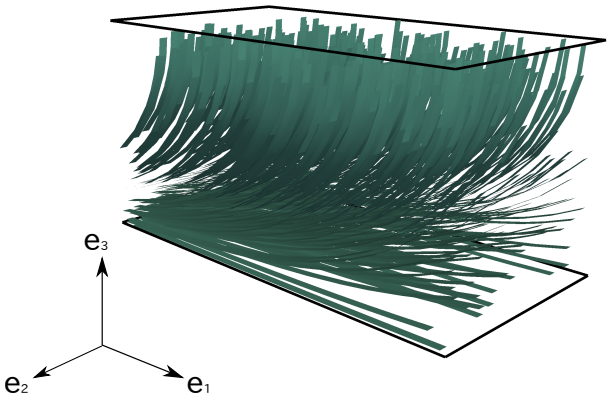

Figure 4.7: Schematic of the orientational alignment of a hybrid-aligned LCN film where the nematic director field $\boldsymbol{n}(\boldsymbol{x})$ is defined as the unit tangent to each plane throughout the film.

4.4.1 Characterization of deformation

The primary metric used to characterize this shape change is the curvature $\kappa = 1/r$, as homogeneous bending throughout a rectangular domain results in the shape of a circular arc. To measure curvature in simulation in a given state of deformation, all the coordinates of each mesh vertex are computed $\boldsymbol{x} = \boldsymbol{X} + \boldsymbol{u}$, and then fed into a nonlinear least-squares optimization process to find the radius of curvature. Briefly, this optimization seeks to find the location of a point that is equidistant from all mesh points as follows:

$$\underset{\boldsymbol{x}_c}{\text{argmin}} \ \text{Variance}\left[\boldsymbol{R}\right] \tag{4.4}$$

$$\text{where } R_i = \|\boldsymbol{x}_i - \boldsymbol{x}_c\| \tag{4.5}$$

This corresponds to the centre point of a circle where all the mesh coordinates lie along an arc on its circumference, and whose radius (taken to be the average of $\boldsymbol{R}$) is the radius of curvature. Since all simulations of the hybrid cantilever are arranged so that it bends about the $\boldsymbol{e}_2$ direction as an axis, this coordinate is ignored during this process.

A consequence of using all the points from the mesh is that the arc has some thickness, meaning that it is impossible to find a value of $\boldsymbol{x}_c$ such that the cost function becomes zero. It also introduces some error into the estimate of the radius, since mesh vertices might not be evenly distributed throughout the thickness of the domain, meaning that some parts of the domain have more weight in the optimization process than others.

Table 4.1: Simulation parameters for characterizing curvature metric

Parameter	**Value**
Type	Deformation
$\hat{\lambda}_{\parallel}$	$1.0 \rightarrow 0.975$
Init. step size	0.00025
Mesh shape	Rectangular
Texture	Hybrid
BCs	$\boldsymbol{u}(X_1 = X_{1_0}) = (0, 0, 0)$
Mesh dims.	3mm $\times$ 0.5mm $\times$ 0.188mm
Mesh density	5 elements / thickness
Shear modulus	1.0Pa

To quantify this error, the deformation of a hybrid-aligned cantilever was simulated, and the curvature was measured at $\hat{\lambda}_{\parallel} = 0.975$, serving as a reference. The reference had a aspect ratio of $\ell/t \approx 15.957$. Then, the curvature measurement was taken again using a subset of the mesh vertices belonging to a shorter cantilever—that is, for some desired length ℓ, only mesh points originally located at some $X_1 < \ell$ were included. Such measurements were taken for 100 subsets of the full data, with evenly-spaced aspect ratios ranging from 1 to ≈ 15.957. Simulation parameters are listed in Table 4.1. An image showing the mesh points used in several example subsets is shown in Figure 4.8.

The relative error was calculated for each subset, and plotted in Figure 4.9. As can be seen, error is very large until a threshold aspect ratio where it drastically falls, and continues to decrease as aspect ratio increases.

For curvature measurements, care is made to always use samples of aspect ratio 8 or more, to ensure that the estimate is converged to a reasonably accurate value. In the future, this measurement could be improved by only sampling coordinates that originally lay on the mid-plane in $\boldsymbol{e}_3$ in the undeformed domain.

4.4.2 Mesh Independence

To show the numerical convergence of the simulations, their sensitivity to mesh density was briefly investigated. `FEniCS` has limited support for refining and coarsening the mesh during simulation, so as an alternative, several simulation runs were made using identical parameters except for the mesh density. All simulations used hybrid texture, and $\hat{\lambda}_{\parallel}$ was swept from 1 to 0.99. Integer numbers of elements per the thickness of the domain were

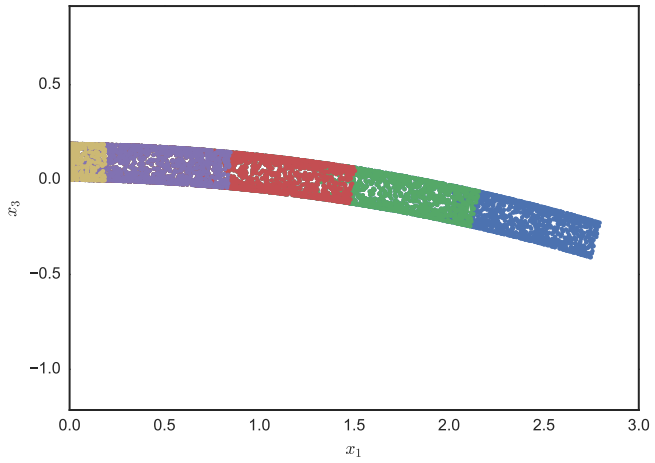

Figure 4.8: Sampled mesh vertices from various subsets of the full cantilever. Note that subsets are inclusive, that is, the yellow set is a subset of the purple set, which in turn is a subset of the red set, etc.

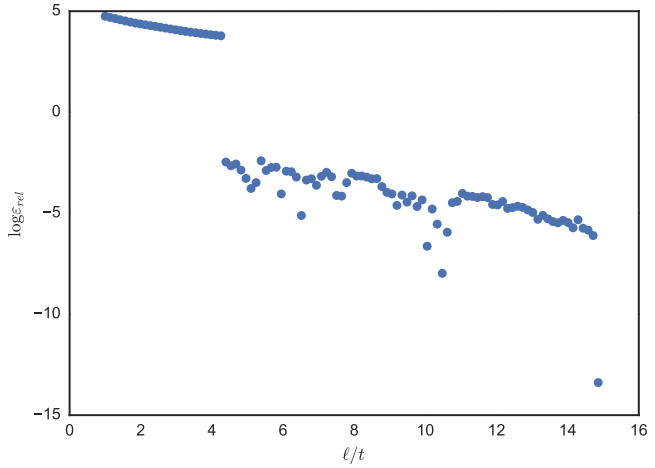

Figure 4.9: Relative error of curvature estimate as a function of cantilever aspect ratio. Note the logarithmic y-axis.

Table 4.2: Simulation parameters for characterizing mesh independence of model

Parameter	**Value**
Type	Deformation
$\hat{\lambda}_{\parallel}$	$1.0 \rightarrow 0.99$
Init. step size	0.00025
Mesh shape	Rectangular
Texture	Hybrid
BCs	$\boldsymbol{u}(X_1 = X_{1_0}) = (0, 0, 0)$
Mesh dims.	3mm $\times$ 0.5mm $\times$ 0.188mm
Mesh density	1–5 elements / thickness
Shear modulus	1.0Pa

chosen as mesh densities of interest, since the thickness defines the most important length scale for the hybrid texture. Densities of 1, 2, 3, 4, and 5 elements per unit of thickness were selected. Other parameters are listed in Table 4.2.

To compare the results, the positions of the corners at the free tip of the cantilever were observed at each step of the simulation. The simulation with the highest mesh density was used as a reference, and error was computed between it and the other simulations, using the Euclidean distance between matching pairs of corners. The final error values are averaged over the different corners. The results can be seen in Figure 4.10.

The amount of error decreases monotonically as the mesh density increases. The lowest mesh density tested showed substantially larger error than all other simulations. All simulations showed a linear relationship between $\hat{\lambda}_{\parallel}$ and error. After fitting first-order polynomials $\varepsilon_{abs}(\hat{\lambda}_{\parallel})$ to all simulations shown in Figure 4.10, the resulting coefficient of determination (R^2) was larger than 0.999 for every simulation.

Since the error is measured at the free end of a bending cantilever, the length of the cantilever, 3mm, defines the scale of the deformations. From this perspective, the magnitude of error is small in all the simulations. Thus, even a mesh density of 2 tetrahedrons spanning the thickness of the domain is roughly adequate for simulating and characterizing bending deformations.

4.4.3 Step Size Independence

The step size taken is of also of interest when considering numerical convergence. The numerical method requires an initial guess for the results, and the solution of the previous

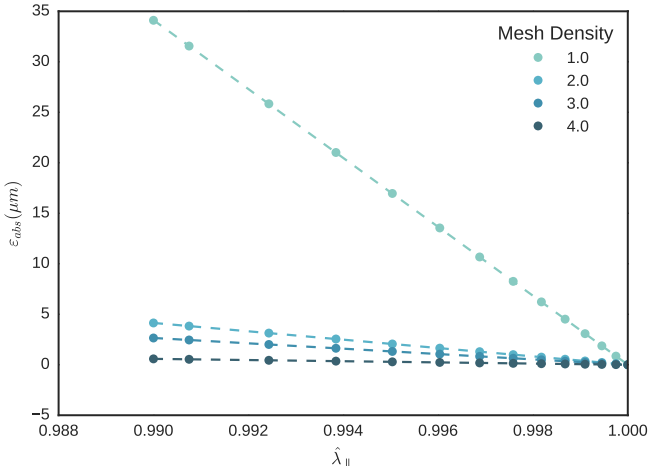

Figure 4.10: Absolute error of position of cantilever tip for simulations of varying mesh densities. Density is expressed in units of numbers of elements per unit thickness of the domain.

step is supplied; thus, a larger step size implies that the initial guess is further from the true solution. In a linear system, such details do not impact the solution, but since the model is nonlinear, it is possible that larger steps could result in failure to converge, or convergence to a distinct solution. Here, several simulations are run with identical parameters except for the initial step size. Contrary to typical simulations, the step size is not changed throughout the simulation.

The simulations used the hybrid texture and $\hat{\lambda}_{\parallel}$ was swept from 1 to 0.98. 5 different step sizes were chosen so that the goal would be reached in 2, 4, 6, 8, or 10 steps, respectively. Other parameters are listed in Table 4.3.

To compare the results, the positions of the corners at the free tip of the cantilever were observed at each step of the simulation, as described in Section 4.4.2. The simulation with the smallest step size was selected to be the reference dataset, and error was computed, as shown in Figure 4.11.

There was no clear relationship between step size and error. Furthermore, the magnitude of error was extremely small in comparison to the length scale (3mm) of the simulation, and on the order of numerical error. As long as Newton's method converges with respect to the selected tolerances, the step size does not strongly influence the results.

Table 4.3: Simulation parameters for characterizing step size independence of model

Parameter	**Value**
Type	Deformation
$\hat{\lambda}_{\parallel}$	$1 \rightarrow 0.98$
Init. step size	0.001–0.005
Mesh shape	Rectangular
Texture	Hybrid
BCs	$\boldsymbol{u}(X_1 = X_{1_0}) = (0, 0, 0)$
Mesh dims.	3mm $\times$ 0.5mm $\times$ 0.188mm
Mesh density	5 elements / thickness
Shear modulus	1.0Pa

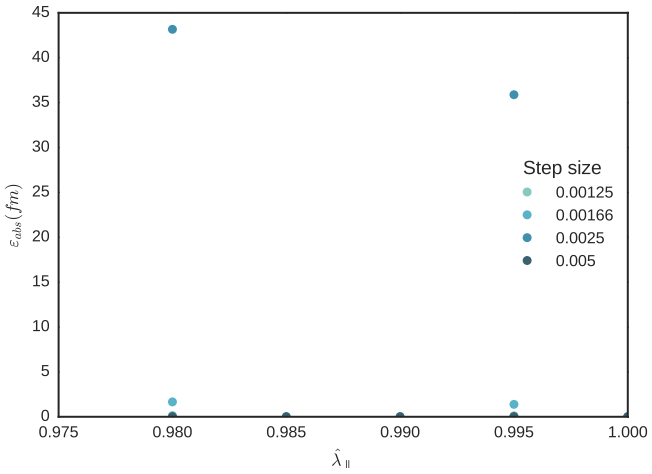

Figure 4.11: Absolute error in position of cantilever tip for simulations of differing step size.

Table 4.4: Simulation parameters for characterizing hysteresis of model

Parameter	**Value**
Type	Deformation
$\hat{\lambda}_{\parallel}$	0.98–0.9875 $\rightarrow$ 0.99
Init. step size	0.00025
Mesh shape	Rectangular
Texture	Hybrid
BCs	$\boldsymbol{u}(X_1 = X_{1_0}) = (0, 0, 0)$
Mesh dims.	3mm $\times$ 0.5mm $\times$ 0.188mm
Mesh density	5 elements / thickness
Shear modulus	1.0Pa

4.4.4 Test for Hysteresis

In a similar vein, it is also of interest to examine whether any hysteresis exists in the simulations, which would indicate the possibility of multiple distinct solutions to the model. To test this, a normal simulation is first performed where $\hat{\lambda}_{\parallel}$ is reached. Then, a new target value of $\hat{\lambda}_{\parallel}$ is chosen to be equal to that of a previously solved step. For the forward part of the cycle, data from the previous run on step size independence with step size of 0.0025 was taken. The solutions for $\lambda_{\parallel} = 0.9800, 0.9825, 0.9850, 0.9875$ were used. For the backward cycle, the objective was set to be $\lambda_{\parallel} = 0.9900$ for all simulations. Parameters are listed in Table 4.4.

To compare the results, the positions of the corners at the free tip of the cantilever were observed at each step of the simulation, as described in Section 4.4.2. All simulations had error values of zero using this metric, indicating that there is no hysteresis effect.

To summarize the findings so far, the curvature metric has poor performance for nearly-flat domains, and for domains with a small length-thickness aspect ratio, but otherwise performs well. By keeping the aspect ratio above 8, a reasonable accuracy can be achieved. Furthermore, the underlying LCE model itself appears to give convergent results for hybrid texture domains, so long as the mesh size is fine enough that two elements span the thickness. As long as the current tolerances for Newton's method are met, step size and step direction is of little importance.

Table 4.5: Simulation parameters for comparing curvature in simulation and experiment

Parameter	**Value**
Type	Deformation
$\hat{\lambda}_{\parallel}$	$1.0 \rightarrow 0.957$
Init. step size	0.00025
Mesh shape	Rectangular
Texture	Hybrid
BCs	$\boldsymbol{u}(X_1 = X_{1_0}) = (0, 0, 0)$
Mesh dims.	650µm × 325µm × 65.8µm
Mesh density	3 elements / thickness
Shear modulus	1.0Pa

4.4.5 Comparison With Experiment

Simulations were performed using stretch factor/temperature relations estimated in Section 4.4.1 from uniform-aligned samples and an idealized hybrid-aligned nematic director profile as in Equation 4.3. Planar anchoring is in the $\boldsymbol{e}_1$-direction and the homeotropic anchoring is the $\boldsymbol{e}_3$-direction. Simulations were performed of the response of a hybrid-aligned LCN cantilever with dimensions to changes in temperature. $\hat{\lambda}_{\parallel}$ was swept from 1.0 to lower values until convergence could no longer be achieved. Other parameters are listed in Table 4.5.

Although the dimensions differ from those of the cantilevers measured experimentally, the curvature is known to be inversely proportional to thickness of the sample for sufficiently long domains [32] and thus the results could be scaled for comparison. Furthermore, since the unscaled curvature of the simulated cantilevers is less, and since the aspect ratio of the domain is closer to unity, a more coarse mesh could be used, substantially reducing the computational complexity of the simulations. Figure 4.12 shows the curvature versus temperature results for both the experimental [1] and simulated LCN cantilevers with 50% M2 composition.

Simulation and experiment show very similar results for this composition. The experimental trends exhibit mild curvature which is not observed in the simulation trend, suggesting that there are some physical details not captured by the model. However, reasonable agreement is obtained over a wide range of temperatures, demonstrating that an accurate prediction of the actuation mode was achieved. Note that the experimental data showed non-negligible hysteresis between the heating and cooling directions.

The same simulation data was also compared to experimental samples with 12% M2,

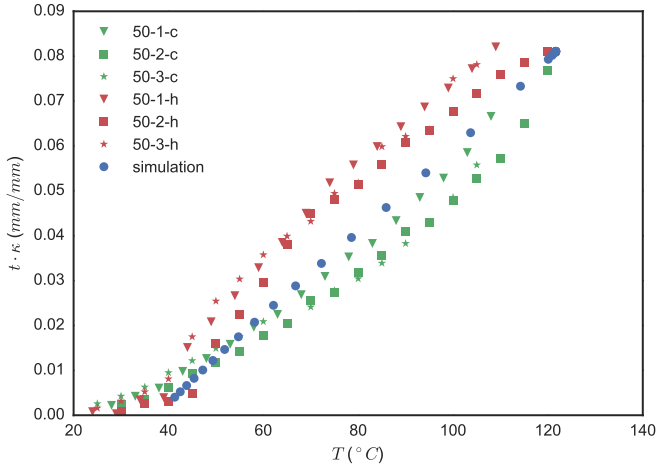

Figure 4.12: Plot of the normalized curvature versus temperature for the experimental and simulated LCN cantilever with 50% M2 composition. The curvature is normalized by the cantilever thickness, as in Sawa *et al.* [32]. Legend indicates experimental sample and whether the data comes from a cooling or heating cycle.

and plotted in Figure 4.13. Unfortunately, only data from the cooling cycle of one experimental sample was available.

In comparison with the samples of 50% M2 composition, the simulation and experiment show very poor agreement for the samples of 12% M2 composition. First, the onset of deformation differs greatly, with the experimental sample starting to deform at 30°C (albeit starting in a bent-backwards position) and the simulation starting to deform at around 45°C. This stems directly from the temperature and thermal expansion data collected in Section 4.2 from planar-aligned samples. Those samples did not show any notable deformation below that temperature where $\hat{\lambda} = 1$ was defined for the simulations. $\hat{\lambda} = 1$ should mark the point of maximum LC ordering, but this point appears to be different between the planar and hybrid 12% samples. This raises a concern that the behaviour of planar samples may not be generalizable to that of hybrid samples, although more research needs to be done to support that hypothesis.

Next, the observed slope is quite different. The shape of the simulation data has a lower slope with upward curvature, in contrast to the experimental data, which is straight until the temperature reaches 80°C. The curvature may indicate a problem with the temperature and thermal expansion model for the 12% samples, as the underlying simulation data has a perfectly linear relation between $\hat{\lambda}_{\parallel}$ and κ. Also, since the data for $\hat{\lambda}(T)$ was only collected

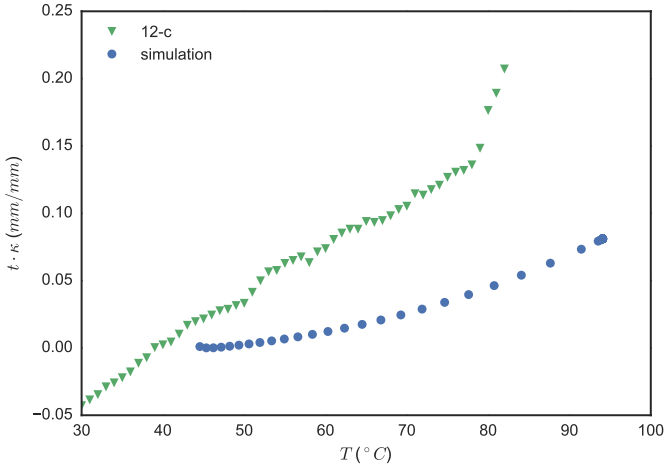

Figure 4.13: Plot of the normalized curvature versus temperature for the experimental and simulated LCN cantilever with 12% M2 composition. The curvature is normalized by the cantilever thickness, as in Sawa *et al.* [32].

in the heating direction for the planar sample, and only the cooling direction for the hybrid sample, error originating in the hysteresis of the samples would be amplified. Finally, the 12% material itself is far more lightly cross-linked than the 50% material; it could simply be that it is outside the range of LCEs well-described by the model.

4.5 Blocking Force of Cantilevers with Hybrid Texture

In addition to the motion of the LCN cantilever, its performance as an actuator also depends on the amount of force it can exert on its surroundings. Measuring this experimentally is complex in that precise control of the conditions of the experiment (e.g., how the sample is clamped) is required to obtain consistent measurements [1]. Furthermore, the geometry of the actuation may be difficult to reconcile with that of the measurement apparatus, particularly if the actuation involves rotation or deformation in multiple axes. On the other hand, simulations overcome these issues and also allow for rapid determination of the sensitivity of the force measurements to the loading configuration.

4.5.1 Blocking Force Procedure

The blocking force is an experimental measurement that is defined by the amount of force required to resist a given deformation; it is a measure of how much force an actuator can exert on its surroundings. In an experiment, an actuator is clamped at one end, and a force sensor is placed so as to obstruct any deformation of the actuator. Then, the actuator is driven, and the resulting force is measured. An example can be seen in ref. 1.

In simulation, a similar procedure can be mimicked. To begin with, a deformation experiment is performed, stopping at the level of stimulus where the blocking force is to be measured. Then, a Neumann boundary condition for an applied traction is placed on a small region of the domain where the force sensor might be placed in a real-world experiment (namely, the part of the actuator which is intended to perform mechanical work).

The direction of the traction should be selected to oppose the observed deformation of the domain. It may be specified in either the material frame or the spatial frame, depending on what is a more natural description for the problem.

The magnitude of the traction is initially chosen to be very small, and the model is solved to determine the deformation (with the original stimulus applied, as well as the opposing traction). The magnitude is then increased step-by-step, and the resulting states of deformation are determined. At each step, the total amount of applied force can be calculated by integrating the traction over the area of the surface it is applied to. This process continues until the domain has been approximately restored to the undeformed state, where the applied force corresponds to the blocking force.

Each step of this process generates a data point consisting of the applied force and the corresponding displacement of the actuator. This can be plotted to understand the mechanical characteristics of the actuator, such as the work it performs:

$$w = \int \boldsymbol{f} \cdot \mathrm{d}\boldsymbol{u} \tag{4.6}$$

In general, the actuation cannot be perfectly counteracted by a traction applied to a small area of the domain. The first consequence of this is that the part of the boundary chosen for the Neumann boundary condition, as well as the direction of traction, should be carefully chosen; if the actuator forms part of a device, the design of the device and the intended loads should serve as a guide for determining these parameters.

In the following simulations, a hybrid cantilever is simulated, and the area of application was selected to be the entire face that forms the free end of the cantilever (i.e., where $\boldsymbol{e}_1$ is at its highest value). The traction is applied in the $\boldsymbol{e}_3$ direction, making it a shear traction.

The second consequence is that a metric is needed which characterizes the distance between the current state of deformation and the undeformed state. This metric guides whether the applied traction should be increased or decreased to measure the blocking force.

For the following simulations, the $\boldsymbol{e}_3$ component of displacement of the free end of the cantilever can be used as the metric; when it equals zero, the blocking force can be measured, and otherwise, its sign and magnitude indicate whether the applied traction should be increased or decreased.

This procedure yields a mechanical understanding of the actuator, while being more flexible than a real-world experiment; as long as appropriate boundary conditions and metrics are formulated, even complex actuations can be characterized.

4.5.2 Mesh Independence

As a basic measure of convergence, the sensitivity of the blocking force to the density of the mesh are considered. Several simulation runs were made using identical parameters except for the mesh density. All simulations used hybrid texture, and the deformation was simulated at $\hat{\lambda}_{\|} = 0.99$. Then, the blocking force was measured in each simulation. Integer numbers of elements per the thickness of the domain were chosen as mesh densities of interest, since the thickness defines the most important length scale for the hybrid texture. Densities of 1, 2, 3, 4, and 5 elements per unit of thickness were selected. Other parameters are listed in Table 4.6.

To compare the results, the blocking force measured at the highest mesh density was used as a reference value, and for the other simulations, the relative error was computed. The results can be seen in Figure 4.14.

At the lowest mesh density examined, the error is substantially higher than other densities, which exhibit a monotonic decrease in error as the density increases, showing numerical convergence for higher mesh densities. With the exception of the lowest density mesh, all simulations exhibited errors with magnitudes less than one percent, which should be sufficiently low for an exploratory design process.

4.5.3 Step Size Independence

As a basic measure of convergence, the sensitivity of the blocking force to the step size of the applied traction are considered. Several simulation runs were made using identical parameters except for the step size. All simulations used hybrid texture, and the deformation

Table 4.6: Simulation parameters for characterizing mesh independence of blocking force

Parameter	**Value**
Type	Blocking force
$\hat{\lambda}_{\parallel}$	0.99
Init. step size	1.0×10^{-5}Pa
Mesh shape	Rectangular
Texture	Hybrid
BCs	$\boldsymbol{u}(X_1 = X_{1_0}) = (0, 0, 0)$; $\boldsymbol{\sigma}(X_1 = X_{1_1}) \cdot \hat{\boldsymbol{k}} = t_{applied}$
Mesh dims.	3mm $\times$ 0.5mm $\times$ 0.188mm
Mesh density	1–5 elements / thickness
Shear modulus	1.0Pa

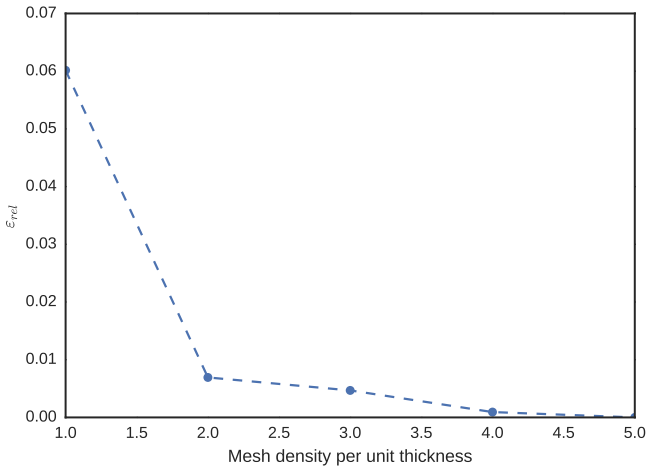

Figure 4.14: Relative error of blocking force for simulations of varying mesh densities, at $\hat{\lambda}_{\parallel} = 0.99$. Density is expressed in units of numbers of elements per unit thickness of the domain.

Table 4.7: Simulation parameters for characterizing step size independence of blocking force

Parameter	**Value**
Type	Blocking force
$\hat{\lambda}_{\parallel}$	0.99
Init. step size	1.0–5.0×10^{-5}Pa
Mesh shape	Rectangular
Texture	Hybrid
BCs	$\boldsymbol{u}(X_1 = X_{1_0}) = (0, 0, 0)$; $\boldsymbol{\sigma}(X_1 = X_{1_1}) \cdot \hat{\boldsymbol{k}} = t_{applied}$
Mesh dims.	3mm $\times$ 0.5mm $\times$ 0.188mm
Mesh density	5 elements / thickness
Shear modulus	1.0Pa

was simulated at $\hat{\lambda}_{\parallel} = 0.99$. Then, the blocking force was measured in each simulation. Unlike in the step size tests for deformation, the blocking force is not known ahead of time, so the step sizes are merely integer multiples of one another, rather than chosen to reach the objective in a particular number of steps. The step sizes used were $1, 2, 3, 4$, and 5×10^{-5}Pa. Other parameters are listed in Table 4.7.

To compare the results, the blocking force measured at the smallest step size was used as a reference value, and for the other simulations, the relative error was computed with respect to this. The results can be seen in Figure 4.15.

No clear relation is found between step size and error in the measurement. Since the errors are all relatively small, this implies that so long as the Newton solver converges according to the chosen tolerances, the choice of step size does not greatly impact the results.

4.5.4 Estimation of the Shear Modulus

The addition of an external force to the simulation makes it necessary to accurately specify the shear modulus in order to obtain quantitative results. Given an accurate value of the shear modulus, simulation and experiment could be compared to see test how accurately the simulation can measure blocking force. But in lieu of such knowledge of the shear modulus, the problem can be approached from the other side: what value of the shear modulus is necessary in order for the simulation and experiment to agree? Although this

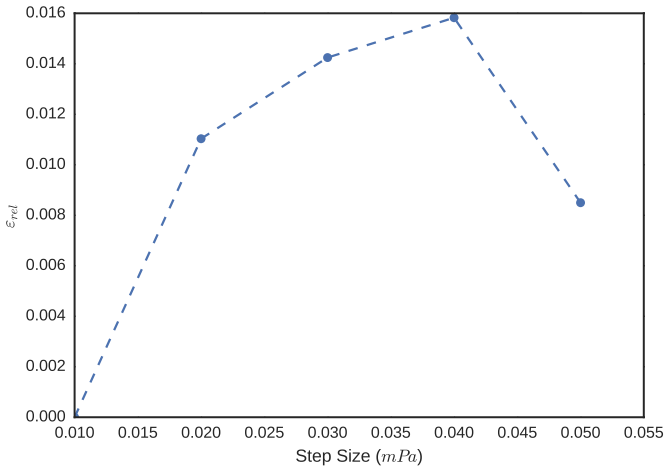

Figure 4.15: Relative error in blocking force for simulations of differing step size (in applied traction).

does not demonstrate the predictive power of the model, it serves as a crude measurement of the shear modulus.

First, a set of test simulations was run to determine the relationship between shear modulus and blocking force in the model. The simulations used rectangular hybrid texture domains with the same dimensions as a set of experimentally-tested samples. The deformation of one such domain was simulated until the point $\hat{\lambda}_{\parallel} \approx 0.996036$. From that point onward, three blocking force simulations were started with different shear moduli. Other parameters can be found in Table 4.8.

It was found that at that fixed value of $\hat{\lambda}_{\parallel}$, there is a linear relationship between the shear modulus and the blocking force measured in the simulation, as seen in Figure 4.16. This result is unsurprising since the shear modulus is linearly proportional to the potential energy density as can be seen in Equation 3.3.

This means that the shear modulus simply scales the results of the blocking force measurements. Given experimental and simulation measurements of the blocking force at a particular temperature, where the simulations initially use some arbitrary shear modulus, the ratio of the two results indicates how much the shear modulus must be scaled in order for simulation and experiment to agree at that temperature.

On the experimental side, data was available for the relationship between blocking force and temperature for hybrid-aligned LCE cantilevers with 50% M2 composition and

Table 4.8: Simulation parameters for characterizing relation between shear modulus and blocking force

Parameter	**Value**
Type	Blocking force
$\hat{\lambda}_{\parallel}$	0.996036
Init. step size	1.0×10^{-7}Pa, 1.0Pa, 2.0Pa
Mesh shape	Rectangular
Texture	Hybrid
BCs	$\boldsymbol{u}(X_1 = X_{1_0}) = (0, 0, 0)$; $\boldsymbol{\sigma}(X_1 = X_{1_1}) \cdot \hat{\boldsymbol{k}} = t_{applied}$
Mesh dims.	13mm $\times$ 0.5mm $\times$ 0.188mm
Mesh density	2 elements / thickness
Shear modulus	1Pa, 5MPa, 10MPa

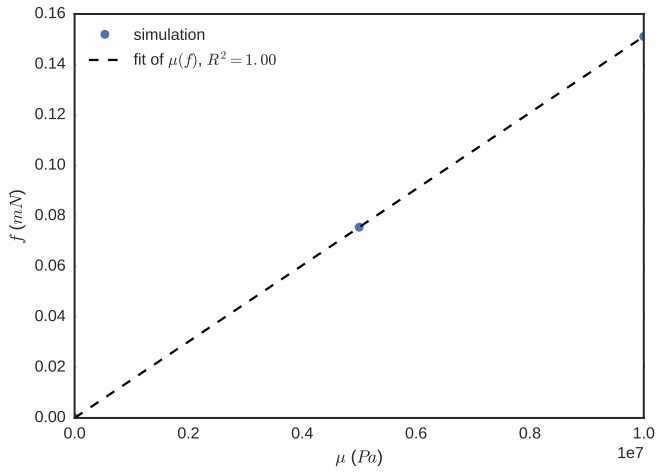

Figure 4.16: Relation between shear modulus and measured blocking force in simulation where $\hat{\lambda}_{\parallel} \approx 0.996036$. Polynomial fit is first-order.

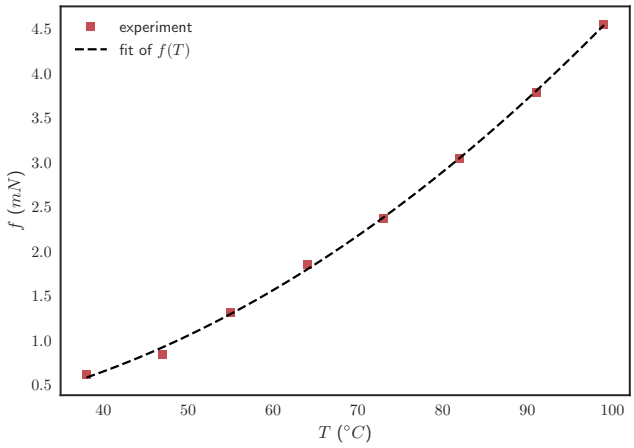

Figure 4.17: Relation between blocking force and temperature for cantilevers with 50% M2 composition and dimensions (13mm $\times$ 2mm $\times$ 0.188mm), along with second-order polynomial fit.

the same physical dimensions. A second-order polynomial fit was made, and the data and fit can be seen in Figure 4.17.

Simulations of the blocking force were run at several temperatures spanning this range. For each simulation, the shear modulus was estimated using the method described above. The resulting temperature trend for the shear modulus is shown in Figure 4.18. Note that at higher temperatures, only the blocking force could be measured (and not the full force-displacement curve), as the simulations with small applied traction (or equivalently, large deformation) encountered numerical problems and did not converge. As such, the initial applied traction is chosen to be sufficiently large that the resulting force is close to the blocking force. Simulation parameters are listed in Table 4.9.

At low temperatures, the shear modulus starts at a very large value and sharply drops as temperature is increased. After a short plateau, the shear modulus appears to slowly increase with temperature. This trend is qualitatively similar to that seen experimentally in other LCEs in the literature where the shear modulus is measured using dynamic mechanical analysis (DMA); elastomers typically have a sharp drop in the shear modulus around the glass transition temperature, and a slow increase afterwards, whether liquid crystalline [70, 71] or isotropic [72].

Although this method is highly impractical for measuring the shear modulus, the phys-

Table 4.9: Simulation parameters for estimating shear modulus

Parameter	**Value**
Type	Blocking force
$\hat{\lambda}_{\parallel}$	0.9725–0.9950
Init. step size	$\approx$ 54–295 µPa
Mesh shape	Rectangular
Texture	Hybrid
BCs	$\boldsymbol{u}(X_1 = X_{1_0}) = (0, 0, 0)$; $\boldsymbol{\sigma}(X_1 = X_{1_1}) \cdot \hat{\boldsymbol{k}} = t_{applied}$
Mesh dims.	13mm $\times$ 0.5mm $\times$ 0.188mm
Mesh density	2 elements / thickness
Shear modulus	1Pa

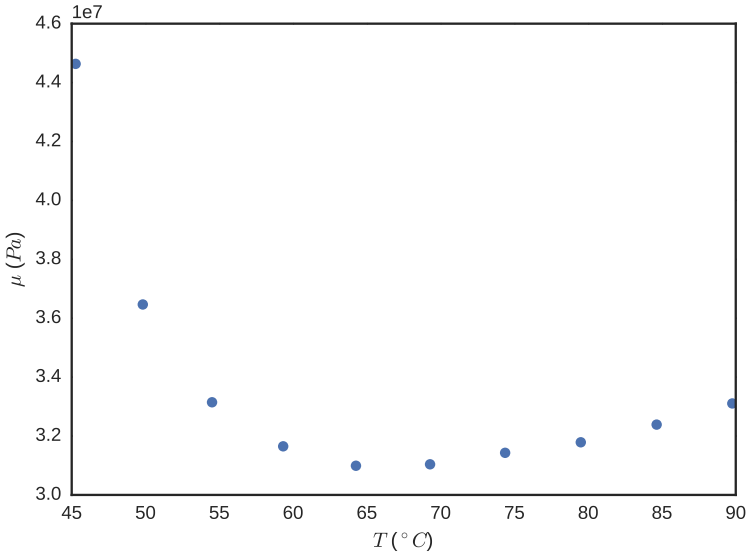

Figure 4.18: Plot of estimated shear modulus versus temperature for the LCN with 50% M2 composition.

ically reasonable trend gives confidence that the model can accurately describe the mechanical properties of LCEs. Still, this agreement should be treated with caution, as there are some differences between the experiment done to measure the blocking force and the simulation. Notably, in the experiment, the film is resting on a flat stage which supports it, while in the simulation the film is merely fixed at one end in a cantilever-like configuration. Additionally, in the experiment, the load is applied normally to the cantilever surface, while in the simulation it is applied as a shear stress. These differences in procedure may subtly change the behaviour of the measurement.

In the context of future work, the question is how the shear modulus might be accurately measured over wide temperature ranges in a more convenient method than a blocking force experiment; the goal of the project is to offer predictive capabilities with minimal upfront investment on the part of the experimentalist. As mentioned previously, dynamic mechanical analysis (DMA) purports to directly measure the shear modulus, but some work may be necessary to reconcile the model used to interpret DMA results and the model used in this work. One path worth pursuing is taking the samples already made for the purpose of measuring $\boldsymbol{C}_*$ and apply simple loading conditions to them parallel and perpendicular to the director and observing the deformation as a function of temperature. This would provide a shear modulus as well as a more absolute notion of the values of $\hat{\lambda}$, rather than setting an arbitrary point to be $\hat{\lambda}_\parallel = \hat{\lambda}_\perp = 1$.

4.6 Conclusions

A hyperelastic solid mechanics model [32] was used to simulate the mechanical response of a nematic LCE to a change in temperature, given knowledge of the nematic texture (imparted during cross-linking) and measurement of mechanical material parameters from uniformly-aligned LCE samples. It was found that in experiment, LCEs do not necessarily exhibit incompressibility; a simple method for reconciling compressible experimental data with incompressible theoretical data was formulated and successfully demonstrated. The simulation method was validated against experimental results for LCE cantilevers resulting from a hybrid-aligned nematic texture; good agreement was achieved for the more densely cross-linked LCE, and poor agreement was achieved for the more sparsely cross-linked LCE. The poor agreement was attributed to mismatch of properties between the samples used for measuring material properties and those used for making actuators. Finally, a method was developed for measuring the force that can be exerted by an LCE actuator and the results showed qualitative agreement with experimental measurements. Working backwards from the experimental measurements, the shear modulus was estimated, showing a temperature

trend similar to other LCEs seen in literature. These results show that the model can be used to accurately and quantitatively simulate the properties of LCEs, but accurately estimating the model parameters remains a challenge.

Chapter 5

Design Study of Multi-legged LCN Gripper

One promising field for application of LCEs is in soft robotics. In ref. 1, Shahsavan *et al.* present a design for a soft robotic gripper made with highly cross-linked LCNs, shown in Figure 5.1a. In that design, several LCN cantilevers are attached to a central circular mounting structure.

Their bottom surface has adhesive properties, so that when the cantilevers are in a flat configuration, the device is capable of adhering to and lifting objects. Each cantilever has hybrid texture, so when the device is heated, the cantilevers peel upward, naturally detaching from the adhered object.

To build the device, multiple components and materials must be integrated together, which complicates the manufacturing process. In this chapter, an alternative design shown in Figure 5.1b is proposed, where the LCE component is made from one monolithic piece, and the texture is crafted to reproduce a similar actuation profile.

5.1 Disk-shaped Domain

A *radial* hybrid-aligned texture, as shown in Figure 5.2, is expected to exhibit bending motion that is omnidirectional, enabling the proposed design. The anchoring conditions for such a texture would require homeotropic anchoring on one bounding surface and radial planar anchoring on the other, resulting in a topological defect with a charge of +1.

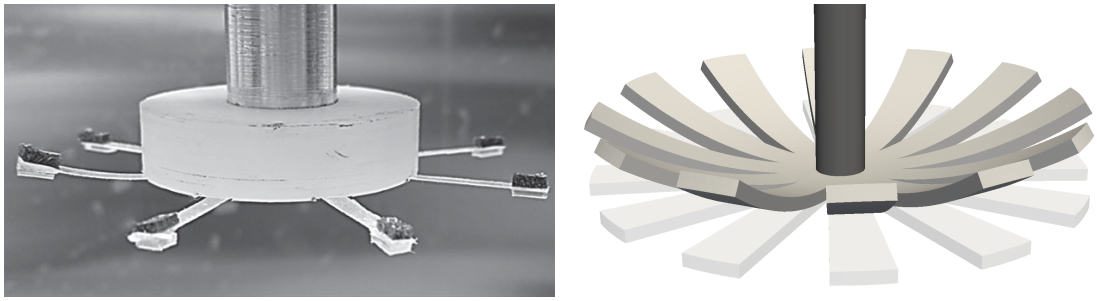

(a) (b)

Figure 5.1: (a) An LCN-based gripper design presented in ref. 1 and (b) the proposed monolithic design.

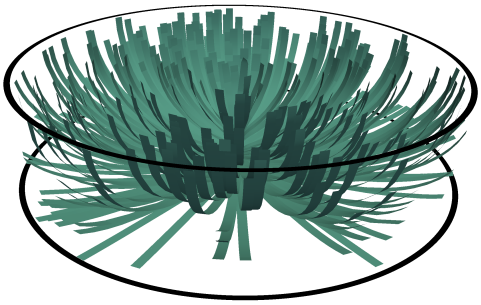

Figure 5.2: Schematic of the director field $\boldsymbol{n}(\boldsymbol{x})$ for an idealized radial hybrid texture.

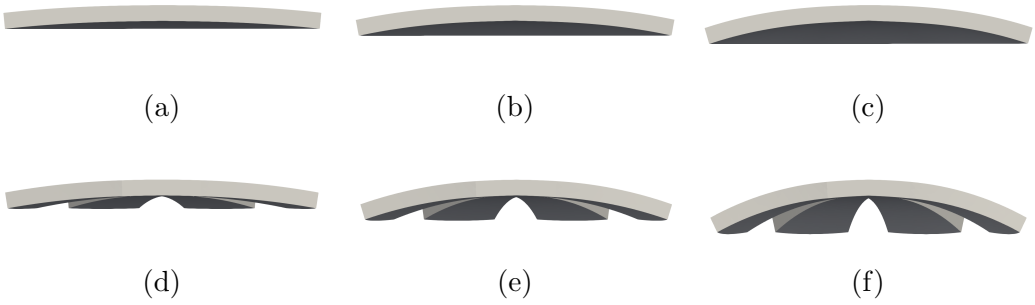

Figure 5.3: (a)–(c) Cutaway views of simulated deformations of an LCN disk with a radial hybrid texture in response to temperature. (d)–(f) Cutaway views of simulated deformations of an LCN flower with eight cuts of depth 750µm and width 300µm. Temperature conditions for each simulation are: (a),(d) $T = 55.60$°C; (b),(e) $T = 74.37$°C; and (c),(f) $T = 94.86$°C.

Unlike the case of the simple cantilever with hybrid texture, the response of an LCN with a radial hybrid-aligned texture is not known *a priori*. It is expected that the omnidirectional bending caused by the radial hybrid texture will result in some frustration due to contraction/expansion in the azimuthal direction. In order to confirm this, a flat disk-shaped LCN domain of radius $r = 1$mm and thickness $t = 0.1$mm with a radial hybrid texture was simulated using the LCN material parameters determined in Section 4.2. Simulations were performed at different temperatures varying from 44–95 °C (as modelled using data from the 50% M2 samples discussed in Chapter 4).

5.2 Flower-shaped Domain

Based upon the frustrated deformations observed in the initial simulations, angled cuts [33] were made in the domain to relieve the frustration through decoupling the expansion/contraction of the LCN azimuthally. This results in a "flower"-like structure where the "petals" can move independently from one another, which was confirmed through simulation. It was also found that these flower-like grippers exhibit a greater range of motion than the disk-shaped domain, compared in Figure 5.3, but it is unclear what shape of cut is optimal or how the mechanical properties of the flower-like gripper are affected.

Given a candidate geometry for simulation-based design, a proof-of-concept factorial design process was performed using the simulation method. Three LCN design factors were investigated (Figure 5.4): (i) radial depth of cuts, (ii) number of evenly-spaced radial

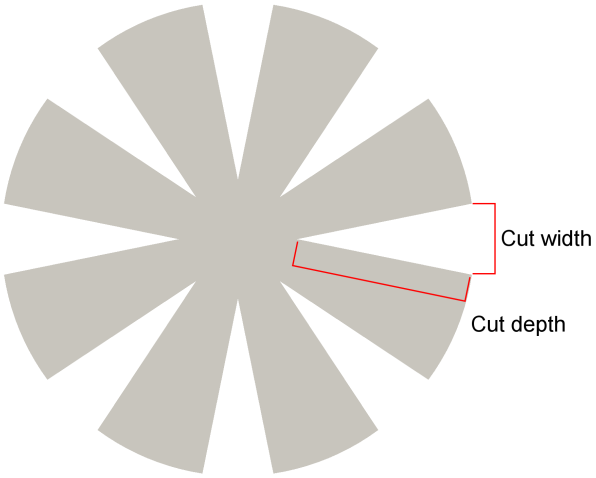

Figure 5.4: Top view of flower-like domain with eight cuts and cut width/depth indicated in red.

cuts, and (iii) width of cuts. Each combination of the three design factors could be easily tested experimentally by making the cuts following cross-linking of a disk-like radial hybrid-aligned LCN sample.

The proof-of-concept factorial design study (i.e., trying each combination of a set of variables) was performed with two levels for each design factor. This results in 2^3 individual geometries where each requires a set of simulations to be performed over a range of operating temperatures. The design factor levels and other parameters are listed in Table 5.1.

Three performance metrics were computed from simulations at $T = 74.37°\text{C}$: tip displacement, blocking force, and the energy density. Tip displacement was measured by calculating the magnitude of the displacement vector in $\boldsymbol{e}_3$ at the petal tips. Blocking force was measured using the same method previously described for the cantilever case, except that the surface traction was applied at the outer circumference of each petal instead of at the end of the cantilever. The shear modulus was estimated at this temperature by applying a cubic interpolating spline to the data collected in Section 4.5.4. Energy density was calculated by integrating the resulting force-displacement curve to determine the amount of work performed, then dividing by the volume of the domain.

In order to roughly characterize the influence of each variable and reveal interaction effects between variables, a linear model was fit for each performance metric using the

Table 5.1: Simulation parameters for factorial study of flower-shaped domain

Parameter	**Value**
Type	Blocking force
$\hat{\lambda}_{\parallel}$	0.98
Init. step size	3.14 kPa
Mesh shape	Cylindrical
Texture	Radial Hybrid
BCs	$\boldsymbol{u}(r = 0, X_3 = X_{3_0}) = (0, 0, 0)$; $\boldsymbol{u}(r = 0, X_3 = X_{3_1}) = (0, 0, u_3)$; $\boldsymbol{\sigma}(r = R) \cdot \hat{\boldsymbol{k}} = t_{applied}$
Mesh dims.	$R = 1\text{mm}, t = 0.1\text{mm}$
Cut depth	500–750 µm
No. cuts	4–8
Cut width	200–300 µm
Mesh density	2 elements / thickness
Shear modulus	31.43MPa

following form:

$$\hat{y} = \bar{y} + \beta_{\#} x_{\#} + \beta_d x_d + \beta_w x_w + \beta_{\#d} x_{\#} x_d + \dots \tag{5.1}$$

Each coefficient β represents the effect of a corresponding variable (or interaction between multiple variables), where the subscripts $\#$, d, and w refer to the number of cuts, cut depth, and cut width, respectively. In the model, variables are scaled such that $x = -1$ corresponds to the low level and $x = +1$ corresponds to the high level of each variable.

It is important to emphasize that this model is not intended to fully and precisely capture the behaviour of the proposed design. In an iterative design process, this model would represent a single iteration, and the results would be used to choose design factors and levels for the next set of simulations so that a more optimal design could be found.

The force-displacement curves collected are plotted in Figure 5.5. The fitted model parameters are listed in Table 5.2 and raw simulation data is provided in Appendix C. A rendering of the resulting deformation of one of the flower-like gripper designs is shown in Figures 5.3d–5.3f.

For the tip displacement, cut depth exerts the largest influence on the resulting deformation by an order of magnitude, while cut width has a negligible effect. Two-factor and three-factor interactions were similarly small in magnitude. For the blocking force, all the terms were negative except for the cut number–cut width interaction term. Cut depth had

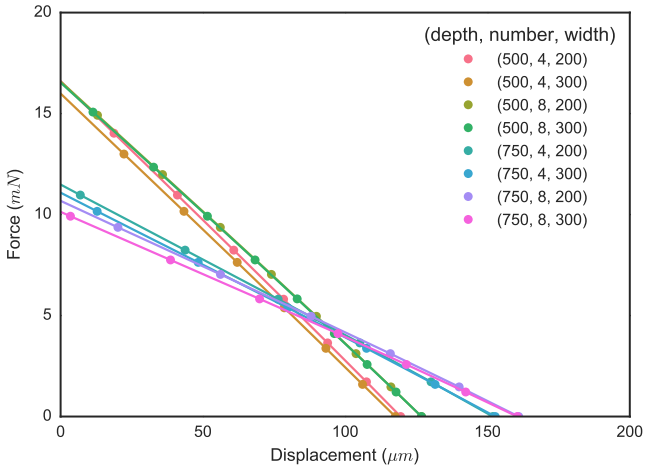

Figure 5.5: Plot of force versus displacement for radial hybrid domains with cuts of varying number and dimensions. Legend shows design parameters used for cuts.

Table 5.2: Fitted coefficients for effects of cuts on mechanical properties of radial hybrid domains.

	Tip displacement (µm)	Blocking force (mN)	Energy density (kJ/m^3)
$\bar{y}$	139.59	13.64	3.52
$\beta_{\#}$	4.16	-0.15	0.27
β_d	16.91	-2.79	-0.17
β_w	-0.19	-0.20	0.07
$\beta_{\#d}$	0.03	-0.28	-0.06
$\beta_{\#w}$	0.06	0.05	0.07
β_{dw}	0.27	-0.03	0.01
$\beta_{\#dw}$	-0.41	-0.09	-0.02

the largest influence on blocking force. This highlights the tradeoff between the force that can be exerted by an actuator and the size of its deformation. For the energy density, the number of cuts is the most influential parameter, as increasing the number of cuts leads to a larger deformation with a relatively small tradeoff in blocking force, as well as reducing the volume of the actuator. Cut depth has a negative effect of similar magnitude.

5.3 Conclusions

A proof-of-concept simulation-based design study was performed, analyzing and optimizing the performance of an alternative to the LCE multi-legged gripper design proposed in ref. 1. These results represent a significant step towards simulation-based design of LCE materials which has the potential to overcome its inherent complexity and cost.

It was found that LCEs with non-trivial textures may show mechanical frustration. By modifying the shape of the domain, this frustration can be relieved, resulting in a larger response to stimuli. Mechanical properties can be tuned to the desired application.

Chapter 6

Design Study of LCN Hinge Actuators

In this chapter, a relatively complex type of actuator which undergoes hinge-like folding in response to temperature will be investigated. Initially, the same approach as in the previous study will be taken in that candidate LCE textures will be assumed and their thermomechanical response simulated. Preliminary results will then be shown for an extension to the LCE simulation method which enables simulation-based prediction of the nematic texture "frozen-in" during cross-linking, given geometry and surface anchoring conditions of the LCE precursor nematic phase.

6.1 Introduction

When facing a complex problem, a generic and highly effective strategy is to break the problem down into several smaller sub-problems, solve each of them individually, and compose the solutions from each sub-problem into the overall solution. In the field of computer algorithms, this principle is captured by the phrase "divide and conquer", but applications of this strategy can be found across all fields, such as the use of separation of variables to solve partial differential equations, or the Born-Oppenheimer approximation in chemistry. In the context of LCE design, a complex problem might consist of solving the inverse problem for a large domain which is supposed to undergo some highly non-trivial deformation. To break it down into sub-problems, one could look at small localized areas of the domain and see if the local deformation could be described as some combination of

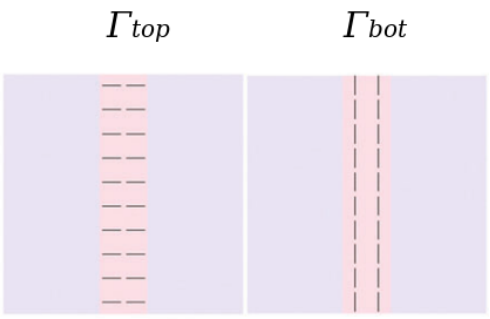

Figure 6.1: Anchoring conditions for top and bottom surfaces used to make LCE with TN texture occupying 20% of the domain. Taken from [62].

extension/contraction, bending, and twisting, or else some other set of elementary deformations.

Solving the inverse problem for those elementary deformations would result in a family of LCE structural elements. Larger inverse problems could then be solved by combining these structural elements in a modular fashion as appropriate. To that end, it would be highly beneficial to find and characterize a family of basic structural elements for LCE deformations.

Fuchi *et al.* [62] present a research study involving the optimization of LCE-based hinge actuators using a simple LCE mechanical model under the assumption that complex nematic textures may be imposed. Their approach involves optimization starting with an initially simple nematic texture, the twisted nematic (TN) cell. This nematic texture is known to exhibit thermomechanical bending, albeit with an undesirable saddle-like shape. In their work, they performed optimization of the nematic texture given access to a photoalignment method which allows the imposition of relatively complex spatially varying textures without the use of traditional surface anchoring techniques. They were able to determine a nematic texture which results in a hinge-like folding mechanism with less saddle-like character compared to the simple TN texture.

Fuchi *et al.* made two variants of the "unoptimized" texture experimentally. In one, 20% of the domain is a contiguous stripe of TN texture, and in the other, 40% of the domain is TN. The remainder of the domain is "inactive" and does not deform substantially in response to stimuli. The anchoring conditions used to make the domain are shown in Figure 6.1.

Curiously, both samples exhibit roughly the same bending response to temperature; the 40% TN sample bends marginally more than the 20% sample, but clearly not twice as

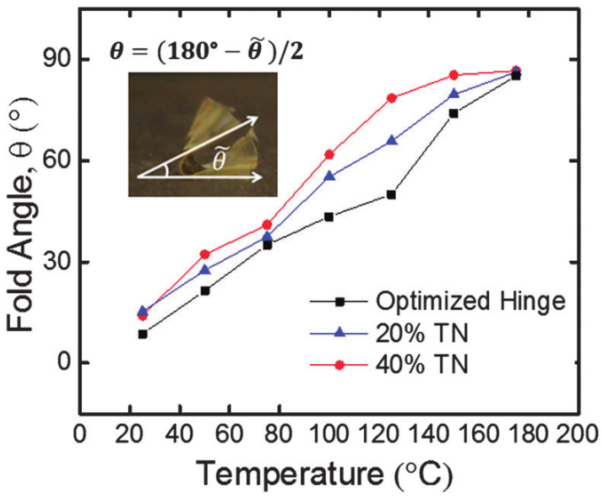

Figure 6.2: Experimentally-measured bending response of LCEs with different textures. Taken from [62].

much, even though there is twice as much active area, as seen in Figure 6.2. This suggests that there is some mechanical frustration in larger TN domains that dampens their bending response.

In this work, an LCE hinge actuator that can be produced with simpler surface alignment methods is studied. Simulation studies are performed in order to determine nematic textures which result in LCE hinge actuators with the largest bending response to stimuli. In addition to simulation of the LCE thermomechanical response, nematic texture simulations are performed to predict the resulting "frozen-in" texture through modelling the nematic precursor to the LCE.

6.2 Methods

6.2.1 Hinge Angle Metric

The hinge angle metric describes the amount of bending observed at a particular state of deformation. It is computed by estimating the slope of the domain near the fixed and free ends, and computing the difference in angle between the two corresponding vectors. In all samples, the $\boldsymbol{e}_2$ direction was the bending axis. Dirichlet boundary conditions were used to fix the face at $X_1 = 0$ in place, and the face at $X_1 = \ell$ is considered the "free end" of

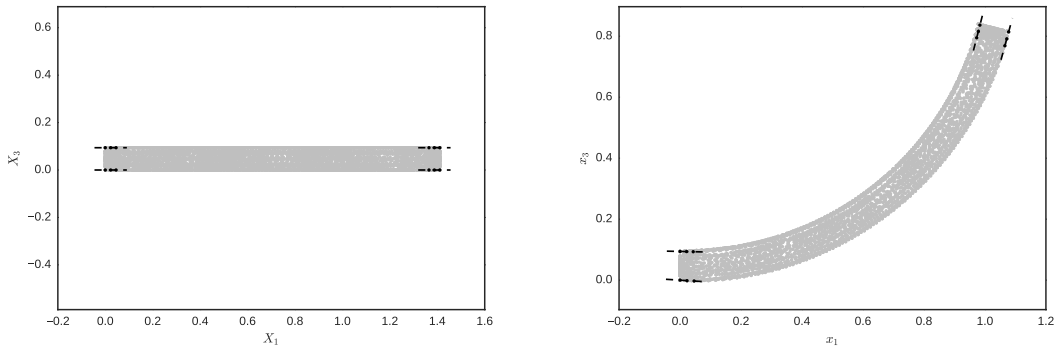

(a) (b)

Figure 6.3: Visualization of hinge metric as applied to TN domain (a) in un-deformed state, and (b) in deformed state.

the hinge. The face at $X_3 = 0$ is considered the bottom face, and the face at $X_3 = t$ is considered the top.

To estimate the slope, several mesh points are taken from the top and bottom edges of the domain near the fixed and free ends. Due to the saddle-like shape of deformations exhibited by the TN samples, there is some additional curvature along the $\boldsymbol{e}_2$ direction, making it harder to estimate the slope; thus, points not originally located at $X_2 = 0$ were not considered. Of the final set of points, four first order polynomials are fit; one is fit for each combination of (fixed end/free end) and (top/bottom surface). This is illustrated in Figure 6.3.

The angles are computed from these slopes, and the differences between the angles in the fixed and free end are computed separately for the top and bottom surfaces. Finally, these differences in angle are averaged to get the metric.

6.2.2 Nematic Texture Dynamics Model

In this work, the Landau-de Gennes model is used to model texture dynamics of the nematic precursor of the LCE domain. The Landau-de Gennes model of the nematic phase is a power series approximation of the free energy density with respect to the alignment tensor $\boldsymbol{Q}$ [10] (see Section 2.1.2). It belongs to a broader class of models derived from the Landau theory of phase transitions, and as such, can be used to model nematic order in conditions near the nematic-isotropic phase transition.

The free energy density in the bulk of the domain can be written concisely as [73]:

$$f_b(\boldsymbol{Q}, \boldsymbol{\nabla Q}, T) = f_{iso} + f_{nb}(\boldsymbol{Q}, T) + f_{ne}(\boldsymbol{Q}, \boldsymbol{\nabla Q}) \tag{6.1}$$

where the contributions originate from the isotropic phase, thermodynamically-mediated nematic alignment, and distortions to nematic order, respectively. Full expressions for the terms can be found in refs. 73 and 74.

The free energy contribution from surface boundary conditions is expressed by defining a uniaxial preferred alignment direction $\boldsymbol{n}$ along that boundary and penalizing deviations from it using a second-order expression [75]:

$$f_s = \alpha \left(\boldsymbol{Q} - \boldsymbol{Q}_{pref}\right) : \left(\boldsymbol{Q} - \boldsymbol{Q}_{pref}\right) \tag{6.2}$$

$$\boldsymbol{Q}_{pref} = S_{eq}\left(\boldsymbol{nn} - \frac{1}{3}\boldsymbol{\delta}\right) \tag{6.3}$$

where α is the anchoring strength and S_{eq} is the magnitude of nematic order. The total free energy of the nematic domain is then [73]:

$$F[Q_{ij}] = \int_V f_b \, dV + \int_S f_s \, dS. \tag{6.4}$$

This is reformulated using the time-dependent Ginzburg-Landau model, resulting in a dynamic model that evolves toward equilibrium (i.e., where the state of $\boldsymbol{Q}$ across the domain minimizes the total free energy) [73]. The expression is taken from ref. 73:

$$\mu_r \frac{\partial Q_{ij}}{\partial t} = -\left[\frac{\partial f_b}{\partial Q_{ij}} - \partial_k\left(\frac{\partial f_b}{\partial(\partial_k Q_{ij})}\right)\right]^{ST} \tag{6.5}$$

where μ_r is the rotational viscosity of the nematic phase, and the ST superscript indicates the symmetric and traceless component of the resulting tensor.

The model is solved using the finite element for spatial discretization and a time-adaptive second-order implicit method for time discretization. The model and solver are implemented using `FEniCS`, as with the LCE mechanical model. Progress toward equilibrium is tracked by rate of change of the solution $\frac{\mathrm{d}Q}{\mathrm{d}t}$, a scalar computed using a finite difference as follows:

$$\frac{\mathrm{d}Q}{\mathrm{d}t}\Big|_{t_i} \approx \frac{\left\|\boldsymbol{Q}_{t_i} - \boldsymbol{Q}_{t_{i-1}}\right\|}{t_i - t_{i-1}} \tag{6.6}$$

When $\frac{\mathrm{d}Q}{\mathrm{d}t}$ falls below a set threshold, the simulation is stopped.

6.3 Results & Discussion

First, several mechanical studies are performed on several variations of the texture of interest. Then, a texture modelling study is performed to try and reproduce one of the variants and determine its experimental viability.

6.3.1 Sensitivity of Bending Response to Various Parameters

To provide a starting point for the investigation, an analysis was performed of the sensitivity of the bending response to several variables. A full factorial design of three variables and two levels per variable was used. As in Fuchi *et al.*'s work [62], the domain consists of a rectangular domain with a subset containing a hinge or "active" texture and the remainder containing an "inactive" texture. The first variable was the volume fraction occupied by the hinge that had levels (10%, 30%). The second variable concerns the spatial arrangement of active and inactive regions.

In Fuchi *et al.*'s work, increasing the size of the TN domain appears to have a very small effect on the bending response. This is surprising, since a larger active bending region should have a larger bending response. One possible explanation is that the TN domain is mechanically frustrated, and that the increased frustration in a larger domain is enough to cancel out the anticipated increase in bending response. In this case, multiple independent TN domains should have a larger bending response than one larger contiguous TN domain. To test this hypothesis, domains with multiple independent TN domains were made by separating them with inactive regions. For simplicity, the layout of active and inactive regions was restricted to a sequence of alternating blocks, with the first and last blocks always being inactive. The key variable was the number of active blocks, with levels (1, 3). This variable is independent of the volume fraction of hinge texture, so that it merely represents how the hinge texture is spatially arranged, and not the volume of active region. A schematic of this is shown in Figure 6.4.

At the time of writing, the simulation method does not support entirely inert regions of LCE, as the entire domain is assumed to have a defined director and a spatially homogeneous magnitude of nematic order. As a substitute, a uniform nematic alignment is used in the "inactive region", oriented along the length of the domain; consequently, this region deforms slightly in response to stimuli. The third variable was simply whether the active texture was TN or hybrid, in case the two textures had substantially different sensitivity to the other variables. Other parameters are listed in Table 6.1.

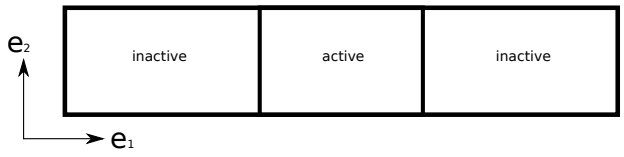

(a)

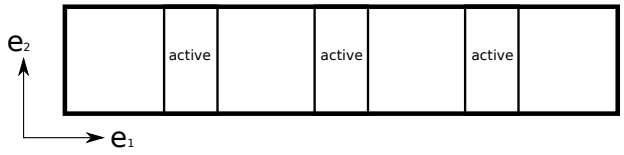

(b)

Figure 6.4: Layout of domains in a hinge with 30% active region divided into (a) 1 block and (b) 3 blocks.

Table 6.1: Simulation parameters for factorial study of hinge actuators

Parameter	**Value**
Type	Deformation
$\hat{\lambda}_{\parallel}$	$1.0 \rightarrow 0.95$
Init. step size	0.001
Mesh shape	Rectangular
Texture	Hybrid, TN, Uniform
BCs	$\boldsymbol{u}(X_1 = X_{1_0}) = (0, 0, 0)$
Mesh dims.	2.5mm $\times$ 0.5mm $\times$ 94µm
Mesh density	3 elements / thickness
Shear modulus	1.0Pa

Hinge angle was measured for each simulation and is plotted as a function of $\hat{\lambda}_{\|}$ in Figure 6.5. The volume fraction of the active region appears to be the most influential variable in governing the bending response, contrary to the results shown in Fuchi *et al.*'s work [62]. It can be seen that splitting the active region in the multiple blocks decreases the response by a small amount—this is most likely a byproduct of the texture near the boundaries between active and inactive regions, which continuously transforms from active to inactive. Hybrid texture also shows a marginally larger response than TN when all other parameters are equal.

6.3.2 Bending Response of Pure TN Domains of Varying Length

In Fuchi *et al.*'s work [62], the size of the hinge region was only weakly correlated with the magnitude of bending response, while in the previous set of simulations, the size of the hinge region was observed to be roughly linearly correlated.

One possible culprit is the neglect of soft elasticity and director reorientation in the model. It is conceivable that the internal stresses created by the folding deformation are sufficient to drive director reorientation in the sample; however, this should result in behaviour opposite from what is observed, with the simulated LCE acting stiffer and less soft than the true material.

It is also possible that the domain size and aspect ratio are key variables in the behaviour of the hinge. Due to limitations of computational resources, small domains with high length:width aspect ratios and low length:thickness aspect ratios were simulated, as compared with the relatively large, square, and thin experimental samples in ref. 62.

To investigate the influence of sample dimensions, a small study was performed with rectangular domains which only have TN texture. In this study, the bending response is measured for TN domains of varying length and width, with every combination of 5 lengths and 2 widths. Other sample parameters are listed in Table 6.2.

For both widths, longer samples encountered convergence problems as $\hat{\lambda}_{\|}$ progressed to lower values, and the simulations were terminated at $\hat{\lambda}_{\|} \approx 0.98$. The hinge angle was measured at this point, and the results from each simulation are plotted in Figure 6.6. Since data was not collected at exactly $\hat{\lambda}_{\|} = 0.98$, the hinge angle was estimated using a cubic interpolating spline of hinge angle as a function of $\hat{\lambda}_{\|}$ for each simulation.

Samples of both widths exhibit an approximately linear relationship between hinge angle and length of the TN domain. The points do not fall in a perfectly straight line, but

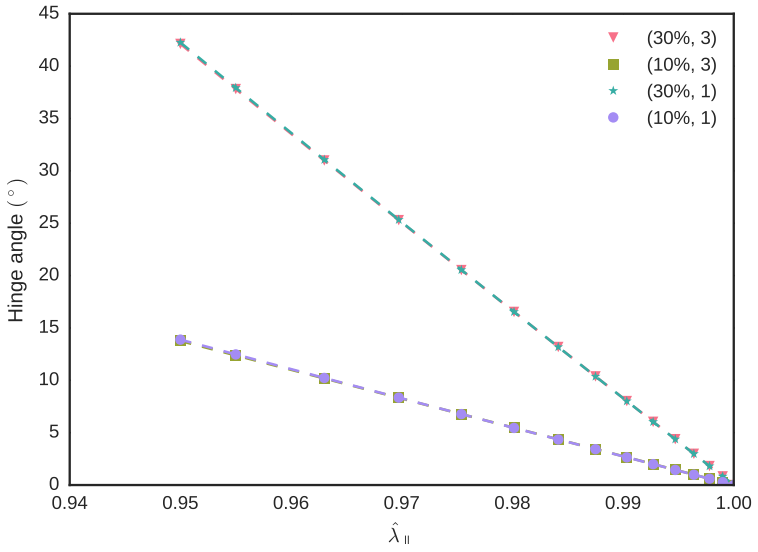

(a)

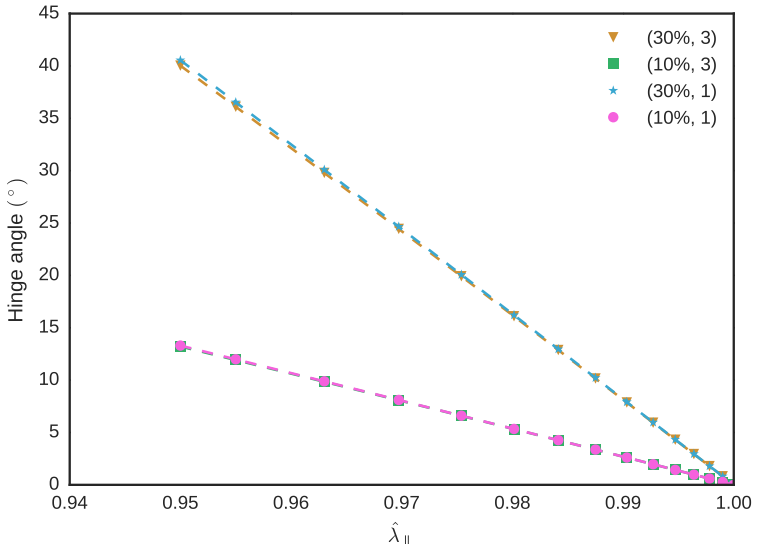

(b)

Figure 6.5: Bending response to temperature for domains with (a) hybrid texture, and (b) TN texture. Legend indicates volume fraction of active region and number of active blocks. Dashed lines are cubic interpolating splines.

Table 6.2: Simulation parameters for variable-length TN hinges

Parameter	**Value**
Type	Deformation
$\hat{\lambda}_{\parallel}$	$1.0 \rightarrow 0.95$
Init. step size	0.001
Mesh shape	Rectangular
Texture	TN
BCs	$\boldsymbol{u}(X_1 = X_{1_0}) = (0, 0, 0)$
Mesh dims.	0.182–1.82 mm $\times$ 0.25–0.50mm $\times$ 94µm
Mesh density	3 elements / thickness
Shear modulus	1.0Pa

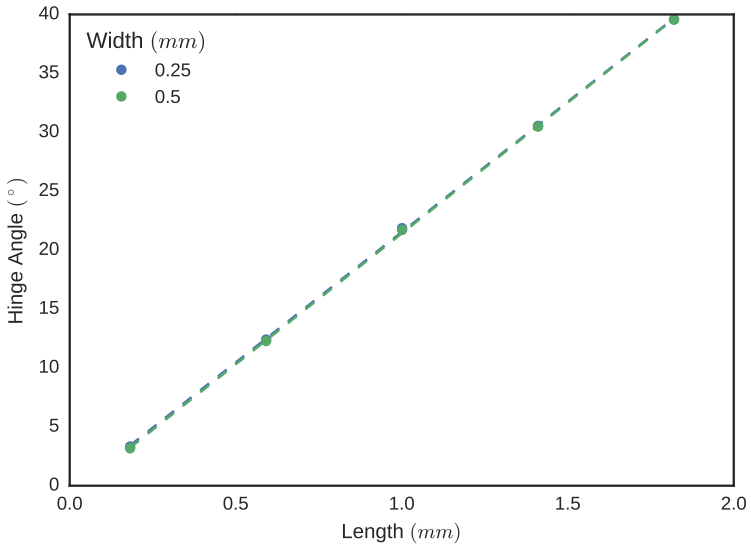

Figure 6.6: Hinge angle observed at $\hat{\lambda}_{\parallel} = 0.98$ for TN domains of varying length and width. Dashed lines show first-order polynomial fit.

given the error inherent in the hinge angle measurement, the significance of this is dubious. Width does not appear to have any influence on the outcome.

In summary, none of the samples simulated showed evidence that TN hinges have a maximum effective size. Again, since the dimensions of the samples simulated are so different from the dimensions of the experimentally-tested samples in ref. 62, it is difficult to say whether the simulation is at fault, or whether the effect is merely insignificant in the simulated samples.

6.3.3 Nematic Reorientation Dynamics

Although the simulations in the previous section were inconclusive, the concept of splitting an active LCE region into multiple parts may still have merit in experimentally-accessible length scales. In future work, these simulations may be able to catch up to experiment and reproduce results such as in Fuchi *et al.* [62] and make further progress in this area.

Of course, in order to simulate the functional mechanical properties of LCEs, the underlying nematic texture "frozen-in" after cross-linking must be known. However, all past research in modelling the mechanics of LCEs has either involved very simple textures (pure splay/twist/bend) or made *ad hoc* assumptions about the texture, as in the previous section. Even experimental works which impose a desired texture with a high degree of control [62, 8] do not have a high-resolution means of inspecting the local LC texture, meaning that the actual texture may differ subtly or greatly from the imposed design. In the context of simulation-assisted design, this highlights a gap between the LCEs that can be modelled and simulated, and the LCEs that can be created experimentally.

Prior to cross-linking, domains composed mainly of LCE monomers exhibit a low molecular mass nematic phase where traditional LC dynamics models can be used to model the texture. These models could form the first stage of a simulation-based LCE "design pipeline" in order to close this gap. Fabrication conditions for the alignment of the LCE prior to cross-linking could be specified in these models, and solving them would result in a high-resolution and physically-accurate texture that would form the initial conditions of the mechanical LCE simulations that are the focus of this thesis.

The integration of simulations of nematic texture formation prior to cross-linking and the resulting functional mechanical properties of the LCE after cross-linking would provide both fundamental and applied researchers with a necessary tool for rational design of LCE-based experiments and devices.

Two classes of these models exist relevant to macroscale nematic reorientation dynamics simulation: nematic director models (Leslie-Ericksen) and alignment tensor models

(Landau-de Gennes) with the latter being the most descriptive in that it is able to capture orientational defects (disclinations) and phase transitions (isotropic-nematic).

In this section, a naïve fabrication procedure for one of the previously-simulated hinges is proposed, and a dynamic nematic texture simulation using a Landau-de Gennes model is applied to determine how closely the resulting texture matches the desired texture. Evidence is found that the proposed fabrication procedure results in the formation of defects in the nematic texture. The detailed structure of the defects remains uncertain, but as the LCE mechanical simulations are not equipped to handle defects, the investigation is stopped at this point. Future work is required to fully determine the texture and to accurately simulate the deformation of the resulting LCE.

Hinge Domain and Proposed Fabrication Procedure

The hinges studied previously contained alternating domains of uniform and TN texture. When considered individually, each of those domains can be easily created with surface anchoring methods. Consider a rectangular domain with large lateral dimensions and a small thickness. To create uniformly-aligned texture, the top and bottom surfaces should both be treated so that they impose anchoring along the same direction. To create a TN texture, the top and bottom surfaces should both have planar anchoring, but aligned perpendicularly to one another. If the domain is filled with an LC compound in its isotropic phase and then cooled slightly below the nematic-isotropic transition temperature, a nematic phase will grow inward from the boundaries. In the case of the TN domain, the disagreement in the director between the top and bottom surface will be resolved by a smooth variation in the director through the thickness of the domain.

In the case of the hinge, the domain contains alternating regions of uniform and TN texture. To create this domain with surface anchoring methods, a naïve approach is to simply combine the anchoring conditions of the individual domains so that they match the desired texture. However, this will result in a discontinuity in the anchoring conditions on the boundary between the TN and uniform regions. It is difficult to predict how the texture will behave in this local area, thus motivating the use of texture modelling of these conditions.

Although many variations of hinges were examined previously, here the simplest case that still contains the same symmetry as the previously-studied designs in Section 6.3.1 was studied. The domain contained one region with TN anchoring, surrounded by two regions with uniform anchoring along the length of the domain, as depicted in Figure 6.7.

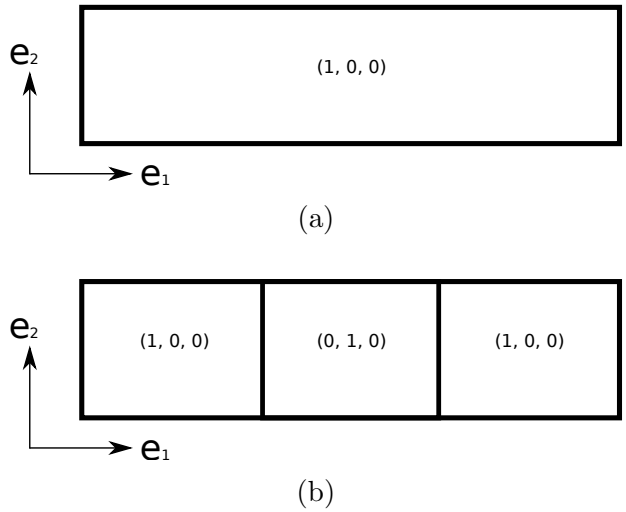

Figure 6.7: Proposed anchoring orientation for hinge domain on (a) top boundary, and (b) bottom boundary.

Simulation Conditions

The total dimensions of the domain were (9.6µm×0.8µm×0.4µm). The density of the mesh was initially 8 units spanning the thickness of the domain (corresponding to one element per 50nm) and later increased to a higher density of 13.3 units spanning the thickness of the domain (corresponding to one element per 30nm) as described later.

The use of two different mesh densities was used in order to speed up the initial equilibration while achieving a higher resolution end result. The initial simulation used the coarser mesh as previously described, and ran from the initial conditions until equilibration, which was defined to be the point where $\frac{\mathrm{d}Q}{\mathrm{d}t} \leq 5.0 \times 10^{-9}\mathrm{s}^{-1}$. After that simulation finished, the result were interpolated onto the higher density mesh, and a new simulation run to equilibrium using the previous result as initial conditions.

The LC medium also requires its own set of physical parameters. Initially, it was planned to measure the material parameters of the LCE monomers M1 and M2 described in Section 4.1, and use them for texture modelling. Unfortunately, the data could not be collected by the time of writing. Instead, material parameters for pentyl-cyanobiphenyl (5CB), a well-known LC compound, were used. This means that the results can only be interpreted qualitatively, and as a proof-of-concept. In future work, this study should use the material parameters of the LCE monomer being studied in order to get quantitatively accurate results.

Table 6.3: Material parameters for 5CB. Values taken from [74].

T_{ni}	307.35	K
T	307	K
a_0	1.4×10^6	$\mathrm{J/m^3K}$
b	1.8×10^6	$\mathrm{J/m^3}$
c	3.6×10^6	$\mathrm{J/m^3}$
L_1	9.1×10^{-12}	J/m
L_2	4.4×10^{-12}	J/m
L_3	7.1×10^{-12}	J/m
L_{24}	4.2×10^{-12}	J/m

Material parameters for 5CB are listed in Table 6.3, as derived from measurements made at a temperature of 307K [74]:

The boundary conditions consist of two surfaces with Neumann boundary conditions as detailed in Section 6.2.2. The preferred anchoring directions are as follows:

- The top surface ($X_3 = 0.4\mu\mathrm{m}$) had uniform anchoring along the $\boldsymbol{e}_1$ direction.
- The bottom surface ($X_3 = 0.0\mu\mathrm{m}$) had uniform anchoring along the $\boldsymbol{e}_1$ direction within the regions intended to develop uniform texture, and along the $\boldsymbol{e}_2$ direction in within the regions intended to develop TN texture.

Since the finite element formulation uses continuous interpolants to represent the solution, discontinuities in the boundary conditions are thought to artificially increase the amount of numerical error in the solution. As a countermeasure, the anchoring on the bottom surface was reformulated to smoothly transition between the two regions as follows: Each of the components of the anchoring alignment (in vector form) were composed of a weighted average of $\boldsymbol{a} = (1, 0, 0)$ and $\boldsymbol{b} = (0, 1, 0)$.

$$\boldsymbol{n}(X_1) = (1 - w(X_1))\boldsymbol{a} + w(X_1)\boldsymbol{b} \tag{6.7}$$

This vector was re-normalized so that the alignment direction is a unit vector across all parts of the surface. The weighting function is the difference of two sigmoid functions:

$$w(x) = S(x - x_\ell) - S(x - x_r) \tag{6.8}$$

$$S(t) = \frac{1}{1 + \exp(-kt)} \tag{6.9}$$

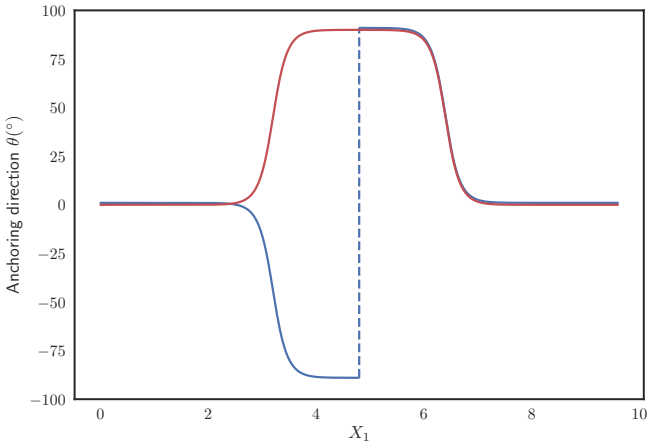

Figure 6.8: Both variations of in-plane direction of anchoring in texture modelling simulations. $\theta = 0°$ corresponds to alignment with $\boldsymbol{e}_1$, and $\theta = 90°$ corresponds to alignment with $\boldsymbol{e}_2$. Note that $\pm 90°$ result in identical nematic order. Values have been slightly shifted for visual clarity.

where $S(t) \in (0, 1)$, $x_\ell = 3.2\text{µm}$ and $x_r = 6.4\text{µm}$ are the left and right bounds of the TN region, respectively, and $k = 6\text{µm}^{-1}$ is a steepness parameter for the sigmoid function.

This smoothing process introduces an additional problem by imposing a particular symmetry on the domain. Since the anchoring direction rotates by 90°, it can rotate either clockwise or counter-clockwise between $\boldsymbol{a}$ and $\boldsymbol{b}$. In the above formulation, the anchoring rotates in the same direction across both uniform-TN boundaries. There is only one alternative, which is that the anchoring rotates in opposite directions across the uniform-TN boundaries. Thus, two independent simulations are run with these two types of anchoring conditions. The anchoring orientation in these two simulations is visualized in Figure 6.8.

These two boundaries had anchoring strengths of $1.0 \times 10^{-2}\text{Jm}^{-2}$. The remaining boundaries had no form of anchoring applied to them. This differs from a more realistic scenario, where there is some anchoring weakly imposed by air at that boundary, but allows a small domain to be simulated without the results being dominated by effects from those boundaries.

Results

After running the two simulations to equilibrium on the denser mesh, the director and biaxiality were computed. They are visualized together in Figure 6.9. In both sets of simulations, the surface anchoring was obeyed near the top and bottom surfaces. However, in the middle, discontinuities in the director field are observed, indicating the presence of defects.

Focusing first on the simulation where the anchoring direction rotates in opposite directions in the smoothed out regions, the biaxiality observed ranged from 0 to 0.207. Three regions of high biaxiality appear to form one contiguous tube-shaped region that passes through the domain near the midpoint as well as along the boundaries between uniform and TN regions. The texture in the middle slice of the domain resembles that of a topological defect with $-\frac{1}{2}$ charge. For the remaining two regions of elevated biaxiality, the texture also has some visible discontinuities, but they are more difficult to visually distinguish. This strongly suggests that there are defects present in the domain. Furthermore, the relatively low magnitude of biaxiality observed make this somewhat inconclusive. It is thought that locally refining the mesh in this area of elevated biaxiality may allow the full structure of the defects to be resolved, if any are indeed present.

Moving on to the simulation where the anchoring direction rotates in the same direction in both smoothed out regions, the biaxiality observed ranged from 0 to 0.209. This time, two contiguous regions are observed which are both inside the TN region. Although the director field is difficult to interpret visually, it loosely resembles two $-\frac{1}{2}$ defects oriented in opposite directions. Again, since the observed biaxiality values are relatively low, a denser mesh is needed to clarify the structure of these two pockets of elevated biaxiality.

Due to the possible presence of defects, the equilibrium texture of the proposed hinge element has not been fully solved. Furthermore, if defects do exist, the LCE mechanical model will need to be modified to accommodate them, as the magnitude of nematic order drops to 0 inside a defect, whereas the current model assumes a uniform magnitude of nematic order throughout the domain.

Thus, the investigation must stop in this incomplete state. Conclusively answering the questions raised here will require a larger and more general study. For the moment, it can simply be said that even with extremely powerful alignment techniques as demonstrated in refs. 62 and 8, caution is still of utmost importance in handling defects. Furthermore, in order to explore the complex textures which endow LCEs with so much potential, texture modelling is required to ensure that proposed designs are physical and experimentally realizable.

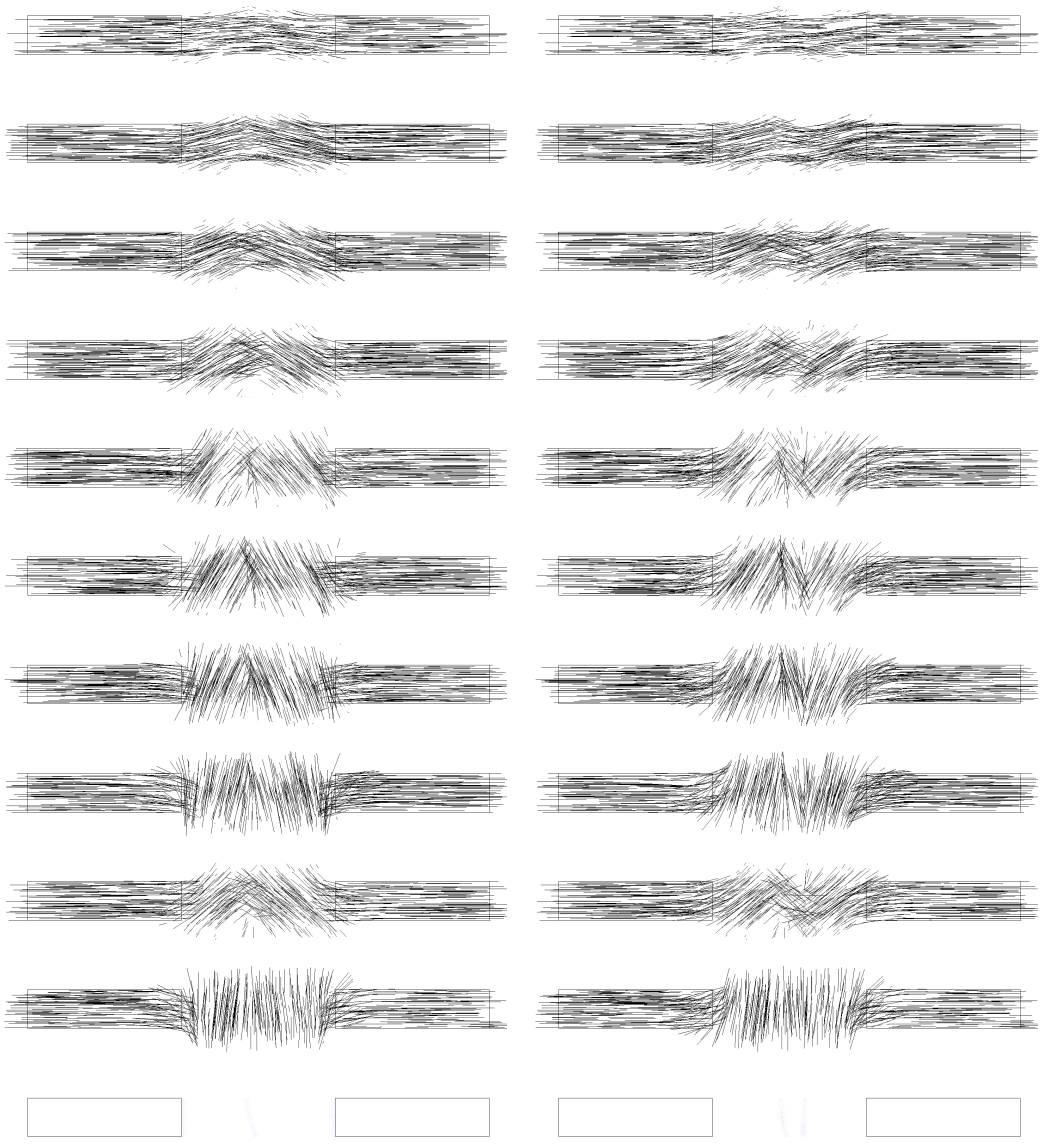

(a) (b)

Figure 6.9: Equilibrium texture of hinge made with naïve surface anchoring in slices along $\boldsymbol{e}_3$, running from the top surface to the bottom surface. Data comes from simulations having anchoring conditions where the anchoring direction rotates in (a) opposite directions, and (b) the same direction in both smoothed out regions. Final image shows volume rendering of biaxiality across all slices. An outline is drawn around the regions with uniform anchoring to provide a visual reference of the domain.

6.4 Conclusions

A design study of nematic LCE-based hinge actuators was performed, investigating nematic textures easily accessible via traditional surface alignment techniques: uniform, hybrid and twisted nematic textures. In contrast to results from the literature, size of the active region appeared to be the most important variable, due to either a mismatch in length scales in simulation and experiment, or deficiencies in the model. In the simulations, LCEs with hybrid texture had a marginally larger bending response than LCEs with TN texture.

Additionally, nematic texture simulations were performed in order to determine the feasibility of recreating the proposed textures experimentally. It was found that imposition of these textures via surface anchoring techniques introduces nematic defects, or disclinations, which would need to be accounted for in the LCE mechanical model before the investigation could be continued.

Chapter 7

Conclusions & Future Work

7.1 Conclusions

The presented methods and results represent a significant first step in the development of applications-focused simulation methods for design of temperature-responsive nematic LCEs. These methods enable the simulation of LCEs of macroscopic size and of non-trivial geometry through the use of continuum mechanics and suitable numerical methods (finite-element method). While more research needs to be done, several significant challenges required for the application of the hyperelastic solid mechanics model of Sawa *et al.* [32] have been addressed:

- Development and validation of a method for taking into account compressibility in the hyperelastic model, guided by experimental observations.
- Validation of the simulation method against experimental data for the deformation of LCE cantilevers possessing hybrid-aligned nematic textures.
- Development and validation of a method for measuring mechanical properties of LCE actuators from simulation.

During the experimental validation, good agreement was achieved between simulation and experiment for the deformation of densely cross-linked LCEs, while agreement with sparsely cross-linked LCEs remained poor. For the mechanical properties, simulations of the blocking force were used to roughly estimate the shear modulus of the experimental samples.

In addition to methods development and validation results, proof-of-concept simulation-based design studies were performed for LCE-based actuators that can be used to advance and accelerate future experimental research. These design studies focused on two applications of LCE actuators that are of current interest in the field: grippers for soft robotics and hinge mechanisms. The first design study optimized an improved design of a multi-legged LCE gripper design initially proposed by Shahsavan *et al.* [1]. In the first case, mechanical frustration was found to play a large role in the response of the LCE to stimuli. This was resolved by modifying the shape of the domain (post cross-linking).

The second study was performed for LCE-based hinge actuators and proposed an alternative design to that of Fuchi *et al.* [62] which is accessible via standard surface alignment techniques, instead of complex and expensive photoalignment techniques.

Finally, preliminary work involving the integration of nematic texture simulations (pre-cross-linking) to inform LCE mechanical modelling was performed. This integrated simulation method represents a significant advancement in the field, where the current state of the art involves either the use of simple nematic textures (pure splay, twist, or bend) or makes highly simplified assumptions of the nematic texture of the LCE prior to cross-linking.

7.2 Future Work

Several recommendations for future work can be made based upon the presented results. These recommendations can be grouped into three classifications: shortcomings of the model, shortcomings of the simulation method, and directions for future research identified in the thesis.

Two significant limitations exist in the hyperelastic solid mechanics model of Sawa *et al.* [32] in the form of assumptions: incompressibility of the LCE and uniaxiality of nematic order. Experimental results presented in Chapter 4 show that the commonly-held assumption that LCEs are incompressible is inaccurate for temperature-responsive LCEs. While a method is proposed to account for compressibility in the model, enhancement of the model to directly account for this phenomenon is more desirable. Furthermore, the model assumes uniaxial nematic order which limits its applicability to nematic textures absent of defects in orientational order. These limitations should be addressed to make the model more practical and applicable for design.

The model representation of the response of the LCE to stimuli also needs to be improved. Although the entirely empirical nature of the representation is highly general and convenient, the mismatch in properties between the weakly cross-linked planar and hybrid

samples observed in Chapter 4 highlights the need for more mechanistic knowledge. Furthermore, the method for measuring the shear modulus used in this work should be viewed as a stop-gap, and a more practical method should be investigated.

The LCE simulation methods applied in this work also suffer from two key limitations: the use of uniform domain meshing, and lack of dynamic simulations. For all but very simple nematic textures, the use of a uniform domain mesh is a severe limitation in that the presence of multiscale features (surface anchoring conditions, defects, etc.) imposes the smaller scale on the mesh element size. The use of adaptive meshing with an appropriate local error estimator would enable a reduction in computational complexity for multiscale nematic textures. Additionally, the hyperelastic model is highly nonlinear and requires a significant amount of computation time for a solution to be found. The use of dynamic simulation could both reduce the computation time for the solution of the equilibrium state and provide dynamic timescales for the response of the LCE to a change in temperature.

Since the shape of the LCE domain was found to have a large impact on its response to stimuli, purely shape-based optimization should be pursued as a means of achieving larger and more advanced responses. However, this implies that the simulation method must be able to resolve solid contact, as more complicated shapes may be far more prone to coming into contact with other parts of the domain.

The study of domains composed of a patchwork of multiple different textures also may to be a promising future direction. However, the model must be improved until the experimental phenomena of interest can be reproduced and defects can be handled. Additionally, texture modelling must remain a central part of this future work.

Finally, in both proof-of-concept design studies, improved LCE designs are proposed compared to past experimental work. As a next step, the designs should be experimentally recreated in order to verify the results and identify gaps or stumbling blocks in the application of the design method in its current state.

References

[1] H. Shahsavan, S. M. Salili, A. Jákli, and B. Zhao. Thermally active liquid crystal network gripper mimicking the self-peeling of gecko toe pads. *Advanced Materials*, 29(3):1604021, 2017. 1604021.

[2] M. Warner and E. M. Terentjev. *Liquid Crystal Elastomers*. International Series of Monographs on Physics, No. 120. OUP Oxford, 2003.

[3] P.-G. de Gennes. Un muscle artificiel semi-rapide. *C. R. Adac. Sci. II B*, 324(5):343–348, 1997.

[4] S. Petsch, B. Khatri, S. Schuhladen, L. Köbele, R. Rix, R. Zentel, and H. Zappe. Muscular MEMS—the engineering of liquid crystal elastomer actuators. *Smart Materials and Structures*, 25(8):85010, 2016.

[5] M. Yamada, M. Kondo, J. I. Mamiya, Y. Yu, M. Kinoshita, C. J. Barrett, and T. Ikeda. Photomobile polymer materials: Towards light-driven plastic motors. *Angewandte Chemie - International Edition*, 47(27):4986–4988, 2008.

[6] E.-K. Fleischmann, H.-L. Liang, N. Kapernaum, F. Giesselmann, J. Lagerwall, and R. Zentel. One-piece micropumps from liquid crystalline core-shell particles. *Nature Communications*, 3:1178, 2012.

[7] C. Li, Y. Liu, X. Huang, and H. Jiang. Direct sun-driven artificial heliotropism for solar energy harvesting based on a photo-thermomechanical liquid-crystal elastomer nanocomposite. *Advanced Functional Materials*, 22(24):5166–5174, 2012.

[8] T. H. Ware, M. E. McConney, J. J. Wie, V. P. Tondiglia, and T. J. White. Voxelated liquid crystal elastomers. *Science*, 347(6225):982–984, 2015.

[9] G. R. Luckhurst and T. J. Sluckin. *Biaxial Nematic Liquid Crystals: Theory, Simulation and Experiment*. Wiley, 2015.

[10] P.-G. de Gennes and J. Prost. The physics of liquid crystals (international series of monographs on physics). *Oxford University Press, USA*, (0.10):0–20, 1995.

[11] P. J. Collings and M. Hird. *Introduction to Liquid Crystals: Chemistry and Physics*. Liquid Crystals Book Series. Taylor & Francis, 1997.

[12] C. Zannoni, C. Fisica, and V. Risorgimento. Molecular design and computer simulations of novel mesophases. *Journal of Materials Chemistry*, 11(11):2637–2646, 2001.

[13] G. W. Gray and S. M. Kelly. Liquid crystals for twisted nematic display devices. *Journal of Materials Chemistry*, 9(9):2037–2050, 1999.

[14] E. F. Gramsbergen, L. Longa, and W. H. de Jeu. Landau Theory of the Nematic Isotropic Phase Transition. *Physics Reports*, 135(4):195–257, 1986.

[15] K. Fukuhara, S. Nagano, M. Hara, and T. Seki. Free-surface molecular command systems for photoalignment of liquid crystalline materials. *Nature Communications*, 5:1–8, 2014.

[16] M. Schadt, K. Schmitt, V. Kozinkov, and V. Chigrinov. Surface-Induced Parallel Alignment of Liquid Crystals by Linearly Polymerized Photopolymers. *Japanese Journal of Applied Physics*, 31(7 R):2155–2164, 1992.

[17] K. Ichimura, T. Seki, A. Hosokit, K. Aoki, A. Hosoki, and K. Aoki. Reversible Change in Alignment Mode of Nematic Liquid Crystals Regulated Photochemically by "Command Surfaces" Modified with an Azobenzene Monolayer. *Langmuir*, 1216(1):1214–1216, 1988.

[18] E. A. Shteyner, A. K. Srivastava, V. G. Chigrinov, H.-S. Kwok, and A. D. Afanasyev. Submicron-scale liquid crystal photo-alignment. *Soft Matter*, 9(21):5160, 2013.

[19] A. Lebar, Z. Kutnjak, S. Žumer, H. Finkelmann, A. Sánchez-Ferrer, and B. Zalar. Evidence of Supercritical Behavior in Liquid Single Crystal Elastomers. *Physical Review Letters*, 94(19):197801, 2005.

[20] A. Petelin and M. Čopič. Nematic fluctuations and semisoft elasticity in liquid-crystal elastomers. *Physical Review E*, 87(6):042502, 2013.

[21] J. V. Selinger and B. R. Ratna. Isotropic-nematic transition in liquid-crystalline elastomers: Lattice model with quenched disorder. *Physical Review E*, 70(4):041707, 2004.

[22] H. Finkelmann, A. Greve, and M. Warner. The elastic anisotropy of nematic elastomers. *European Physical Journal E*, 5(3):281–293, 2001.

[23] Y. Yusuf, J. H. Huh, P. E. Cladis, H. R. Brand, H. Finkelmann, and S. Kai. Low-voltage-driven electromechanical effects of swollen liquid-crystal elastomers. *Physical Review E*, 71(6):1–8, 2005.

[24] J. Küpfer and H. Finkelmann. Nematic liquid single crystal elastomers. *Die Makromolekulare Chemie, Rapid Communications*, 12(12):717–726, 1991.

[25] D. J. Broer, J. Boven, G. N. Mol, and G. Challa. In-situ photopolymerization of oriented liquid-crystalline acrylates, 3. oriented polymer networks from a mesogenic diacrylate. *Die Makromolekulare Chemie*, 190(9):2255–2268, 1989.

[26] M. Camacho-Lopez, H. Finkelmann, P. Palffy-Muhoray, and M. Shelley. Fast liquid-crystal elastomer swims into the dark. *Nature materials*, 3:307–310, 2004.

[27] A. Sánchez-Ferrer, A. Merekalov, and H. Finkelmann. Opto-mechanical effect in photoactive nematic side-chain liquid-crystalline elastomers. *Macromolecular Rapid Communications*, 32(8):671–678, 2011.

[28] S. Iamsaard, S. J. Aßhoff, B. Matt, T. Kudernac, J. J. L. M. Cornelissen, S. P. Fletcher, and N. Katsonis. Conversion of light into macroscopic helical motion. *Nature Chemistry*, 6(3):229–235, 2014.

[29] D. Liu and D. J. Broer. Self-assembled dynamic 3d fingerprints in liquid-crystal coatings towards controllable friction and adhesion. *Angewandte Chemie International Edition*, 53(18):4542–4546, 2014.

[30] R. R. Kohlmeyer and J. Chen. Wavelength-selective, IR light-driven hinges based on liquid crystalline elastomer composites. *Angewandte Chemie - International Edition*, 52:9234–9237, 2013.

[31] A. Kaiser, M. Winkler, S. Krause, H. Finkelmann, and A. M. Schmidt. Magnetoactive liquid crystal elastomer nanocomposites. *Journal of Materials Chemistry*, 19(4):538, 2009.

[32] Y. Sawa, K. Urayama, T. Takigawa, A. DeSimone, and L. Teresi. Thermally driven giant bending of liquid crystal elastomer films with hybrid alignment. *Macromolecules*, 43(9):4362–4369, 2010.

[33] A. Konya, V. Gimenez-Pinto, and R. L. B. Selinger. Modeling defects, shape evolution, and programmed auto-origami in liquid crystal elastomers. *Frontiers in Materials*, 3:24, 2016.

[34] H. Wermter and H. Finkelmann. Liquid crystalline elastomers as artificial muscles. *e-Polymers*, (013):1–13, 2001.

[35] A. R. Tajbakhsh and E. M. Terentjev. Spontaneous thermal expansion of nematic elastomers. *The European Physical Journal E*, 6(2):181–188, 2001.

[36] J. K. Whitmer, T. F. Roberts, R. Shekhar, N. L. Abbott, and J. J. De Pablo. Modeling the polydomain-monodomain transition of liquid crystal elastomers. *Physical Review E*, 87(2):1–5, 2013.

[37] J. Küupfer and H. Finkelmann. Liquid crystal elastomers: Influence of the orientational distribution of the crosslinks on the phase behaviour and reorientation processes. *Macromolecular Chemistry and Physics*, 195:1353–1367, 1994.

[38] K. Urayama, R. Mashita, I. Kobayashi, and T. Takigawa. Stretching-induced director rotation in thin films of liquid crystal elastomers with homeotropic alignment. *Macromolecules*, 40(21):7665–7670, 2007.

[39] G. C. Verwey and M. Warner. Soft rubber elasticity. *Macromolecules*, 28(12):4303–4306, 1995.

[40] B. L. Mbanga, F. Ye, J. V. Selinger, and R. L. B. Selinger. Modeling elastic instabilities in nematic elastomers. *Physical Review E*, 82(5):4–7, 2010.

[41] M. Warner, P. Bladon, and E. M. Terentjev. "Soft elasticity" - deformation without resistance in liquid crystal elastomers. *Journal de Physique II*, 4(1):93–102, 1994.

[42] J. S. Biggins, M. Warner, and K. Bhattacharya. Supersoft elasticity in polydomain nematic elastomers. *Physical Review Letters*, 103(3):1–4, 2009.

[43] S. Conti, A. DeSimone, and G. Dolzmann. Semisoft elasticity and director reorientation in stretched sheets of nematic elastomers. *Physical Review E*, 66(6):1–8, 2002.

[44] I. Kundler and H. Finkelmann. Strain-induced director reorientation in nematic liquid single crystal elastomers. *Macromolecular Rapid Communications*, 16(9):679–686, 1995.

[45] A. DeSimone and L. Teresi. Elastic energies for nematic elastomers. *European Physical Journal E*, 29(2):191–204, 2009.

[46] J. G. Gay and B. J. Berne. Modification of the overlap potential to mimic a linear site–site potential. *The Journal of Chemical Physics*, 74(6):3316, 1981.

[47] R. Berardi, C. Zannoni, J. S. Lintuvuori, and M. R. Wilson. A soft-core Gay-Berne model for the simulation of liquid crystals by Hamiltonian replica exchange. *The Journal of chemical physics*, 131(17):174107, 2009.

[48] G. Skačej and C. Zannoni. Molecular simulations elucidate electric field actuation in swollen liquid crystal elastomers. *Proceedings of the National Academy of Sciences of the United States of America*, 109(26):10193–8, 2012.

[49] G. Skačej and C. Zannoni. Main-chain swollen liquid crystal elastomers: a molecular simulation study. *Soft Matter*, 7(21):9983–9991, 2011.

[50] K. Urayama, S. Honda, and T. Takigawa. Deformation coupled to director rotation in swollen nematic elastomers under electric fields. *Macromolecules*, 39(5):1943–1949, 2006.

[51] J. M. Ilnytskyi, M. Saphiannikova, D. Neher, and M. P. Allen. Modelling elasticity and memory effects in liquid crystalline elastomers by molecular dynamics simulations. *Soft Matter*, 8(43):11123–11134, 2012.

[52] A. Hotta and E. M. Terentjev. Long-time stress relaxation in polyacrylate nematic liquid crystalline elastomers. *Journal of Physics: Condensed Matter*, 13(50):11453–11464, 2001.

[53] G. Skačej and C. Zannoni. Molecular simulations shed light on supersoft elasticity in polydomain liquid crystal elastomers. *Macromolecules*, 47(24):8824–8832, 2014.

[54] P. Pasini, G. Skačej, and C. Zannoni. A microscopic lattice model for liquid crystal elastomers. *Chemical Physics Letters*, 413(4-6):463–467, 2005.

[55] G. Skačej and C. Zannoni. External field-induced switching in nematic elastomers: A Monte Carlo study. *European Physical Journal E*, 20(3):289–298, 2006.

[56] W. M. Lai, D. Rubin, and E. Krempl. *Introduction to Continuum Mechanics*. Elsevier Science, 2009.

[57] D. Broer, G. P. Crawford, and S. Zumer. *Cross-Linked Liquid Crystalline Systems: From Rigid Polymer Networks to Elastomers*. Liquid Crystals Book Series. CRC Press, 2011.

[58] L. Jin, Z. Zeng, and Y. Huo. Thermomechanical modeling of the thermo-ordermechanical coupling behaviors in liquid crystal elastomers. *Journal of the Mechanics and Physics of Solids*, 58(11):1907–1927, 2010.

[59] H. Aharoni, E. Sharon, and R. Kupferman. Geometry of Thin Nematic Elastomer Sheets. *Physical Review Letters*, 113(25):257801, 2014.

[60] Y. Lin, L. Jin, and Y. Huo. Quasi-soft opto-mechanical behavior of photochromic liquid crystal elastomer: Linearized stress-strain relations and finite element simulations. *International Journal of Solids and Structures*, 49(18):2668–2680, 2012.

[61] S. Serak, N. Tabiryan, R. Vergara, T. J. White, R. A. Vaia, and T. J. Bunning. Liquid crystalline polymer cantilever oscillators fueled by light. *Soft Matter*, 6(4):779–783, 2010.

[62] K. Fuchi, T. H. Ware, P. R. Buskohl, G. W. Reich, R. A. Vaia, T. J. White, and J. J. Joo. Topology optimization for the design of folding liquid crystal elastomer actuators. *Soft Matter*, 11(37):7288–7295, 2015.

[63] C. D. Modes, M. Warner, C. Sánchez-Somolinos, L. T. De Haan, and D. Broer. Mechanical frustration and spontaneous polygonal folding in active nematic sheets. *Physical Review E*, 86(6):2–4, 2012.

[64] L. Teresi and V. Varano. Modeling helicoid to spiral-ribbon transitions of twist-nematic elastomers. *Soft Matter*, 9(11):3081, 2013.

[65] A. DeSimone, P. Gidoni, and G. Noselli. Liquid crystal elastomer strips as soft crawlers. *Journal of the Mechanics and Physics of Solids*, 84:254–272, 2015.

[66] F. Cajori. *A history of mathematical notations*, volume 1. Courier Dover Publications, 1993.

[67] J. Bonet and R. D. Wood. *Nonlinear Continuum Mechanics for Finite Element Analysis*. Cambridge University Press, 1997.

[68] M. S. Gockenbach. *Understanding and Implementing the Finite Element Method*. Society for Industrial and Applied Mathematics (SIAM, 3600 Market Street, Floor 6, Philadelphia, PA 19104), 2006.

[69] G. Barbero and L. R. Evangelista. *Adsorption phenomena and anchoring energy in nematic liquid crystals*. CRC press, 2005.

[70] P. Stein, N. Aßfalg, H. Finkelmann, and P. Martinoty. Shear modulus of polydomain, mono-domain and non-mesomorphic side-chain elastomers: Influence of the nematic order. *European Physical Journal E*, 4(3):255–262, 2001.

[71] D. Rogez, G. Francius, H. Finkelmann, and P. Martinoty. Shear mechanical anisotropy of side chain liquid-crystal elastomers: Influence of sample preparation. *European Physical Journal E*, 20(4):369–378, 2006.

[72] A. M. Squires, A. R. Tajbakhsh, and E. M. Terentjev. Dynamic Shear Modulus of Isotropic Elastomers. *Macromolecules*, 37(4):1652–1659, 2004.

[73] P. Khayyatzadeh, F. Fu, and N. M. Abukhdeir. Field-driven dynamics of nematic microcapillaries. *Physical Review E*, 92(6):1–10, 2015.

[74] F. Fu and N. M. Abukhdeir. Formation and field-driven dynamics of nematic spheroids. pages 1–36, 2017. arXiv:1702.05404v1.

[75] N. J. Mottram and C. J. P. Newton. Introduction to Q-tensor theory. pages 1–20, 2014. arXiv:1409.3542.

[76] K. B. Petersen and M. S. Pedersen. The matrix cookbook, 2012. Version 20121115.

Appendix A

Derivation of Stress for Model

The expression for the Cauchy stress tensor for the incompressible hyperelastic model described in Section 3.3.2 is derived as follows.

In Chapters 4 and 5 of ref. 67, the following relationship between W and $\boldsymbol{\sigma}$ is described:

$$\boldsymbol{P} = \frac{\partial W}{\partial \boldsymbol{F}} \tag{A.1}$$

$$\boldsymbol{\sigma} = \frac{1}{\det \boldsymbol{F}} \boldsymbol{P} \cdot \boldsymbol{F}^T \tag{A.2}$$

where $\boldsymbol{P}$ is the first Piola-Kirchhoff stress tensor.

Thus,

$$\boldsymbol{\sigma} = \frac{1}{\det \boldsymbol{F}} \frac{\partial W}{\partial \boldsymbol{F}} \cdot \boldsymbol{F}^T \tag{A.3}$$

Starting with the isotropic term:

$$W_{iso} = p(\det \boldsymbol{F} - 1) \tag{A.4}$$

$$\boldsymbol{\sigma}_{iso} = \frac{1}{\det \boldsymbol{F}} \frac{\partial W_{iso}}{\partial \boldsymbol{F}} \cdot \boldsymbol{F}^T \tag{A.5}$$

$$\tag{A.6}$$

Taking a formula from ref. 76,

$$\frac{\partial \det \boldsymbol{X}}{\partial \boldsymbol{X}} = \boldsymbol{X}^{-T} \det \boldsymbol{X} \tag{A.7}$$

The derivative can now be evaluated and substituted back into the formula for $\boldsymbol{\sigma}$.

$$\frac{\partial W_{iso}}{\partial \boldsymbol{F}} = p \frac{\partial \det \boldsymbol{F}}{\partial \boldsymbol{F}} \tag{A.8}$$

$$= p \boldsymbol{F}^{-T} \det \boldsymbol{F} \tag{A.9}$$

$$\boldsymbol{\sigma}_{iso} = p \boldsymbol{\delta} \tag{A.10}$$

Next, the deviatoric term. For brevity, let $J = \det \boldsymbol{F}$. Einstein notation [56] will be used in the derivation.

$$\hat{W}(\boldsymbol{C}) = W(\hat{\boldsymbol{C}}) \tag{A.11}$$

$$= W(J^{-2/3}\boldsymbol{C}) \tag{A.12}$$

$$= \frac{1}{2}\mu \left[J^{-2/3} C_{ab} C^{-1}_{*ba} - 3 \right] \tag{A.13}$$

$$= \frac{1}{2}\mu \left[J^{-2/3} F_{za} F_{zb} C^{-1}_{*ba} - 3 \right] \tag{A.14}$$

$$\boldsymbol{P}_{dev} = \frac{\partial \hat{W}}{\partial \boldsymbol{F}} \tag{A.15}$$

$$= \frac{1}{2}\mu C^{-1}_{*ba} \left[\frac{\partial J^{-2/3}}{\partial F_{ik}} F_{za} F_{zb} + J^{-2/3} \frac{\partial F_{za} F_{zb}}{\partial F_{ik}} \right] \tag{A.16}$$

Focusing on the first term in brackets in Equation A.16 and reusing Equation A.7,

$$\frac{\partial J^{-2/3}}{\partial F_{ik}} = -\frac{2}{3} J^{-5/3} \frac{\partial J}{\partial F_{ik}} \tag{A.17}$$

$$= -\frac{2}{3} J^{-2/3} (F^{-T})_{ik} \tag{A.18}$$

Now looking at the second term in brackets in Equation A.16,

$$\frac{\partial F_{za}F_{zb}}{\partial F_{ik}} = \frac{\partial F_{za}}{\partial F_{ik}}F_{zb} + F_{za}\frac{\partial F_{zb}}{\partial F_{ik}} \tag{A.19}$$

$$= \delta_{zi}\delta_{ak}F_{zb} + \delta_{zi}\delta_{bk}F_{za} \tag{A.20}$$

$$= \delta_{ak}F_{ib} + \delta_{bk}F_{ia} \tag{A.21}$$

This can be further simplified when substituting the results back into Equation A.16 and bringing in the C_{*ba}^{-1} term.

$$\boldsymbol{P}_{dev} = \frac{1}{2}\mu J^{-2/3}\left[-\frac{2}{3}C_{*ba}^{-1}C_{ab}(F^{-T})_{ik} + C_{*ba}^{-1}(\delta_{ak}F_{ib} + \delta_{bk}F_{ia})\right] \tag{A.22}$$

$$\left[\cdots + C_{*bk}^{-1}F_{ib} + C_{*ka}^{-1}F_{ia}\right] \tag{A.23}$$

$$\left[\cdots + C_{*kb}^{-1}F_{ib} + C_{*ka}^{-1}F_{ia}\right] \tag{A.24}$$

$$\left[\cdots + 2C_{*ka}^{-1}F_{ia}\right] \tag{A.25}$$

$$= \mu J^{-2/3}\left[C_{*ka}^{-1}F_{ia} - \frac{1}{3}C_{*ba}^{-1}C_{ab}(F^{-T})_{ik}\right] \tag{A.26}$$

Substituting that result back into Equation A.3 and simplifying yields the final result:

$$\boldsymbol{\sigma}_{dev} = \frac{1}{J}P_{ik}\cdot\left(\boldsymbol{F}^{T}\right)_{lj} \tag{A.27}$$

$$= \frac{1}{J}P_{ik}F_{jk} \tag{A.28}$$

$$= \mu J^{-5/3}\left[C_{*ka}^{-1}F_{ia}F_{jk} - \frac{1}{3}C_{*ba}^{-1}C_{ab}\delta_{ij}\right] \tag{A.29}$$

$$= \mu J^{-5/3}\left[\boldsymbol{F}\cdot\boldsymbol{C}_{*}^{-1}\cdot\boldsymbol{F}^{T} - \frac{1}{3}\left(\boldsymbol{C}\boldsymbol{C}_{*}^{-1}\right)\boldsymbol{\delta}\right] \tag{A.30}$$

Appendix B

Explanation of Image Processing Methods

The images in Figure B.1 show various steps in the image processing methods used to measure the dimensions of LCE films in Section 4.2. The original image as captured is in the upper-left, and the final processed image highlighting the edges of the film is shown in the bottom-right.

Images 1–5: Cropping to only the LCE film on a white background.

1. Original image.
2. White border is cropped, image is denoised, and a heavy median blur is applied.
3. Otsu's binarization is applied to threshold the image and emphasize the circular field of view of the microscope.
4. The largest circle in the thresholded image (and the resulting inscribed square) are found.
5. The original image is cropped with the dimensions of the inscribed square.

Images 6–10: Isolating the outline of the film from other noise in the image.

6. Image is denoised and a median blur is applied.

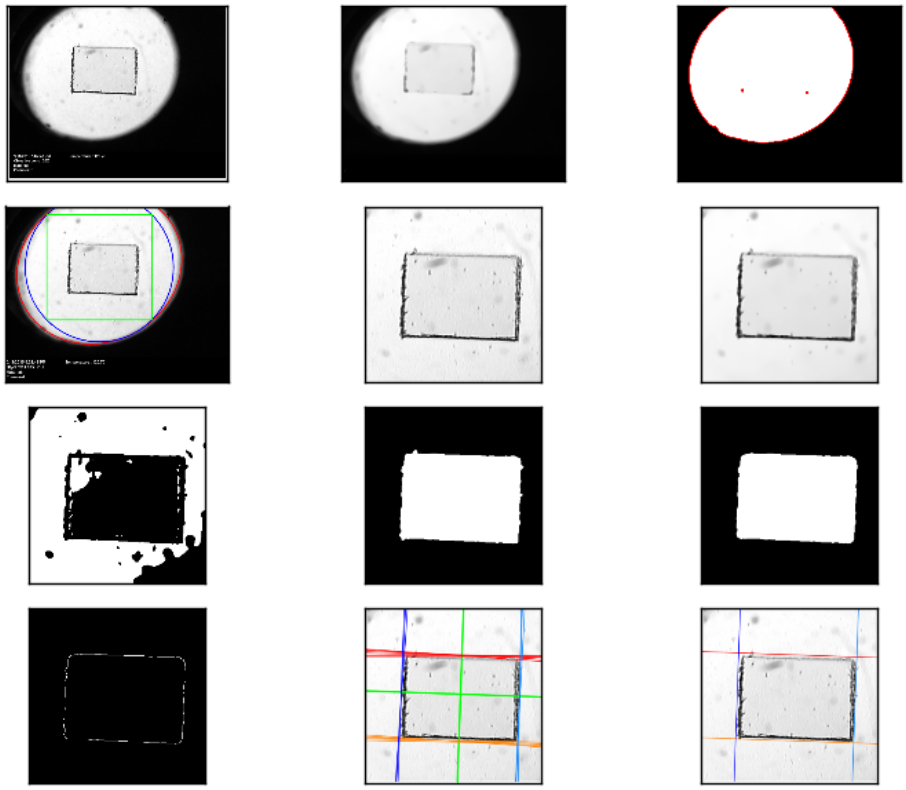

Figure B.1: Intermediate steps of the image processing method used to measure the dimensions of LCE films.

7. Image is thresholded by mean brightness value.
8. A successive dilation and erosion are performed to disconnect film from nearby blobs of dirt. Largest contiguous shape in the image is flood filled, and all other shapes are removed to eliminate tiny pieces of dirt from the background.
9. A larger erosion and dilation are performed to smooth out the shape of the film.
10. Canny edge detection is applied.

Images 11-12: Measuring the dimensions of the film outline.

11. The Hough line transform is applied. Lines are sorted into horizontal/vertical categories and outliers (in terms of angle) are removed. The midpoint of the film is estimated. Lines are further sorted into belonging to the left/right/top/bottom edge based on relative position to the estimated centre of the film.
12. Within the collection of lines for each edge, outliers (in terms of angle) are removed. Assuming the shape is roughly a parallelogram, representative edges for the left/right and top/bottom edges are chosen, and these final edges are shown.

Appendix C

Raw Data Collected for Flower Petal Study

Table C.1: Effect of cuts on mechanical properties of radial hybrid domains.

$x_{\#}$	x_d	x_w	Tip displacement (µm)	Blocking force (mN)	Energy density (kJ/m^3)
-1	-1	-1	119.5	16.61	3.40
-1	-1	$+1$	117.6	15.99	3.33
$+1$	-1	-1	126.8	16.59	3.88
$+1$	-1	$+1$	126.8	16.53	4.17
-1	$+1$	-1	151.9	11.49	3.11
-1	$+1$	$+1$	152.7	11.08	3.18
$+1$	$+1$	-1	161.0	10.68	3.43
$+1$	$+1$	$+1$	160.4	10.13	3.69

Appendix D

Documentation

D.1 Measurement of the idealized deformation

This pertains to the data collected in Section 4.2.

Figures 4.2, 4.4 and 4.3 are generated by running `map_simu_experiment.py` (`sawa:r245`) on the microscope expansion datasheet `50-100M2-M1Planar-3.csv`, separately with options `--temperature` and `--thermal`.

Figures 4.6 and 4.5 are generated by using the same script on the file `12-100M2-M1Planar-1_MANUAL.csv`.

In later revisions of the code, model files are stored in the `models` module in the `sawa` repository, and registered in the module code there with shorthand names for easy access.

D.2 Characterization of deformation

This pertains to data in Section 4.4.1 and Figures 4.8 and 4.9.

D.2.1 Setup

Follows setup from Appendix D.3.

D.2.2 Postprocessing

`calc_curvature.sh` is run using `sawa:r276` to generate curvature and position data.

The figures are generated by running `analyze_curvature_accuracy.py` (`sawa:r276`) on `displacement.npz` from the simulation with the highest density mesh. The script is run separately with options `-n 5` and `-n 100`

D.3 Mesh Independence

This pertains to data in Section 4.4.2 and Figure 4.10.

D.3.1 Setup

The folders are manually set up using code from `sawa:r246`, except for an updated version of `sawa_no_grav.py`.

`submit_jobs.sh` is run to submit all the jobs.

D.3.2 Postprocessing

Postprocessing should be done in `sawa:r254`.

`calc_curvature.sh` is run to compute curvature values and final positions.

`compare_final_point_positions.py` is run to generate the figures.

D.4 Step Size Independence

This pertains to data in Section 4.4.3 and Figure 4.11.

D.4.1 Setup

`setup_step_size_job_folders.py` is run to make folders for each of the runs.

It relies on the files inside `template_copy/`, which consist of a mesh, configuration, and code from `sawa:246` (except for an updated `sawa_no_grav.py`).

`submit_jobs.sh` is run to start all the jobs.

D.4.2 Postprocessing

Postprocessing should be done in `sawa:r254`.

`npz_hdf2any.sh` is run to generate `displacement.npz` for all simulations.

Then, `compare_final_point_positions.py` is run to generate the figures.

D.5 Hysteresis of Deformation

This pertains to data in Section 4.4.4.

D.5.1 Setup

`setup_hysteresis_job_folders.py` is run to create the simulation folders.

It relies on data from the step size simulation in `../step_size_independence_curvature/step_size_0.0025/` for the forward part of the cycle.

`submit_jobs.sh` is run to start the simulations.

D.5.2 Postprocessing

`sawa:254` should be used for postprocessing.

`npz_hdf2any.sh` is run to generate `displacement.npz` for each simulation.

`compare_final_point_positions.py` is run to generate the calculate the error.

D.6 Comparison With Experiment

This pertains to the simulations run in Section 4.4.5 and Figures 4.12 and 4.13.

D.6.1 Setup

Manual setup is performed. Code comes from `sawa:r132`, with an updated version of `sawa_no_grav.py`.

D.6.2 Postprocessing

`postproc_sim.py` is run from `sawa:r133` to compute curvature and related quantities.

The rest of the scripts are run from `sawa:r276`.

`add_exp_data.py` is run separately with parameters `50-P3` and `12-P2-man` for the 50% and 12% samples, respectively. This uses the temperature and thermal expansion models to map the simulation data onto experimental temperatures.

Then `plot_curvature.py` is run separately on the previously generated CSV files (e.g., `mapped_data_T_50-P3_--_S_50-P3.csv`) and with parameters `50-heating50-cooling` for the 50% sample and `12-c` for the 12% sample.

D.7 Mesh Independence for Blocking Force

This pertains to simulations run in Section 4.5.2 and Figure 4.14.

D.7.1 Setup

This relies on the previous mesh independence data for the free deformation of the domain, documented in Appendix D.3.

Uses `sawa:r276` and `reaction_force:67`.

First, `prep_mesh_indep_rf.py` is run to copy the free deformation data in and setup the blocking force configuration and code.

The, `submit_jobs.sh` is run to start the simulations.

D.7.2 Postprocessing

`analyze_mesh_density_rf.py` is run to generate the plots.

D.8 Step Size Independence for Blocking Force

This pertains to simulations run in Section 4.5.3 and Figure 4.15.

D.8.1 Setup

Uses `sawa:r276` and `reaction_force:67`

First, `prep_step_size_indep_rf.py` is run to set up the job folders.

It relies on the contents of `template_copy/`, which is copied from the output of the highest-density simulation from the free displacement mesh independence test.

`submit_jobs.sh` is run to start the simulations.

D.8.2 Postprocessing

`analyze_step_size_rf.py` is run to generate the plots.

D.9 Estimation of the Shear Modulus

This pertains to simulations run in Section 4.5.4 and Figures 4.16, 4.17 and 4.18.

D.9.1 Setup

First, a simulation for the free displacement of the cantilever is set up manually with code from `sawa:r148` (but updating `sawa_no_grav.py`) and run until convergence becomes poor.

The output from the free displacement simulations is manually copied over to set up the jobs where the shear modulus was varied.

`sawa_opt.py` is taken from `reaction_force:r66`. `bcic.py` is taken from `sawa:r208`.

The jobs are manually started.

For measuring the shear modulus, `setup_twostep_job_folders.py` is run to write the configuration files and copy over the mesh and scripts.

It relies on the files inside the `template` folder. The scripts are gathered from a variety of different revisions; `sawa_opt.py` is from `reaction_force:r68`, `bcic.py` from `sawa:r208`, and the rest from `sawa:r148`.

However, some adjustments were made manually to the configuration in each simulation folder so that the datapoints land extremely close to the blocking force.

D.9.2 Postprocessing

For the simulations where shear was varied, `analyze_shear_rf.py` is run using `sawa:r276` to gather blocking force data from several simulations, then `shear_rf_trend.py` is run to generate the plots for the experimental temperature-blocking force trend and the simulated shear modulus-blocking force trend.

For measuring the shear modulus, `analyze_shear_rf.py` is run from `reaction_force:r68`.

The output CSV file is renamed to `temperature_rf_results_w_shear.csv`, then `shear_rf_T_trend.py` is run from `sawa:r276` to generate the plot.

D.10 Factorial Study of Flower-shaped Domain

This pertains to the simulations run in Section 5.2, Figure 5.5, and Tables 5.2 and C.1.

D.10.1 Setup

This is run in two parts, where first the free displacement of the flower domains is simulated, and afterwards the blocking force is simulated.

`prepare_angle_cut.py` is run from `sawa:r275` to make the mesh geometries and setup the simulation folders for the free displacement.

The `template_dir` folder contains scripts (mostly) from `sawa:r208`, but with `sawa_no_grav.py` being an unversioned copy adapted with the new PDE from `sawa:r275`.

`submit_jobs.sh` is run to start the deformation jobs.

`prep_angle_cut_rf.py` is run from a separate folder to set up the blocking force simulations. It relies on copies of `sawa_opt.py` and `misc_util.py` in the same folder, which are taken from `reaction_force:r70`, while `bcic.py` is taken from `sawa:r208`.

`submit_jobs.sh` is run again to start the reaction force jobs.

D.10.2 Postprocessing

All the postprocessing is done on the blocking force data, since it contains everything needed for the figures and tables.

`hdf2any.sh` can be run to generate `.pvd` files to visualize the output in Paraview.

The temperature is found using `map_s_T.py` from `sawa:r241` and providing the value of `stretch_para` used in the reaction force simulation.

This is fed into `spline_shear_T.py` in `ch4/shear_mod_est/` to get an estimate for the shear modulus.

Once the shear modulus is known, it is hardcoded in `record_outcomes_rf.py`, which is run to generate a table of outcome measurements.

Then, `effects.py` is run to calculate the model parameters.

D.11 Sensitivity of Bending Response to Various Parameters

This pertains to the simulations run in Section 6.3.1 and Figure 6.5.

D.11.1 Setup

`prepare_clean_hinge_ff.py` is run to generate meshes and copy in relevant Python files and configuration. Since it relies on `pygmsh`, it may be easier to run locally than on SHARCNET.

The `py267` folder contains scripts (mostly) from `sawa:r267`, but with `sawa_no_grav.py` taken from `sawa:r275`.

`template_conf.yaml` contains a configuration for a TN bending actuator from `/chemeng/raeneufe/lce_fenics/r234/boom_gate/t_0.188_f_0.2/conf.yaml`, though its goal, step size, and texture specification are updated.

`ff_2(3)_design.csv` and `levels.csv` specify the variable settings for each simulation in the study.

`submit_jobs.sh` is then run to submit jobs for all the simulations.

D.11.2 Postprocessing

`hdf2any.sh` can be run with `sawa:r267` to generate `.pvd` files to visualize in Paraview.

`npz_hdf2any.sh` is run to generate a `displacement.npz` file for each simulation, which is subsequently used by `analyze_hinge_angle_ff.py` to generate the figures and `hinge_study.csv`.

`effects.py` is optionally run to do a factorial analysis on the results at a particular stretch.

D.12 Bending Response of Pure TN Domains of Varying Length

This pertains to the simulations run in Section 6.3.2 and Figure 6.6.

D.12.1 Setup

`prepare_var_length_TN.py` is run to generate meshes and copy in relevant Python files and configuration. Since it relies on pygmsh, it may be easier to run locally than on SHARCNET.

The mesh dimensions are manually changed in the script and separate folders for `width_0.25` and `width_0.50` are made by hand.

The `py267` folder contains scripts (mostly) from `sawa:r267`, but with `sawa_no_grav.py` taken from `sawa:r275`.

`hinge_buffer_template_conf.yaml` contains a configuration for a TN bending actuator from `/chemeng/raeneufe/lce_fenics/r234/boom_gate/t_0.188_f_0.2/conf.yaml`, though its goal, step size, and texture specification are updated.

`submit_jobs.sh` is then run to submit jobs for all the simulations.

D.12.2 Postprocessing

`hdf2any.sh` can be run with `sawa:r274` from each of the `width_*` folders to generate `.pvd` files to visualize in Paraview.

`npz_hdf2any.sh` can run to generate a `displacement.npz` file for each simulation, which is used by the subsequent analysis scripts.

`analyze_hinge_angle.py` is run in each of the `width_*` folders to generate `width_*_spa_*_datapoints.csv`. Note that the last few datapoints from many of the simulations with longer domains appear to have high error, with the step size rapidly shrinking and the deformations almost locking up. As such, a parallel stretch value of 0.98 is selected so that only datapoints from before this onset of problems are used in the analysis.

`plot_hinge_angle_vs_length.py` is run to aggregate data from all widths and make a combined figure.

D.13 Nematic Reorientation Dynamics

This pertains to the simulations run in Section 6.3.3 and Figure 6.9.

D.13.1 Setup

In this set of simulations, it's initially run with a lower density mesh, and resumed with a higher density mesh to get a high resolution solution while speeding up the initial equilibration.

`mesh_dense_embedded_TN_cantilever.py` and `mesh_dense_embedded_TN_cantilever_sym.py` from `code:r222` is run to generate the lower density mesh and initial conditions for the asymmetric and symmetric cantilevers, respectively.

`transient.py` from `code:r223` and `code:r222` is used to run the simulations for the asymmetric and symmetric cantilevers, respectively.

After running the simulations with the lower density mesh, `mesh_resume.py` is run to take the last solution of the lower density simulations, interpolate it onto a higher density mesh, and output the interpolation as initial conditions for the higher density simulations.

The higher density simulations are then run until they reach equilibrium as defined by the configuration.

D.13.2 Postprocessing

Some custom Paraview filters and macros are used for postprocessing the PVD output of the simulations, which are stored in `paraview_macros/` in `code:r222`.

To generate the figures, `z_slice_screenshots.py` is run from the Python shell in Paraview.

It relies on the `ComputeEigenvaluesSPBiaxiality` filter, which should be imported in Paraview first.

Appendix E

Change-in-reference Procedure

Although the simulations have been demonstrated to converge in a wide variety of situations, this seems to only hold within a limited range of the stretch parameters $\hat{\lambda}$. This problem affected all results collected. In the author's experience, as $\hat{\lambda}$ gets further from unity, more Newton iterations are required to achieve convergence at each step.

As the number of Newton iterations required exceeds the maximum limit set in the configuration, the step size is automatically decreased, which allows the simulation to continue to proceed for some time. However, as the simulation continues the step size approaches zero, marking an effective limit on the value of $\hat{\lambda}$ that can be reached.

The location of this effective limit is highly dependent on the geometry of the domain, the boundary conditions, and the nematic alignment, but it appears to be more closely related to the magnitude of deformation than $\hat{\lambda}$. This can make the range of parameters which can be simulated prohibitively small, so it is a serious obstacle in fulfilling the objectives of the project.

A countermeasure proposed and demonstrated here involves changing the reference state of the simulations part-way through. Within the model, a deformed domain is recast as a new undeformed domain in its initial state. The simulation is then able to continue until the problem is encountered again.

An illustration of the results of the method to a simulation of a bending hybrid cantilever is shown in Figure E.1.

While this method appears to function well, it substantially complicates the implementation of the simulation code and subsequent analysis. Thus, it was not completed in time to be used in the main body of the thesis. The details are presented here to document the problem and aid future work using the model.

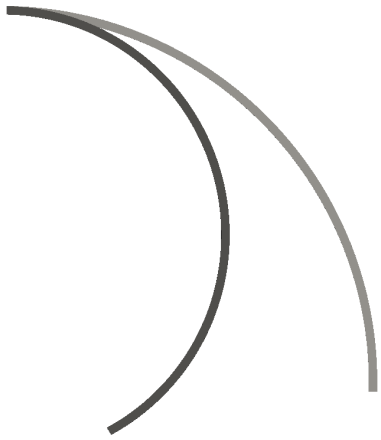

Figure E.1: Maximally-attainable deformation of a hybrid cantilever. Lighter colour: before applying change-in-reference. Darker colour: after applying change-in-reference.

E.1 Mathematical formulation

E.1.1 Immediately after updating the reference state

The first step is to update the mesh, by setting the new positions of each mesh coordinate to the deformed state of the previous mesh.

After updating the mesh, and setting the displacement in the new reference state to zero, the stretch values must also be updated.

This is because the new reference state should be at equilibrium. If the displacement is zero, this means that the stretch values should be set to unity.

To see why, observe the potential energy density formula:

$$W(\boldsymbol{C}; \boldsymbol{C}_*) = \frac{1}{2}\mu(\boldsymbol{C} : \boldsymbol{C}_*^{-1} - 3) \tag{E.1}$$

There is always a global minimum at $\boldsymbol{C} = \boldsymbol{C}_*$. In the general case, it may not be possible to find a displacement such that $\boldsymbol{C} = \boldsymbol{C}_*$, but we can work backwards by computing $\boldsymbol{C}$ for the case $\boldsymbol{u} = \boldsymbol{0}$.

$$\boldsymbol{F} = \boldsymbol{\delta} + \boldsymbol{\nabla u} \tag{E.2}$$
$$= \boldsymbol{\delta} \tag{E.3}$$

$$\boldsymbol{C} = \boldsymbol{F}^T \cdot \boldsymbol{F} \tag{E.4}$$
$$= \boldsymbol{\delta} \tag{E.5}$$

Now, we can find a value of $\boldsymbol{C}_*$ that satisfies this.

$$\boldsymbol{C}_* = \boldsymbol{C} \tag{E.6}$$
$$= \boldsymbol{\delta} \tag{E.7}$$
$$\boldsymbol{F}_* = \boldsymbol{\delta} \tag{E.8}$$
$$= \lambda_{\parallel} \boldsymbol{nn} + \lambda_{\perp} \left(\boldsymbol{\delta} - \boldsymbol{nn} \right) \tag{E.9}$$

$\left(\lambda_{\parallel}, \lambda_{\perp}\right) = (1, 1)$ will always minimize W for the case of $\boldsymbol{u} = \boldsymbol{0}$.

E.1.2 Converting from the new to previous reference state

After the reference state has been updated and the system evolves a bit, it is necessary to understand what the "overall" stretch values are in the original reference state.

It is instructive to examine how this works for a deformation gradient.

Imagine we start out in our initial reference state, $\boldsymbol{X}$, and impose the deformation $\boldsymbol{u}'$, making the intermediate state $\boldsymbol{x}' = \boldsymbol{X} + \boldsymbol{u}'$. From there, we impose another deformation $\boldsymbol{u}''$, which leaves us in the state $\boldsymbol{x}''$.

The overall deformation is $\boldsymbol{u} = \boldsymbol{u}' + \boldsymbol{u}''$.

Now we can calculate the deformation gradients for these steps:

$$\boldsymbol{F} = \boldsymbol{\delta} + \boldsymbol{\nabla u} \tag{E.10}$$
$$= \frac{\partial \boldsymbol{x}''}{\partial \boldsymbol{X}} \tag{E.11}$$

This can be decomposed into two separate deformation gradients encompassing the first and second deformations, respectively. However, it is crucial to realize that this gradient is always defined in terms of the current reference frame:

$$\boldsymbol{F}' = \boldsymbol{\delta} + \frac{\partial \boldsymbol{u}'}{\partial \boldsymbol{X}} \tag{E.12}$$

$$= \frac{\partial \boldsymbol{x}'}{\partial \boldsymbol{X}} \tag{E.13}$$

$$\boldsymbol{F}'' = \boldsymbol{\delta} + \frac{\partial \boldsymbol{u}''}{\partial \boldsymbol{x}'} \tag{E.14}$$

$$= \frac{\partial \boldsymbol{x}''}{\partial \boldsymbol{x}'} \tag{E.15}$$

The quantity $\frac{\partial \boldsymbol{x}''}{\partial \boldsymbol{x}'}$ can be rewritten:

$$\frac{\partial \boldsymbol{x}''}{\partial \boldsymbol{x}'} = \frac{\partial \boldsymbol{x}''}{\partial \boldsymbol{X}} \cdot \frac{\partial \boldsymbol{X}}{\partial \boldsymbol{x}'} \tag{E.16}$$

$$= \boldsymbol{F} \cdot \frac{\partial \boldsymbol{X}}{\partial \boldsymbol{x}'} \tag{E.17}$$

$\frac{\partial \boldsymbol{X}}{\partial \boldsymbol{x}'}$ can be thought of as the deformation gradient for the transformation from $\boldsymbol{x}'$ back into $\boldsymbol{X}$, which turns out to be $\boldsymbol{F}'^{-1}$.

Thus,

$$\boldsymbol{F}'' = \boldsymbol{F} \cdot \boldsymbol{F}'^{-1} \tag{E.18}$$

$$\boldsymbol{F}'' \cdot \boldsymbol{F}' = \boldsymbol{F} \tag{E.19}$$

Deformation gradients can be composed through the tensor dot product.

E.1.3 Idealized deformation gradient and stretch values

The formula for the idealized deformation gradient is shown below:

$$\boldsymbol{F}_*(\lambda_\parallel, \lambda_\perp, \boldsymbol{n}) = \lambda_\parallel \boldsymbol{n}\boldsymbol{n} + \lambda_\perp (\boldsymbol{\delta} - \boldsymbol{n}\boldsymbol{n}) \tag{E.20}$$

After a change-in-reference, it must also be adjusted.

Since it represents the *ideal* deformation that each infinitesimal volume "wants" to have, it is independent of the *actual* stretching of the dimensions of the domain.

However, it is sensitive to the rotation of the domain which may occur as a consequence of deformation. $\boldsymbol{n}$ represents the director orientation in the reference state; hence if the reference state changes, $\boldsymbol{n}$ must also be updated. For instance, if we start with a flat, sheet-like domain and hold the left half immobile while folding the right half 90 degrees, the director in the right half of the domain should now also rotate 90 degrees to accompany the deformation.

The rotation can be determined from the actual deformation gradient $\boldsymbol{F}$. For any physical deformation, the polar decomposition can be applied to $\boldsymbol{F}$, separating it into a rotation tensor and a stretch tensor. Incidentally, the polar decomposition can be performed 'left-handed' or 'right-handed', which result in different values for the stretch tensor, but identical rotations.

$$\boldsymbol{F} = \boldsymbol{V} \cdot \boldsymbol{R} \tag{E.21}$$
$$= \boldsymbol{R} \cdot \boldsymbol{U} \tag{E.22}$$

We can then write a new value for the director:

$$\boldsymbol{n}' = \boldsymbol{R} \cdot \boldsymbol{n} \tag{E.23}$$

Thus, in the new reference state,

$$\boldsymbol{F}'_* = \lambda'_{\parallel} \boldsymbol{n}'\boldsymbol{n}' + \lambda'_{\perp} \left(\boldsymbol{\delta} - \boldsymbol{n}'\boldsymbol{n}'\right) \tag{E.24}$$

As mentioned earlier, immediately after a change in reference, $\left(\lambda'_{\parallel}, \lambda'_{\perp}\right) = (1, 1)$ and $\boldsymbol{F}'_*$ is just the identity tensor.

The last concern is how to compute the "overall" $\left(\lambda_{\parallel}, \lambda_{\perp}\right)$, given some combination of $\left(\lambda'_{\parallel}, \lambda'_{\perp}\right)$ and $\left(\lambda''_{\parallel}, \lambda''_{\perp}\right)$.

Since $\boldsymbol{F}_*$ is fundamentally a stretch tensor with no rotation, we should counteract the actual rotation of the domain to bring the two idealized deformations into the same reference space.

If $\boldsymbol{n}'' = \boldsymbol{Q} \cdot \boldsymbol{n}'$,

$$\begin{aligned}
\boldsymbol{F}_* &= \boldsymbol{Q}^T \cdot \boldsymbol{F}_*'' \cdot \boldsymbol{Q} \cdot \boldsymbol{F}_*' && \text{(E.25)}\\
&= \boldsymbol{Q}^T \cdot \boldsymbol{F}_*(\lambda_\parallel'', \lambda_\perp'', \boldsymbol{n}'') \cdot \boldsymbol{Q} \cdot \boldsymbol{F}_*(\lambda_\parallel', \lambda_\perp', \boldsymbol{n}') && \text{(E.26)}\\
&= \boldsymbol{F}_*(\lambda_\parallel'', \lambda_\perp'', \boldsymbol{n}') \cdot \boldsymbol{F}_*(\lambda_\parallel', \lambda_\perp', \boldsymbol{n}') && \text{(E.27)}\\
&= \ldots && \text{(E.28)}\\
&= \lambda_\parallel'' \lambda_\parallel' \boldsymbol{n}'\boldsymbol{n}' + \lambda_\perp'' \lambda_\perp' \left(\delta - \boldsymbol{n}'\boldsymbol{n}'\right) && \text{(E.29)}\\
&= \boldsymbol{F}_*(\lambda_\parallel'' \lambda_\parallel', \lambda_\perp'' \lambda_\perp', \boldsymbol{n}') && \text{(E.30)}
\end{aligned}$$

So in conclusion, the "overall" stretch factors λ for a series of independent deformations are merely the product of the stretch factors of each deformation.

E.2 Validation

Performing the change-in-reference involves several numerical steps in order to deform the domain and rotate the director field appropriately, so it must introduce some numerical error into the results. This error needs to be quantified in order to evaluate the practicality of the procedure.

Although the purpose of the change-in-reference is to relieve convergence problems, for the purpose of measuring error, a simulation will first be run in a range of parameters with good convergence, and then the change-in-reference procedure will be applied at different points. The results will be compared to compute error.

The reference simulation is as follows. A rectangular domain with dimensions (3mm $\times$ 0.5mm $\times$ 0.188mm) is made, with a hybrid director field (planar portion aligned with $\boldsymbol{e}_1$, thickness direction $\boldsymbol{e}_3$). The face at $X_1 = 0$ is fixed immobile with a Dirichlet boundary condition. $\hat{\lambda}_\parallel$ is swept from 1.0 to 0.98 in even steps of 0.00125.

For quantifying error, the final position of the set of corners on the $X_1 = 3$ face will be compared to those of the reference and the Euclidean distance computed. Since the domain is a hybrid domain, it should bend as $\hat{\lambda}$ changes, and since they are at the very end of the domain, those corners will experience the largest displacement from their initial positions. Any error in the displacements will be compounded by the length of the domain, which will serve as a characteristic length scale for interpreting the results.

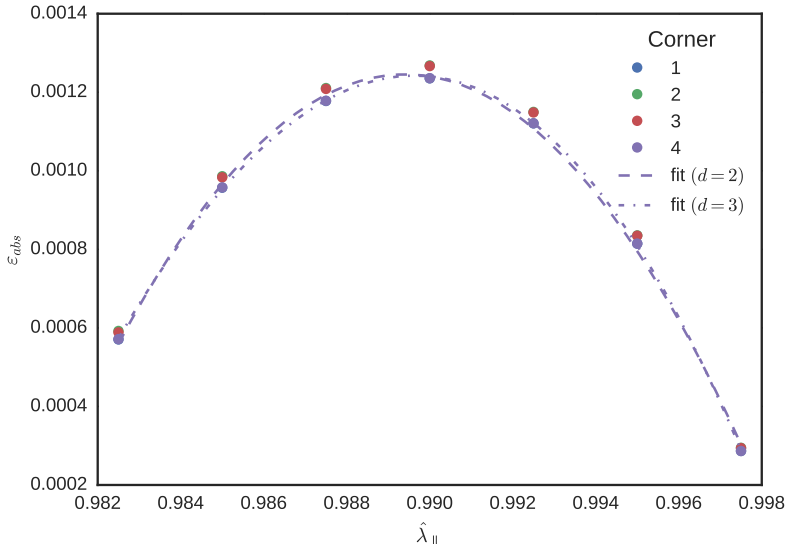

Figure E.2: Error introduced by applying the change-in-reference procedure at different steps in a simulation while maintaining step direction. Polynomial fits are also shown for corner 4.

E.2.1 Forward iteration

In this set of validation runs, a change-in-reference is performed on the reference data at various steps, and continued to achieve an overall $\hat{\lambda}_{\parallel} = 0.98$.

The steps selected have values of $\hat{\lambda}_{\parallel}$ of 0.9975, 0.9950, 0.9900, 0.9875, 0.9850, and 0.9825.

The error calculation was performed by comparing the final state of this simulation with the final state of the reference, which each have $\hat{\lambda}_{\parallel} = 0.98$, and the results are shown in Figure E.2.

The error has a maximum near $\hat{\lambda}_{\parallel} \approx 0.99$, which is the halfway point between the initial and final state of the reference simulation, and approaches zero as the change-in-reference is applied near the initial and final states.

It is unsurprising that the error is small when the change-in-reference is applied very late ($\hat{\lambda}_{\parallel} = 0.9825$); even if some error is introduced, it is only compounded over one small step.

If the perspective on which simulation is the "reference" is reversed, a similar explanation can be used to understand the low error when the change-in-reference is applied very early ($\hat{\lambda}_{\|} = 0.9975$). Even though the change-in-reference introduces some error, it is commensurate with the magnitude of the deformation of the reference simulation, which is also small at this step.

Thus, the maximum in the middle exists as a result of the larger error introduced by the change-in-reference (due to the magnitude of deformation of the reference simulation), which is then compounded over a larger number of steps.

Given the length scale of 3.0, the amount of error is relatively small in the range studied, but could grow large under repeated application of the procedure, or for very large changes in $\hat{\lambda}$.

By fitting a polynomial to the $\varepsilon_{abs}(\hat{\lambda}_{\|})$, the order of the error could also be estimated.

The second-order polynomial had a coefficient of determination $R^2 = 0.998245$, while the third-order polynomial had $R^2 = 0.999876$, making them both extremely close fits. A fourth-order polynomial was able to pass through all points exactly, but even this error measure should have its own numerical measure, so no special significance should be assigned to this.

Thus, the overall order of the error appears to be sub-quartic.

E.2.2 Hysteresis

In this set of validation runs, a change-in-reference is performed on the reference data at various steps, but the goal is set to be the initial configuration so that the overall $\hat{\lambda}_{\|} = 1.0$.

The steps selected have values of $\hat{\lambda}_{\|}$ of 0.9975, 0.9950, 0.9900, 0.9875, 0.9850, 0.9825, and 0.9800.

The error calculation was performed by comparing the final state of this simulation with the initial state of the reference, which each have $\hat{\lambda}_{\|} = 1.0$, and the results are shown in Figure E.3.

The error plot has a minimum as the change-in-reference is performed at points closer to $\hat{\lambda}_{\|} = 1.0$. This shows that the change-in-reference introduces some error which is compounded as steps are taken, regardless of forward or backward direction.

The magnitude of the error is still small in comparison to the length scale of the domain.

A polynomial was fit to $\varepsilon_{abs}(\hat{\lambda}_{\|})$ in order to estimate the order of the error.

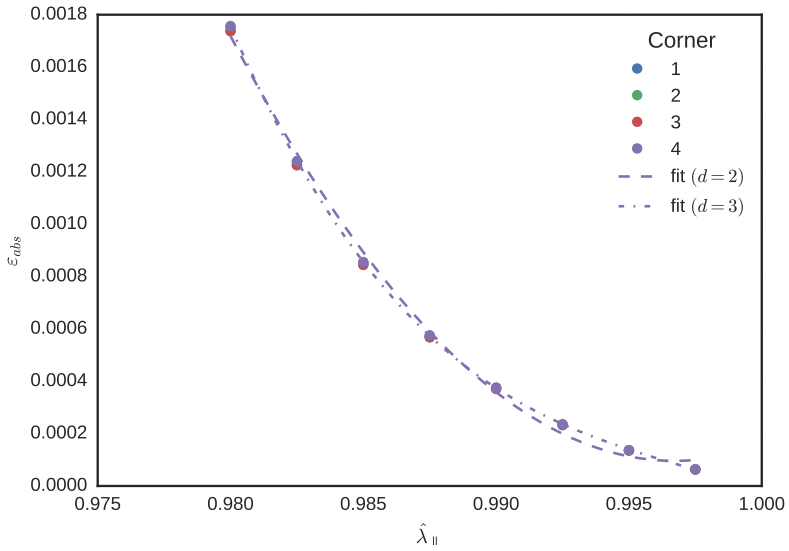

Figure E.3: Error introduced by applying the change-in-reference procedure at different steps in a simulation and reversing step direction. Polynomial fits are also shown for corner 4.

The second-order polynomial had a coefficient of determination $R^2 = 0.996982$, while the third-order polynomial had $R^2 = 0.999988$, making them both extremely close fits. Again, a fourth-order polynomial was able to pass through all points exactly.

Thus, the overall order of the error appears to be sub-quartic.